
Inverse Problems in Elliptic Charged-Particle Beams

by

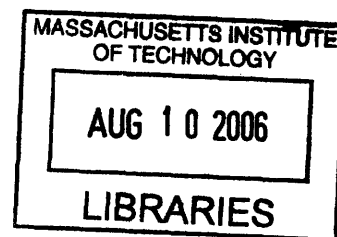
Ronak Jayant Bhatt

Bachelor of Science, Physics (1998)
California Institute of Technology

Submitted to the Department of Physics
in Partial Fulfillment of the Requirements for the Degree of


Doctor of Science in Physics
at the
Massachusetts Institute of Technology

June 2006




© 2006 Massachusetts Institute of Technology. All rights reserved.


Signature of Author:


Department of Physics
May 26, 2006

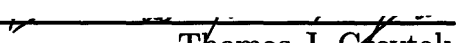
Certified by:


Richard Temkin
Senior Scientist, Department of Physics
Thesis Supervisor

Certified by:


Chiping Chen
Principal Research Scientist
Thesis Supervisor

Accepted by:


Thomas J. Greytak
Professor of Physics
Associate Department Head for Education

ARCHIVES

Inverse Problems in Elliptic Charged-Particle Beams

by Ronak Jayant Bhatt

Submitted to the Department of Physics on May 26, 2006 in Partial Fulfillment of the Requirements for the Degree of Doctor of Science in Physics

Abstract

The advantages of elliptic (or sheet) beams have been known for many years, but their inherent three-dimensional nature presents significant theoretical, design, and experimental challenges in the development of elliptic beam systems. The present work provides a framework for the design of elliptic cross-section charged-particle beam formation and transport systems.

An effective mathematical formalism for describing accelerating elliptic cross-section beams is developed in which the particle distribution function for an elliptic beam is associated with a hyperellipsoid in phase space, and the evolution equations for the particle distribution hyperellipsoid are obtained.

A novel methodology is presented for the design of elliptic beam-forming diodes utilizing an analytic prescription for the surfaces of three-dimensional electrodes which generate, accelerate, and confine a highly laminar elliptic beam. Three-dimensional simulations and tolerance studies are performed, confirming the theoretical predictions that a near-ideal beam can be produced.

Focusing systems are described for elliptic beams in coasting, accelerating, and compressing regions with analytic prescriptions for the applied electric and magnetic fields required to maintain a laminar flow profile for particles within the beam. Numerical phase-space evolution and 3D simulations confirm that self-consistent laminar flow profiles are maintained by the theoretically-designed applied fields.

The traditional approach to charged-particle dynamics problems involves extensive numerical optimization over the space of initial and boundary conditions in order to obtain desired charged-particle trajectories. The approach taken in the present work is to obtain analytic inverses wherever possible in order to minimize any necessary numerical optimization. Desired trajectories are assumed, and the applied fields and electrode geometries are then determined in a manner consistent with the assumed trajectories.

Thesis Supervisors:

Richard Temkin
Senior Scientist

Chiping Chen
Principal Research Scientist

Acknowledgements

This thesis would not have been possible without the love and support of my family. A heartfelt thank you goes out to my parents who brought me to this point and to my sister who helped push me onward.

I would like to thank my thesis advisors Chiping Chen and Rick Temkin for their enthusiasm, guidance, openness, and kindness over the years. Thanks also to Miklos Porkolab and John Belcher for serving as readers and providing valuable feedback on my research, and to Bruno Coppi for providing a welcoming environment for a fresh graduate student at MIT.

I would also like to thank all past and present members and collaborators of the Waves and Beams Division of the PSFC that I have been fortunate enough to interact with - you have made work a pleasure. In particular, the conversations with Mark Hess, Jing Zhou, Ksenia Samokhvalova, Enrique Henestroza, Tom Bemis, Jagadishwar Sirigiri, John Davies, Chad Marchewka, and Roark Marsh have been extremely useful in developing the ideas and methodology behind this thesis.

Finally, a thank you to all the friends I have made while at MIT. I consider it a blessing that you are too numerous to mention, individually. A special thank you should be reserved for my roommates during my MIT stay: Manish Jethwa, Casey Huang, and Timothy Chan.

Contents

Abstract	3
Acknowledgements	5
Contents	7
1 Introduction	11
2 Elliptic Beam Phase-Space Evolution	17
2.1 Overview	17
2.2 Self Fields of a Uniform Density Coasting Elliptic Beam in Vacuum	18
2.2.1 Overview	18
2.2.2 Internal Self-Electric Field.....	19
2.2.3 External Self-Electric Field.....	21
2.2.4 Self-Magnetic Field.....	22
2.3 Total Electric and Magnetic Fields for an Accelerating Beam	23
2.3.1 Overview	23
2.3.2 Paraxial Expansion of the Electrostatic Potential.....	24
2.3.3 Electrostatic Potential Coefficients for the Accelerating Elliptic Beam	26
2.3.4 Applied Magnetic Fields.....	30
2.3.5 Total Electric and Magnetic Fields in the Paraxial Approximation.....	32
2.4 Matrix Formulation of Transverse Equations of Motion	33
2.5 Particle Distribution Matrix	37
2.6 Elements of the Distribution Matrix	40
2.6.1 Projection of the 4D Hyperellipsoid.....	40
2.6.2 Standard Parameterization of the Ellipse.....	41
2.6.3 Relations Between Standard and Matrix Form	42
2.6.4 Relations Between Envelope Quantities and Matrix Elements	43
3 Single Particle Dynamics	49
3.1 Overview	49
3.2 Wide-Dimension Dynamics	51

3.2.1	Axial and Quadrupole Magnetic Field Contributions to the Momentum	51
3.2.2	Momentum Evolution due to the Axial Magnetic Field	52
3.2.3	Momentum Evolution due to the Quadrupole Magnetic Field	52
3.2.4	Displacement Evolution and Ordering Conditions	53
3.3	Narrow-Dimension Dynamics.....	55
3.3.1	Momentum Evolution	55
3.3.2	Displacement Evolution and Ordering Conditions	56
3.4	Survey of Ordering Regimes for Applied Fields.....	57
3.4.1	Summary of Ordering Regimes	57
3.4.2	Small Fields, Non-Oscillatory Regime.....	59
3.4.3	Small Fields, Momentum Oscillation Regime.....	59
3.4.4	Oscillatory Residual Quadrupole Field Regime.....	60
3.4.5	Small Axial Field Regime	61
3.4.6	Oscillatory Axial Field Regime	61
3.4.7	Small Residual Quadrupole Field Regime.....	62
4	Elliptic Beam Formation.....	65
4.1	Overview	65
4.2	Review of Previous Space-Charge Flow Results	66
4.2.1	Relativistic Child-Langmuir Flow	66
4.2.2	Nonrelativistic Child-Langmuir Flow	68
4.2.3	Pierce Sheet-Beam Diode.....	69
4.2.4	Radley Cylindrical Beam Diode.....	71
4.3	Elliptical Diode Theory.....	72
4.3.1	Overview	72
4.3.2	Mathieu Series Solution.....	74
4.4	Numerical Results.....	76
4.4.1	Overview	76
4.4.2	10:1 Elliptic Electron Beam	78
4.4.3	3:2 Elliptic Heavy Ion Beam	81
4.4.4	6:1 Electron Beam with Tolerance Studies.....	82
4.4.4.1	Simulation Overview.....	82
4.4.4.2	Sensitivity to Finite Extent of Electrodes	84
4.4.4.3	Sensitivity to Part Misalignment	86
4.4.4.4	Sensitivity to Thermally-Insulating Gap.....	88
4.4.4.5	Warm Beam Simulations	89
4.5	Summary.....	90
5	Elliptic Beam Transport	91

5.1	Overview	91
5.2	Envelope Perturbations.....	94
5.3	Trajectory Perturbations and Envelope Twist Angle.....	96
	5.3.1 Wide-Dimension Trajectory Perturbations.....	96
	5.3.2 Narrow-Dimension Trajectory Perturbations	97
	5.3.3 Envelope Twist Angle.....	100
5.4	Applied Fields	100
	5.4.1 Relations for Envelope Perturbations.....	100
	5.4.2 Applied Quadrupole Fields	101
	5.4.3 Applied Longitudinal Magnetic Field.....	104
5.5	Envelope Perturbations.....	105
	5.5.1 Normal Modes	105
	5.5.2 Trajectory Perturbations	107
	5.5.3 Envelope Perturbations	109
	5.5.4 Summary	110
5.6	Ordering Constraints	110
	5.6.1 Overview	110
	5.6.2 Applied Quadrupole Magnetic Field	110
	5.6.3 Axial Magnetic Field	112
	5.6.4 Small Envelope Oscillation Constraint and Summary of Ordering	116
5.7	Numerical Results.....	117
	5.7.1 6:1 Nonrelativistic Beam.....	117
	5.7.2 10:1 Relativistic Beam	121
6	Elliptic Beams in Transition	125
6.1	Overview	125
6.2	Beam Injection Matching.....	125
	6.2.1 Overview	125
	6.2.2 Applied Magnetic Fields in the Transition Region	126
	6.2.3 Semi-Analytic Solution Technique	128
	6.2.4 6:1 Elliptic Beam Matching Example.....	130
6.3	Beam Compression.....	136
	6.3.1 Overview	136
	6.3.2 Applied Magnetic Fields in the Transition Region	136
	6.3.3 6:1 Elliptic Beam Compression Example	138
7	Conclusion	145

Appendix	147
A Elliptic Projections	147
A.1 Overview	147
A.2 1D Projection of the 2D Ellipse	147
A.3 3D Projection of the 4D Hyperellipsoid	149
A.4 2D Projection of the 3D Ellipsoid	150
B Envelope Quantities	151
C Negligibility of Perturbed Trajectory Term.....	153
References.....	155

1 Introduction

The formation and control of charged-particle beams has been a topic of intense and fruitful study for a century and a half, ever since Plücker [1] reported on the deflection of cathode rays in 1858. In the span of those 150 years, we have seen the development of thousands of commercial, medical, military, industrial and research applications for charged-particle beams, from the microwave ovens and television sets in each of our homes to the largest accelerators probing the fundamental structure of matter. Most of these systems have, by the virtues of necessity, simplicity, and symmetry, utilized charged-particle beams of circular cross-section. With recent advances in numerical simulation tools, however, there has been a renewed interest in the design of 3D charged-particle beam systems.

Electron beams of elongated elliptic cross-sections (or “sheet” beams), in particular, have long generated great interest in vacuum electronics [2]. In vacuum electron devices, a resonant interaction between an electron beam and a comoving electromagnetic wave simultaneously induces bunching of the beam and amplification of the wave, thereby converting dc beam energy into rf wave energy. It is well-known that high space-charge forces inhibit beam bunching, which reduces the energy conversion efficiency in microwave tubes. Because elliptic beam distributions have a lower self-energy of assembly than circular beam distributions, their space-charge forces are reduced, and, consequently, higher energy conversion efficiencies can be attained. Moreover, high-aspect ratio elliptic beams can transport a great deal of beam current through narrow waveguides in which the beams can interact with short-wavelength (high-frequency) modes. This allows the design of rf devices with higher power and frequency than can be attained using conventional circular beam technology.

There is also interest in elliptical beams for direct injection into high-intensity ion and electron accelerators. In these systems, beams often exhibit mismatched envelope oscillations [3] and non-laminar flows such as large-amplitude density fluctuations [4], emittance growth, and chaotic particle orbits which can lead to beam interception and pose difficulty in beam focusing and compression. Many of these effects are due to beam mismatch and subsequent non-equilibrium behavior. Beams in these systems are generally formed with a circular cross-section and then must be “matched” into an alternating-gradient magnetic quadrupole lattice in which the beam is (periodically) elliptical. This process can be simplified if the beam originates with an elliptic cross-section, allowing more natural matching [5] between beam injectors and commonly used

magnetic focusing lattices and reducing the emittance growth associated with beam mismatch.

Presently, there are vigorous activities in the development of elliptic-beam sources [6] [7] [8] [9] [10], traveling wave amplifiers [9] [11], klystrons [12] [13], and focusing systems [14] [15] [16]. Over 600 high-power, high-efficiency klystrons, for example, may be needed to provide rf power for the acceleration cavities of the proposed TeV International Linear Collider (ILC). The Stanford Linear Accelerator Laboratory (SLAC) has proposed [17] a 10 MW sheet-beam klystron to meet this need, as shown in Figure 1.1. Other groups, such as Los Alamos National Laboratory (LANL), are also interested in sheet-beam technology for microwave amplifier applications. The LANL sheet-beam traveling-wave tube design [18] incorporates a solenoid/quadrupole magnet combination (shown in Figure 1.2) in order to transform an incident circular beam into an emergent elliptical beam. The Massachusetts Institute of Technology has also initiated a ribbon beam amplifier project [19] for communications and accelerator applications.

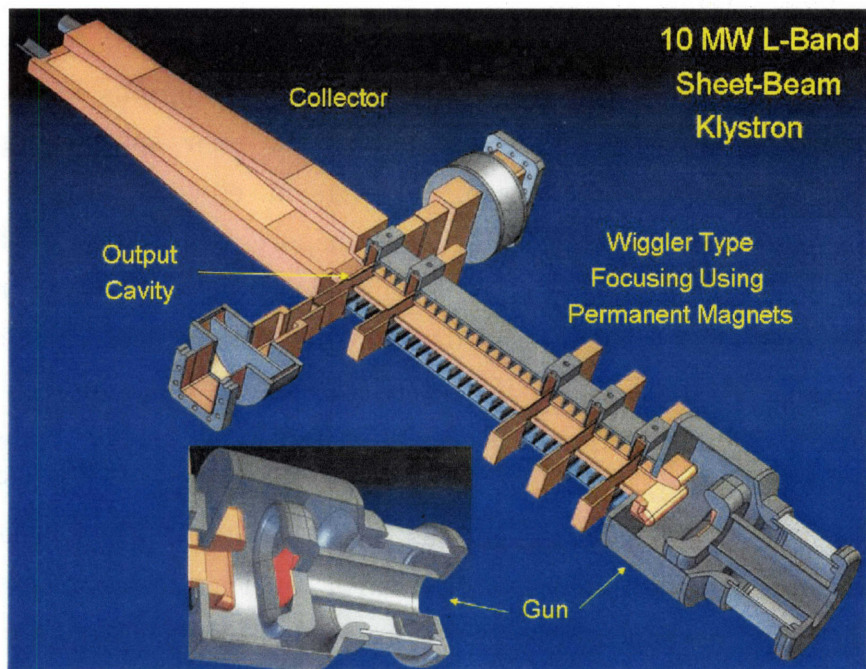


Figure 1.1: SLAC design of a 10 MW sheet-beam klystron for International Linear Collider application (Figure reproduced from Ref. [17].)

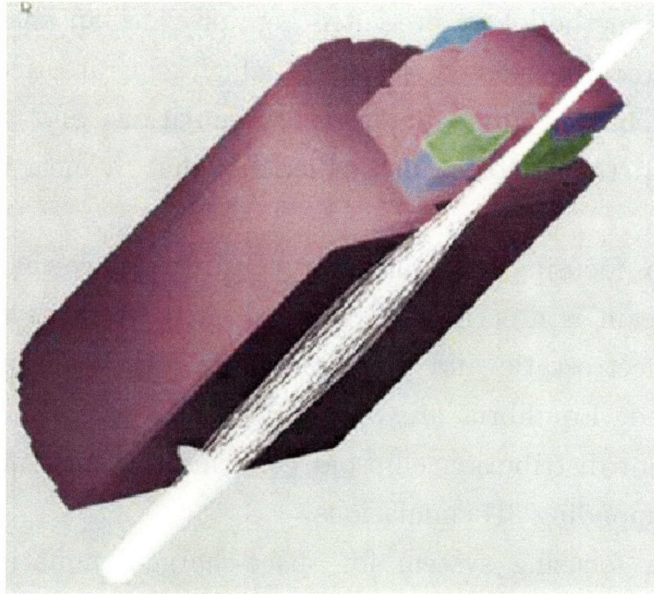


Figure 1.2: LANL design of solenoid/quadrupole magnet combination used to transform an incident circular beam into an emergent elliptical beam (Figure reproduced from Ref. [18].)

The advantages of elliptic (or sheet) beams have been known for many years, but their inherent three-dimensional nature presents significant theoretical, design, and experimental challenges in the development of elliptic beam systems. The present work provides a framework for the design of elliptic cross-section charged-particle beam formation and transport systems.

In Chapter 2, an effective mathematical formalism for describing elliptic cross-section beams is developed. The particle distribution function for an elliptic beam is associated with a hyperellipsoid in phase space, and the evolution equations for the particle distribution hyperellipsoid are obtained.

In Chapter 3, ordering arguments are presented to identify the dominant terms for single particle dynamics within elliptic beams. Criteria are established which must be met in order to maintain certain desired single-particle trajectories, and several regimes are identified which correspond to different components of a beam system: the beam-forming diode, the transitional matching section, and the coasting beam transport lattice.

In Chapter 4, a novel methodology is presented for the design of elliptic beam-forming diodes. Unlike conventional design methods utilizing extensive numerical

optimization tools, the methodology presented here provides an analytic prescription for the construction of three-dimensional electrodes which generate, accelerate, and confine a high-quality elliptic beam. Three-dimensional simulations and tolerance studies are performed, confirming the theoretical predictions that a near-ideal beam can be produced.

In Chapter 5, a focusing system for a coasting, space-charge-dominated, high aspect-ratio elliptic beam is described. Given a desired beam envelope trajectory, the equilibrium applied electrostatic and magnetic fields and beam initial conditions are analytically determined. Equilibria are constructed for example cases, and numerical integration of the beam distribution ellipsoid confirms the existence of a well-behaved beam, as do the corresponding 3D simulations.

In Chapter 6, a focusing system for space-charge-dominated, high-aspect ratio elliptical beams in transition regions is described. A semi-analytic methodology is developed to construct a laminar flow profile in the transition region between a beam-forming diode and a beam transport tunnel. Similarly, a methodology is developed to construct a laminar flow profile for an elliptic beam which is expanding or contracting. Self-consistent flow profiles are constructed for example cases, and numerical integration of the beam distribution ellipsoid confirms the existence of a well-behaved beam, as do the corresponding 3D simulations.

As we shall see in later chapters, the underlying theme of the present thesis is an inverse approach to beam system design. The traditional, or “direct”, approach to charged-particle dynamics problems involves fully specifying initial and boundary conditions (i.e., entrance conditions for an elliptic beam, electrode geometries, and applied magnetic fields are fully specified) and then integrating the particles forward to determine their trajectories. The constraints of applications, however, are usually imposed the other way: certain particle trajectories are desired and the initial and boundary conditions must be determined. This defines the inverse problem.

Without a strong analytical understanding of the system at hand, inverse problems can be quite challenging. They are usually solved by numerical optimization over some set of initial and boundary conditions. One guesses a set of initial and boundary conditions, integrates the trajectories forward, evaluates the resulting trajectories by comparing them to the desired trajectories using some merit function, and then makes adjustments to one’s initial guess and iterates. As one might imagine, for a 3D elliptic beam system, the sheer number of potential initial and boundary conditions can make brute-force numerical optimization impractical. The approach taken in the present work is to obtain analytic inverses wherever possible in order to minimize any necessary

numerical optimization. Desired trajectories are assumed, and the applied fields and electrode geometries are then determined in a manner consistent with the assumed trajectories.

2 Elliptic Beam Phase-Space Evolution

2.1 Overview

The general problem of mathematically describing a charged-particle beam evolution is quite challenging. It is easy to be overwhelmed by free parameters and functions relating to the positions and energies of the constituent beam particles and three-dimensional applied electric and magnetic fields. A common approach is to take the continuum limit and describe the beam via a particle distribution function describing the density of particles in phase (position and velocity) space. If one further imposes certain requirements on beam behavior (e.g. that the beam flows axially, is time independent, and remains confined), one can obtain constraints on the applied electric and magnetic fields. In addition, by employing the paraxial approximation under the assumptions that motion is largely along a central beam axis and that the fields and particle distribution vary only linearly in directions transverse to that axis, the problem can be made tractable.

This chapter develops a theory to describe the phase space evolution of a steady-state accelerating elliptic charged-particle beam such as that shown in Figure 2.. This type of theory can be applicable to coasting beams in magnetic and electrostatic focusing lattices as well as electrostatically accelerated beams in diode injectors and depressed collectors. The effects of self-electric and self-magnetic fields are included as well as those of applied magnetic and electric fields. The theory will be developed in the paraxial approximation, assuming forces linear in the transverse coordinates (relative to a central beam axis) and velocities largely in the longitudinal direction, compared to those in the transverse directions.

In the paraxial approximation, the transverse accelerations induced by the total electric and magnetic fields must vary linearly with the transverse coordinates. This condition is most easily satisfied if both the beam self-fields and system applied fields are independently linear in the transverse coordinates. One might also consider cases in which nonlinear forces in the self-fields are precisely canceled by nonlinear forces in the applied fields in such a way as to produce linear accelerations. The latter case is more difficult to analyze, but may be relevant to certain beam-matching situations where self-field linearity is difficult to maintain. We reserve the study of this case for future work, and address, in this chapter, the simpler case of linear self-fields and linear applied fields.

In Section 2.2 the expressions for the self-electric and magnetic fields of a coasting elliptic beam are obtained. In Section 2.3 expressions for the self-electric and magnetic fields of an accelerating elliptic beam are obtained. In Section 2.4 the single-particle equations of motion are expressed in a matrix form. In Section 2.5, the particle distribution matrix and its evolution equations are introduced. Finally, in Section 2.6, the components of the particle distribution matrix are specified and related to measurable parameters such as beam size and emittance.

2.2 Self Fields of a Uniform Density Coasting Elliptic Beam in Vacuum

2.2.1 Overview

For a beam of elliptic cross-section, linear self-fields are obtained if the beam has a uniform charge density in any transverse cross-section with a sharp elliptic boundary beyond which the charge density vanishes, as shown in Figure 2.1. This elliptic boundary of the beam is commonly referred to as the beam envelope and is characterized by its semi-major and semi-minor axes a and b , respectively. Although we assume in this section that the beam has a uniform, longitudinally constant envelope, this analysis may be also applied to elliptic beams with slowly varying envelopes [i.e., $a = a(z)$ and $b = b(z)$], provided the local values of the envelope quantities are used. We restrict our attention in this section to coasting (non-accelerating) beams.

In Section 2.2.2, an expression is obtained for the self-electric field in the region within the elliptic beam boundary. Outside the beam boundary, the self-electric field takes a different form, as shown in Section 2.2.3. The self-magnetic field is easily related to the self-electric fields, as shown in Section 2.2.4.

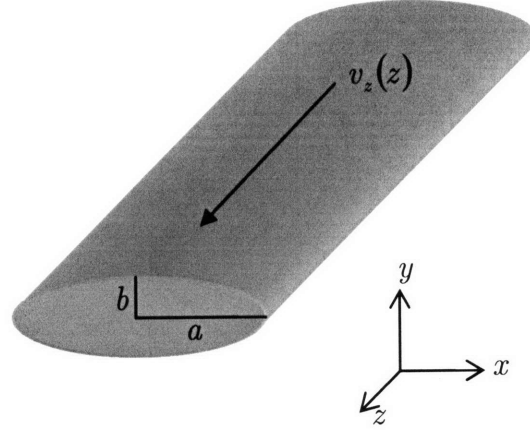


Figure 2.1: An accelerating elliptic charged-particle beam with semi-major radius a , semi-minor radius b , and axial beam velocity $\mathbf{v} = v_z \hat{\mathbf{e}}_z$.

2.2.2 Internal Self-Electric Field

For a uniform density elliptic beam with the beam axis aligned along the $\hat{\mathbf{e}}_z$ direction, semi-major axis a aligned along the $\hat{\mathbf{e}}_x$ direction, and semi-minor axis b aligned along the $\hat{\mathbf{e}}_y$ direction, the internal self electrostatic potential is given by [19] and references therein as

$$\Phi^{\rho 0} = \frac{-2I}{v_z(a+b)} \left(\frac{\tilde{x}^2}{a} + \frac{\tilde{y}^2}{b} \right), \quad (2.1)$$

where the beam velocity and current are both uniform and represented by $\mathbf{v} = v_z \hat{\mathbf{e}}_z$, and $\mathbf{I} = I \hat{\mathbf{e}}_z$, respectively. The superscript “ $\rho 0$ ” is used to denote that this is a self-field potential for the coasting beam.

The coordinate system (\tilde{x}, \tilde{y}) in which the beam ellipse semi-axes are aligned with the coordinate axes will, in general, be rotated with respect to the laboratory coordinate system (x, y) by an angle θ , as shown in Figure 2.2. The two coordinate systems are related by

$$\begin{aligned} \tilde{x} &= x \cos \theta + y \sin \theta, \\ \tilde{y} &= -x \sin \theta + y \cos \theta. \end{aligned} \quad (2.2)$$

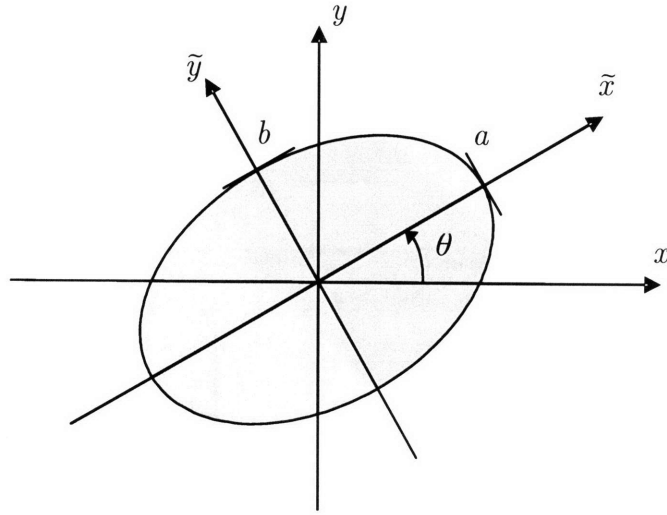


Figure 2.2: The beam-aligned coordinate system (\tilde{x}, \tilde{y}) is rotated with respect to the laboratory coordinate system (x, y) by an angle θ . The z -axis (out of the page) is also the beam axis.

In the laboratory coordinate system then, $\Phi^{\rho 0}$ becomes

$$\Phi^{\rho 0} = \Phi_{20}^{\rho 0} x^2 + \Phi_{11}^{\rho 0} xy + \Phi_{02}^{\rho 0} y^2, \quad (2.3)$$

where we have defined

$$\Phi_{20}^{\rho 0} \equiv \frac{-I}{v_z} \frac{a + b - (a - b) \cos 2\theta}{ab(a + b)}, \quad (2.4)$$

$$\Phi_{11}^{\rho 0} \equiv \frac{2I}{v_z} \frac{(a - b) \sin 2\theta}{ab(a + b)}, \quad (2.5)$$

$$\Phi_{02}^{\rho 0} \equiv \frac{-I}{v_z} \frac{a + b + (a - b) \cos 2\theta}{ab(a + b)}. \quad (2.6)$$

Note that

$$\Phi_{02}^{\rho 0} = \left(-1 + \frac{2(a + b)}{a + b - (a - b) \cos 2\theta} \right) \Phi_{20}^{\rho 0}, \quad (2.7)$$

$$\Phi_{11}^{\rho 0} = \frac{2(b - a) \sin 2\theta}{a + b - (a - b) \cos 2\theta} \Phi_{20}^{\rho 0}. \quad (2.8)$$

The results of this section are valid within the elliptic beam boundary, i.e., the shaded region in Figure 2.2.

2.2.3 External Self-Electric Field

Outside the elliptic beam boundary (i.e., in the unshaded region of Figure 2.2), the external self-electrostatic potential of the uniform elliptic beam is given in Ref. [20] by

$$-\frac{v_z}{2I} \Phi_{\text{ext}}^{\rho 0} = \ln(\sqrt{a^2 + \zeta} + \sqrt{b^2 + \zeta}) - \ln(a + b) + \frac{\tilde{x}^2 \sqrt{b^2 + \zeta} + \tilde{y}^2 \sqrt{a^2 + \zeta}}{(\sqrt{a^2 + \zeta} + \sqrt{b^2 + \zeta}) \sqrt{a^2 + \zeta} \sqrt{b^2 + \zeta}}, \quad (2.9)$$

where ζ is defined by

$$\zeta = \frac{1}{2} \left[\tilde{x}^2 + \tilde{y}^2 - a^2 - b^2 + \sqrt{(\tilde{x}^2 + \tilde{y}^2 - a^2 - b^2)^2 + 4(b^2 \tilde{x}^2 + a^2 \tilde{y}^2 - a^2 b^2)} \right]. \quad (2.10)$$

Note that the space outside the elliptic beam corresponds to $0 < \zeta < \infty$, and the $\zeta = 0$ surface corresponds to the ellipse boundary. In the laboratory coordinates, $\Phi_{\text{ext}}^{\rho 0}$ and ζ are given by

$$\begin{aligned} 2\zeta = & x^2 + y^2 - a^2 - b^2 \\ & + \left\{ [x^2 + y^2 - a^2 - b^2]^2 + 2[(a^2 + b^2)(x^2 + y^2) - 2a^2 b^2 - (a^2 - b^2)2xy \sin 2\theta \right. \\ & \left. - (a^2 - b^2)(x^2 - y^2) \cos 2\theta] \right\}^{1/2}, \end{aligned} \quad (2.11)$$

and

$$\begin{aligned} -\frac{v_z}{2I} \Phi_{\text{ext}}^{\rho 0} = & \ln(\sqrt{a^2 + \zeta} + \sqrt{b^2 + \zeta}) - \ln(a + b) + \frac{(x^2 \cos^2 \theta + y^2 \sin^2 \theta + xy \sin \theta)}{(\sqrt{a^2 + \zeta} + \sqrt{b^2 + \zeta}) \sqrt{a^2 + \zeta}} \\ & + \frac{(y^2 \cos^2 \theta + x^2 \sin^2 \theta - xy \sin \theta)}{(\sqrt{a^2 + \zeta} + \sqrt{b^2 + \zeta}) \sqrt{b^2 + \zeta}}. \end{aligned} \quad (2.12)$$

The results in Eqs. (2.11) and (2.12) are consistent with Eq. (2.1); that is, the potential is continuous across the beam boundary as shown in Figure 2.3 for the example of a uniform density, uniform velocity elliptic beam with $a/b = 10$.

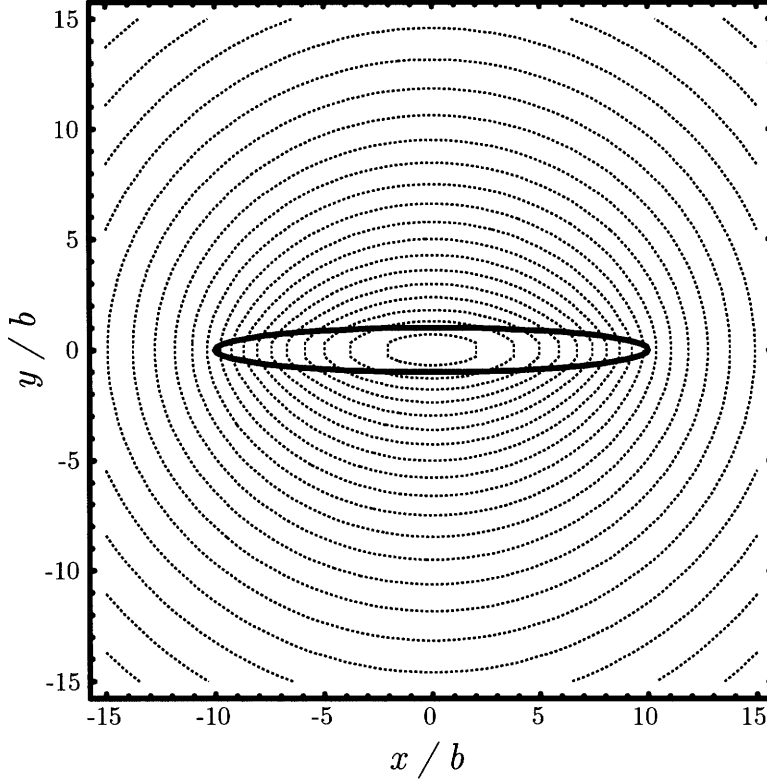


Figure 2.3: Relative equipotentials are shown both inside and outside a constant z cross-section of a 10:1 uniform density, uniform velocity elliptic beam. The solid line indicates the 10:1 elliptic beam boundary, while the dotted lines are equipotentials.

2.2.4 Self-Magnetic Field

Again following Ref. [19], the beam's self-magnetic field can be represented using a one-component vector potential $\mathbf{A}^{\rho 0} = A_z^{\rho 0} \hat{\mathbf{e}}_z$ which differs from the scalar potential by a factor of $\beta = v_z/c$, i.e., $A_z^{\rho 0} = \beta \Phi^{\rho 0}$. The self-magnetic field components can then be determined through

$$\mathbf{B}^{\rho 0} = \nabla \times \mathbf{A}^{\rho 0}, \quad (2.13)$$

which yields

$$\begin{aligned} B_x^{\rho 0} &= \frac{\partial A_z^{\rho 0}}{\partial y} \\ &= \beta (2y\Phi_{02}^{\rho 0} + x\Phi_{11}^{\rho 0}), \end{aligned} \quad (2.14)$$

$$\begin{aligned}
B_y^{\rho 0} &= -\frac{\partial A_z^{\rho 0}}{\partial x} \\
&= -\beta(2x\Phi_{20}^{\rho 0} + y\Phi_{11}^{\rho 0}).
\end{aligned}
\tag{2.15}$$

These expressions are valid within the elliptic beam boundary. Similar reasoning can be used to obtain the external self-magnetic field, but since this field does not affect the beam dynamics, we need not compute it.

2.3 Total Electric and Magnetic Fields for an Accelerating Beam

2.3.1 Overview

In this section we incorporate applied electric and magnetic fields into our paraxial field expressions. We will often refer back to the results of Section 2.2 for the self-fields, but this section is developed more generally. Since we now allow for acceleration, the axial beam velocity will no longer be axially uniform. Moreover, because of the potential gradient across the transverse dimension of the beam, the velocity will also vary transversely.

The variable-velocity beam is a natural consequence if we are dealing with the common scenario of a beam that is generated from a uniform-potential surface such as a single electrode (see Chapter 4). It has a uniform-energy, variable-velocity beam profile.

We could consider the opposite case of a variable-energy, uniform-velocity beam profile. The latter would correspond to a beam originating along a variable-potential surface such as a series of electrodes or a single electrode with a small resistance and an accompanying voltage drop from its center to its perimeter. The variable-energy configuration is difficult to construct and is not commonly applied to practical devices, and thus we will not consider it further in this study, but leave it as an avenue for future research.

The uniform-energy, variable-velocity beam profile implies that transversely uniform charge-density is not compatible with transversely uniform current-density for an accelerating beam. Again, because it is more representative of the actual devices we wish to understand (see Chapter 4), we will adopt the uniform-current-density model. This uniform-energy, uniform-current-density, variable-velocity beam profile model places a limit on the validity of the paraxial approximation, since the non-uniform charge-density implies nonlinear corrections to the self-electric field. Nonetheless, this is the most relevant model for describing common beam devices. We shall show how the

nonlinear corrections can be quantified, and find that they are quite negligible for most cases of interest. For extreme cases of very high current or very wide beams, we may be forced to resort to more complicated variable-energy configurations in order to assure linear self-fields across the beam width.

In Section 2.3.2, we develop a paraxial expansion of the electrostatic potential employing the assumptions of a uniform-energy, uniform-current-density, variable-velocity beam profile. In Section 2.3.3, we determine specific coefficients of the paraxial expansion for an accelerating elliptic beam. In Section 2.3.4, we develop an analogous paraxial expansion for the applied magnetic fields. Finally, in Section 2.3.5, we derive the total electric and magnetic fields in the paraxial approximation.

2.3.2 Paraxial Expansion of the Electrostatic Potential

In the paraxial approximation, we assume the longitudinal (\hat{e}_z -directed) particle velocities are much greater than the transverse velocities, so conservation of energy implies

$$(\gamma - \gamma_0)mc^2 = -q\Phi, \quad (2.16)$$

where $\gamma \equiv (1 - v_z^2/c^2)^{-1/2}$ is the usual relativistic factor in terms of the longitudinal particle velocity $v_z = dz/dt$, m and q are the particle mass and charge, respectively, c is the speed of light in vacuum, Φ is the electrostatic potential, and $\gamma_0 \equiv \gamma|_{\Phi=0}$ is the value taken by the relativistic factor where the electrostatic potential vanishes. For example, $\gamma_0 = 1$ for an electron which is emitted with $v_z = 0$ from a cathode at an electrostatic potential $\Phi = 0$.

We express the velocity using energy conservation, Eq. (2.16), as

$$v_z(x, y, z) = c \sqrt{1 - \left(\gamma_0 - \frac{q\Phi}{mc^2} \right)^{-2}}. \quad (2.17)$$

The total potential can be expressed as the sum of the on-axis and transversely dependent parts as $\Phi = \Phi_{00}(z) + \Phi_{\perp}(x, y, z)$, where $\Phi_{\perp} \ll \Phi_{00}$ under the paraxial approximation. We can Taylor expand the velocity to obtain

$$\begin{aligned}
v_z &= c \left[1 - \left(\gamma_0 - \frac{q\Phi_{00}}{mc^2} - \frac{q\Phi_{\perp}}{mc^2} \right)^{-2} \right]^{1/2} \\
&\cong v_{z00} \left(1 - \frac{q\Phi_{\perp}}{\beta_{00}^2 \gamma_{00}^3 mc^2} \right),
\end{aligned} \tag{2.18}$$

where the subscript “00” denotes on-axis values,

$$\gamma_{00} = \gamma_0 - \frac{q\Phi_{00}}{mc^2}, \tag{2.19}$$

$$\beta_{00} = \sqrt{1 - \gamma_{00}^{-2}}, \tag{2.20}$$

and

$$v_{z00} = \beta_{00}c. \tag{2.21}$$

Now we express the total electrostatic potential of the accelerating elliptic beam, quite generally, as

$$\Phi(x, y, z) = \sum_{n,m=0}^{\infty} x^n y^m \Phi_{nm}(z), \tag{2.22}$$

where we can see the $\Phi_{00}(z)$ term represents the on-axis part of the potential, and the rest of the sum is Φ_{\perp} . Poisson’s equation yields

$$\nabla^2 \Phi = -4\pi\rho, \tag{2.23}$$

or

$$\sum_{n,m=0}^{\infty} \left[x^n y^m \Phi_{nm}'' + n(n-1)x^{n-2}y^m \Phi_{nm} + m(m-1)x^n y^{m-2} \Phi_{nm} \right] = \frac{-4I}{abv_z}, \tag{2.24}$$

or

$$\sum_{n,m=0}^{\infty} x^n y^m \left[\Phi_{nm}' + (n+2)(n+1)\Phi_{n+2,m} + (m+2)(m+1)\Phi_{n,m+2} \right] = \frac{-4I}{abv_{z00}} \left(1 + \frac{q\Phi_{\perp}}{\beta_{00}^2 \gamma_{00}^3 mc^2} \right), \tag{2.25}$$

where the primes denote differentiation with respect to z .

We solve Eq. (2.25) by equating the coefficients of each term in the sum. The important terms are those in which the sum $n+m$ is even. The odd-sum terms

represent electric field components which produce centroid motion of the beam. If we demand that the beam axis remains fixed, we must require these centroid-motion-inducing terms to vanish. In these circumstances, the form of Eq. (2.25) ensures that these odd-sum terms are decoupled from the even-sum terms. As a result, we may freely set all the odd-sum terms to zero. The first few even-sum terms are

$$\frac{-4I}{abv_{z00}} = \Phi''_{00} + 2(\Phi_{20} + \Phi_{02}), \quad (2.26)$$

$$\frac{-4I}{abv_{z00}} \frac{q}{\beta_{00}^2 \gamma_{00}^3 mc^2} \Phi_{11} = \Phi''_{11} + 6(\Phi_{31} + \Phi_{13}), \quad (2.27)$$

$$\frac{-4I}{abv_{z00}} \frac{q}{\beta_{00}^2 \gamma_{00}^3 mc^2} \Phi_{20} = \Phi''_{20} + 2\Phi_{22} + 12\Phi_{40}, \quad (2.28)$$

$$\frac{-4I}{abv_{z00}} \frac{q}{\beta_{00}^2 \gamma_{00}^3 mc^2} \Phi_{02} = \Phi''_{02} + 2\Phi_{22} + 12\Phi_{04}. \quad (2.29)$$

We shall make use of Eq. (2.26) to describe the accelerating beam in Section 2.3.3. Equations (2.27), (2.28), and (2.29) are useful because they place limits on the validity of the paraxial approximation to the electric fields. In particular, Eqs. (2.28) and (2.29) can be examined in the limit of no z -dependence to assess the effect of the voltage depression across the beam insofar as it generates departures from uniform density. Similarly, Eq. (2.27) can be examined in the low current limit to examine the effect of beam twisting insofar as it generates nonlinear self-fields. Recall from Section 2.2.2 that the term Φ_{11} in the electrostatic potential is generated by a rotated beam.

We should note that the expressions for the potential in this section do not distinguish between self-electric fields, applied electric fields, or image charge fields induced by the beam by a conducting pipe. In fact, the expressions presented here include all of these fields. We shall illustrate in Section 2.3.3 how the electrostatic potential components are associated with each of these fields.

2.3.3 Electrostatic Potential Coefficients for the Accelerating Elliptic Beam

The total electrostatic potential consists of the axial potential, a self-field term for the accelerating beam, and another term due to all external (source-free) fields, which, to paraxial order, can be represented as an electrostatic quadrupole, i.e.,

$$\Phi = \Phi_{00} + \left(\Phi'_{20} x^2 + \Phi'_{02} y^2 + \Phi'_{11} xy \right) + \left(\Phi_Q x^2 - \Phi_Q y^2 + \Phi_Q xy \tan 2\theta_Q \right). \quad (2.30)$$

In Eq. (2.30), the first term in parentheses represents the accelerating beam self-field contribution, denoted by the superscript “ ρ ”, whereas the second term in parentheses represents the applied electrostatic quadrupole, denoted by the subscript “ Q ”. The applied electrostatic quadrupole field is rotated with respect to the laboratory coordinates by an angle θ_Q relative to the x -axis.

Rearranging terms in Eq. (2.30) and organizing them in the form of Eq. (2.22), we find

$$\begin{aligned} \Phi &= \Phi_{00} + \left(\Phi'_{20} + \Phi_Q \right) x^2 + \left(\Phi'_{02} - \Phi_Q \right) y^2 + \left(\Phi'_{11} + \Phi_Q \tan 2\theta_Q \right) xy \\ &= \Phi_{00} + \Phi_{20} x^2 + \Phi_{02} y^2 + \Phi_{11} xy, \end{aligned} \quad (2.31)$$

and the relations

$$\Phi_{20} = \Phi'_{20} + \Phi_Q, \quad (2.32)$$

$$\Phi_{02} = \Phi'_{02} - \Phi_Q, \quad (2.33)$$

$$\Phi_{11} = \Phi'_{11} + \Phi_Q \tan 2\theta_Q. \quad (2.34)$$

Note that the chosen decomposition of the total electrostatic potential in terms of a self-field and an applied contribution is not unique, i.e. there are more free parameters on the right sides of Eqs. (2.32), (2.33), and (2.34) than those on the left. This is not the case in the non-accelerating beam case. There, the self-field solution can be obtained by applying the infinitely-far boundary (no applied electric field) condition, and thus the self-field and external field components of the total potential are uncoupled. An accelerating beam, however, cannot exist without some externally applied field. In this case, the self-field and external fields are inherently coupled. While this presents some subtlety, it does not present difficulty, since we can *define* what we mean when we refer to the “self-field of an accelerating beam” as opposed to its “applied field.” By defining the “zero” of the applied electrostatic quadrupole field appropriately, we can obtain a simple result for the accelerating beam self-field. The most natural approach is to employ this process in reverse by defining an accelerating beam self-field which mimics many properties of the non-accelerating beam self-field and smoothly approaches the non-accelerating beam results in the appropriate limits. These requirements on the

accelerating beam self-field will then fix a certain definition for the applied electrostatic quadrupole field.

Let us substitute Eqs. (2.32) and (2.33) into Eq. (2.26). We find

$$2\Phi_{20}^\rho \left(1 + \frac{\Phi_{02}^\rho}{\Phi_{20}^\rho} \right) = \frac{-4I}{abv_{z00}} - \Phi_{00}'' . \quad (2.35)$$

The ratio $\Phi_{02}^\rho/\Phi_{20}^\rho$ between the self-field components of the accelerating beam is thus far undetermined in this decomposition of the total field; however, we can require that Eq. (2.35) recovers the result of Eq. (2.4) in the limit of a non-accelerating beam. This limit is recovered if we ensure that $\Phi_{02}^\rho/\Phi_{20}^\rho = \Phi_{02}^{\rho 0}/\Phi_{20}^{\rho 0}$, for in that case, Eq. (2.35) becomes

$$2\Phi_{20}^\rho \left(1 + \frac{\Phi_{02}^{\rho 0}}{\Phi_{20}^{\rho 0}} \right) = \frac{-4I}{abv_{z00}} - \Phi_{00}'' , \quad (2.36)$$

or, equivalently,

$$\frac{4(a+b)\Phi_{20}^\rho}{a+b-(a-b)\cos 2\theta} = \frac{-4I}{abv_{z00}} - \Phi_{00}'' . \quad (2.37)$$

Rearranging Eq. (2.37), we find the most natural generalization of the electrostatic potential terms from a non-accelerating to an accelerating beam:

$$\Phi_{20}^\rho = -\frac{a+b-(a-b)\cos 2\theta}{4(a+b)} \left(\frac{4I}{abc} \frac{1}{\sqrt{1-\left(\gamma_0 - \frac{q\Phi_{00}}{mc^2}\right)^{-2}}} + \Phi_{00}'' \right) , \quad (2.38)$$

and

$$\Phi_{02}^\rho = \left(-1 + \frac{2(a+b)}{a+b-(a-b)\cos 2\theta} \right) \Phi_{20}^\rho , \quad (2.39)$$

which are readily compared to Eqs. (2.4) and (2.7) in the limit of $\Phi_{00}'' \rightarrow 0$. Similarly, we can require the relative magnitude of the cross term Φ_{11}^ρ of the accelerating beam to take the same value as it does for the non-accelerating beam by fixing [in analog to Eq. (2.8)]

$$\Phi_{11}^\rho = \frac{-2(a-b)\sin 2\theta}{a+b-(a-b)\cos 2\theta} \Phi_{20}^\rho. \quad (2.40)$$

The natural generalization obtained by requiring that the accelerating beam transverse potential ratios remain the same as those for the non-accelerating beam fully specifies the decomposition of Eqs. (2.32), (2.33), and (2.34), fixing Φ_Q and θ_Q . In particular, we express

$$\begin{aligned} \frac{\Phi_{02}^{\rho 0}}{\Phi_{20}^{\rho 0}} &= \frac{\Phi_{02}^\rho}{\Phi_{20}^\rho} \\ &= \frac{\Phi_{02} + \Phi_Q}{\Phi_{20} - \Phi_Q}, \end{aligned} \quad (2.41)$$

which implies

$$\Phi_Q = \frac{\Phi_{02}^{\rho 0} \Phi_{20} - \Phi_{20}^{\rho 0} \Phi_{02}}{\Phi_{02}^{\rho 0} + \Phi_{20}^{\rho 0}}. \quad (2.42)$$

Similarly, the cross term ratio

$$\begin{aligned} \frac{\Phi_{11}^{\rho 0}}{\Phi_{20}^{\rho 0}} &= \frac{\Phi_{11}^\rho}{\Phi_{20}^\rho} \\ &= \frac{\Phi_{11} - \Phi_Q \tan 2\theta_Q}{\Phi_{20} - \Phi_Q}, \end{aligned} \quad (2.43)$$

implies

$$\tan 2\theta_Q = \frac{\Phi_{11}}{\Phi_Q} - \frac{\Phi_{11}^{\rho 0}}{\Phi_{20}^{\rho 0}} \left(\frac{\Phi_{20}}{\Phi_Q} - 1 \right). \quad (2.44)$$

The above successful separation of the applied electrostatic quadrupole terms and the self field terms of the accelerating beam will facilitate discussion in later chapters of beam focusing and equilibrium. We simply remind the reader that the Φ_Q terms represent a quadrupole electric field (rotated by an angle θ_Q relative to the x -axis of the laboratory coordinates) which is imposed by external conducting walls and applied potentials. In order to enforce a particular Φ_Q in the beam interior, electrodes at the specified potentials must be placed along one or more external equipotential surfaces given by the equation

$$\Phi_{\text{ext}} = \Phi_{00} + \Phi_{\text{ext}}^{\rho} + \Phi_Q(x^2 - y^2 + xy \tan 2\theta_Q). \quad (2.45)$$

In the non-accelerating beam limit, $\Phi_{\text{ext}}^{\rho} = \Phi_{\text{ext}}^{\rho 0}$, and the external equipotentials can be determined analytically using Eq. (2.12). This allows the design of conformal coasting beam tunnels which can aid in beam focusing (setting $\Phi_Q = 0$ defines the external equipotentials which negate all image-charge effects), or, alternatively, the design of beam tunnels which enforce a desired quadrupole focusing field on the beam. Note also that perturbations of external electrodes from the specified equipotentials will have a diminishing effect with distance from the beam. This last fact ensures that a beam tunnel of almost arbitrary shape, if sufficiently large, will have negligible image-charge effects. The more general solution of Φ_{ext}^{ρ} is left as a topic for future research in this area.

2.3.4 Applied Magnetic Fields

The most general applied magnetic field can be written as $\mathbf{B}_{\text{app}} = -\nabla\Psi$, where the magnetic potential Ψ satisfies $\nabla^2\Psi = 0$. By analogy with the electric potential, we employ a paraxial expansion

$$\Psi(x, y, z) = \sum_{n,m=0}^{\infty} x^n y^m \Psi_{nm}(z). \quad (2.46)$$

As with the electric potential, the terms in which the sum $n + m$ is odd will result in centroid motion of the beam. While centroid motion takes place in certain types of magnetic focusing systems (e.g. wiggler fields [21] [22]), for the highly elliptic, high space-charge beams of interest to us, wiggler focusing produces excessive transverse motion of the beam [14] [23] [24]. Moreover, the paraxial approximations used throughout in the present work are most accurate when the beam axis is fixed. For this reason, we will proceed as we did with the electrostatic potential, consider only the even-sum $n + m$ terms and set all the odd-sum terms to zero in Eq. (2.46). For the first few even-sum terms, Laplace's equation for the magnetic potential then yields,

$$0 = \Psi_{00}'' + 2(\Psi_{20} + \Psi_{02}), \quad (2.47)$$

$$0 = \Psi_{11}'' + 6(\Psi_{31} + \Psi_{13}), \quad (2.48)$$

$$0 = \Psi_{20}'' + 2\Psi_{22} + 12\Psi_{40}, \quad (2.49)$$

$$0 = \Psi''_{02} + 2\Psi_{22} + 12\Psi_{04}. \quad (2.50)$$

To first order in the transverse coordinates, the applied magnetic field can be written as

$$\mathbf{B}_{\text{app}} = -\nabla(\Psi_{00} + x^2\Psi_{20} + xy\Psi_{11} + y^2\Psi_{02}). \quad (2.51)$$

Combining Eqs. (2.47) and (2.51) yields

$$\mathbf{B}_{\text{app}} = B_z(z)\hat{\mathbf{e}}_z - \frac{dB_z(z)}{dz}[r_m x \hat{\mathbf{e}}_x + (1 - r_m)y \hat{\mathbf{e}}_y] + \frac{B_Q(z)}{\lambda}(y \hat{\mathbf{e}}_x + x \hat{\mathbf{e}}_y), \quad (2.52)$$

where we have defined an aspect ratio parameter for the axial magnetic field

$$r_m(z) \equiv \left(1 + \frac{\Psi_{02}(z)}{\Psi_{20}(z)}\right)^{-1}, \quad (2.53)$$

an axial field magnitude

$$B_z(z) \equiv -\Psi'_{00}(z), \quad (2.54)$$

and a quadrupole field magnitude

$$B_Q(z) \equiv -\lambda\Psi_{11}(z). \quad (2.55)$$

We have also introduced a reference length λ which will be useful for normalization purposes in Section 2.4.

Equations (2.48), (2.49), and (2.50) can be examined to determine the magnitude of the non-paraxial magnetic field components. In Chapter 5, we return to these equations in order to derive constraints on Ψ_{00} imposed by the paraxial approximation.

The application of quadrupole magnetic fields is well understood. Electromagnets with hyperbolically machined iron pole-pieces are often used when strong fields are desired. For weaker fields, permanent magnets of a variety of simple configurations can be used by noting that a quadrupole field is naturally achieved in the region between two oppositely oriented dipole magnets located some distance apart. One might use a single contiguous magnet on either side of the beam or a plurality of magnets chosen to produce the desired field in the beam area.

The longitudinal magnetic field (the components generated by the B_z term) can also be achieved through well understood means. Electromagnet and permanent magnet

solenoids and non-axisymmetric periodic cusped fields using permanent or electromagnet configurations have been described elsewhere [23] [25]. Most simply, a set of axially-magnetized planar magnets with irises would be used to construct the desired field. The iris shapes and magnet thicknesses, positions, and magnetizations will determine the axially-varying field strength and aspect ratio $r_m/(1-r_m)$. As the configuration becomes more planar, r_m approaches zero. As the configuration becomes more circular, r_m approaches $1/2$.

2.3.5 Total Electric and Magnetic Fields in the Paraxial Approximation

The total electric and magnetic fields for an accelerating elliptic beam in the paraxial approximation are

$$\mathbf{E} = -\nabla\Phi, \quad (2.56)$$

and

$$\begin{aligned} \mathbf{B} &= \mathbf{B}_{\text{app}} + \mathbf{B}^{\rho 0} \\ &= -\nabla\Psi + \nabla \times \mathbf{A}^{\rho 0}, \end{aligned} \quad (2.57)$$

where

$$\mathbf{A}^{\rho 0} = A_z^{\rho 0} \hat{\mathbf{e}}_z = \beta_{00} \Phi^{\rho 0} \hat{\mathbf{e}}_z. \quad (2.58)$$

Note that the self-magnetic field $\mathbf{B}^{\rho 0}$ for the accelerating beam is identical to that for the coasting beam, since it depends only on the local beam size, the rotation angle, and the current I , which is conserved.

Substituting the electrostatic potential Φ defined in Eq. (2.30) into Eq. (2.56), we can write the Cartesian components of the total electric field as

$$\begin{aligned} E_x &= -2x \Phi_{20} - y \Phi_{11} \\ &= -2x(\Phi'_{20} + \Phi_Q) - y(\Phi'_{11} + \Phi_Q \tan 2\theta_Q), \end{aligned} \quad (2.59)$$

$$\begin{aligned} E_y &= -2y \Phi_{02} - x \Phi_{11} \\ &= -2y(\Phi'_{02} - \Phi_Q) - x(\Phi'_{11} + \Phi_Q \tan 2\theta_Q), \end{aligned} \quad (2.60)$$

$$E_z = -\Phi'_{00}, \quad (2.61)$$

where we have used Eqs. (2.32), (2.33), and (2.34), the prime denotes a derivative with respect to z , and the accelerating beam self-field coefficients (superscript “ ρ ”) are related to the axial potential Φ_{00} through Eqs. (2.38), (2.39), and (2.40).

Similarly, substituting the applied magnetic field defined in Eq. (2.52) and the self-magnetic fields from Eqs. (2.14) and (2.15) into Eq. (2.57), we find for the Cartesian coordinates of the total magnetic field

$$B_x = x \left(\beta \Phi_{11}^{\rho 0} - r_m \frac{dB_z}{dz} \right) + y \left(\frac{B_Q}{\lambda} + 2\beta \Phi_{02}^{\rho 0} \right), \quad (2.62)$$

$$B_y = x \left(\frac{B_Q}{\lambda} - 2\beta \Phi_{20}^{\rho 0} \right) + y \left(- (1 - r_m) \frac{dB_z}{dz} - \beta \Phi_{11}^{\rho 0} \right), \quad (2.63)$$

$$B_z = B_z(z), \quad (2.64)$$

where the coasting beam self-field coefficients (superscript “ $\rho 0$ ”) are determined by Eqs. (2.4), (2.5), and (2.6).

2.4 Matrix Formulation of Transverse Equations of Motion

While the longitudinal equations of motion, more precisely the longitudinal velocity v_z , is described by Eq. (2.18), the transverse single-particle equations of motion are given by

$$\begin{aligned} \mathbf{p}_\perp &= m\gamma \frac{d\mathbf{x}_\perp}{dt} \\ &= mv_z \gamma \frac{d\mathbf{x}_\perp}{dz}, \end{aligned} \quad (2.65)$$

and

$$\begin{aligned} \mathbf{F}_\perp &= \frac{d\mathbf{p}_\perp}{dt} \\ &= v_z \frac{d\mathbf{p}_\perp}{dz}, \end{aligned} \quad (2.66)$$

where we have used the relativistic particle momentum $\mathbf{p} = \gamma m \mathbf{v}$ and the Lorentz force on a charged particle $\mathbf{F} = q(\mathbf{E} + \frac{1}{c} \mathbf{v} \times \mathbf{B})$. Referring back to Section 2.3.5, we can express the Cartesian components of the transverse Lorentz force in the paraxial approximation as

$$\begin{aligned}
F_x &= q \left(E_x + \frac{v_y}{c} B_z - \frac{v_z}{c} B_y \right) \\
&= q \left\{ -2x\Phi_{20} - y\Phi_{11} + \frac{p_y}{\gamma_{00}mc} B_z \right. \\
&\quad \left. - \frac{v_{z00}}{c} \left[x \left(\frac{B_Q}{\lambda} - 2\beta_{00}\Phi_{20}^{\rho 0} \right) + y \left(-\frac{dB_z}{dz} (1 - r_m) - \beta_{00}\Phi_{11}^{\rho 0} \right) \right] \right\},
\end{aligned} \tag{2.67}$$

and

$$\begin{aligned}
F_y &= q \left(E_y - \frac{v_x}{c} B_z + \frac{v_z}{c} B_x \right) \\
&= q \left\{ -2y\Phi_{02} - x\Phi_{11} - \frac{p_x}{\gamma_{00}mc} B_z \right. \\
&\quad \left. + \frac{v_{z00}}{c} \left[x \left(-\frac{dB_z}{dz} r_m + \beta_{00}\Phi_{11}^{\rho 0} \right) + y \left(\frac{B_Q}{\lambda} + 2\beta_{00}\Phi_{02}^{\rho 0} \right) \right] \right\}.
\end{aligned} \tag{2.68}$$

Note that in the paraxial approximation above, we retain only those terms linear in the transverse coordinates and momenta. We henceforth suppress the subscript “00” on the velocity functions v_z , β , and γ with the understanding that we will always refer to their axial values.

We are now able to write the equation of motions (2.65) and (2.66) in a matrix form as

$$\frac{d\boldsymbol{\chi}}{dz} = \underline{\mathbf{F}} \cdot \boldsymbol{\chi}, \tag{2.69}$$

where

$$\boldsymbol{\chi}(z) \equiv \begin{pmatrix} x \\ p_x \\ y \\ p_y \end{pmatrix}, \tag{2.70}$$

$$\underline{\mathbf{F}} \equiv \begin{pmatrix} 0 & F_{xp_x} & 0 & 0 \\ F_{p_x x} & 0 & F_{p_x y} & F_{p_x p_y} \\ 0 & 0 & 0 & F_{yp_y} \\ F_{p_y x} & F_{p_y p_x} & F_{p_y y} & 0 \end{pmatrix}, \tag{2.71}$$

and the elements of $\underline{\mathbf{F}}$ are

$$F_{xp_x} = F_{yp_y} = \frac{1}{\gamma\beta mc}, \quad (2.72)$$

$$F_{p_x x} = q \left[-\frac{2}{\beta c} \Phi_{20} - \frac{1}{c} \left(\frac{B_Q}{\lambda} - 2\beta \Phi_{20}^{\rho 0} \right) \right], \quad (2.73)$$

$$F_{p_x y} = q \left[-\frac{1}{\beta c} \Phi_{11} + \frac{1}{c} \left(\beta \Phi_{11}^{\rho 0} + \frac{dB_z}{dz} (1 - r_m) \right) \right], \quad (2.74)$$

$$F_{p_y x} = q \left[-\frac{1}{\beta c} \Phi_{11} + \frac{1}{c} \left(\beta \Phi_{11}^{\rho 0} - \frac{dB_z}{dz} r_m \right) \right], \quad (2.75)$$

$$F_{p_y y} = q \left[-\frac{2}{\beta c} \Phi_{02} + \frac{1}{c} \left(\frac{B_Q}{\lambda} + 2\beta \Phi_{02}^{\rho 0} \right) \right], \quad (2.76)$$

and

$$F_{p_x p_y} = -F_{p_y p_x} = \frac{qB_z}{\gamma\beta mc^2}. \quad (2.77)$$

It is useful to work in dimensionless quantities and express Eqs. (2.65) and (2.66) as

$$\bar{\mathbf{p}}_{\perp} = \beta\gamma \frac{d\bar{\mathbf{x}}_{\perp}}{d\bar{z}}, \quad (2.78)$$

and

$$\bar{\mathbf{F}}_{\perp} = \frac{d\bar{\mathbf{p}}_{\perp}}{d\bar{z}}, \quad (2.79)$$

where

$$\bar{\mathbf{p}} \equiv \frac{\mathbf{p}}{mc}, \quad (2.80)$$

$$\bar{\mathbf{x}} \equiv \frac{\mathbf{x}}{\lambda}, \quad (2.81)$$

$$\bar{\mathbf{F}} \equiv \mathbf{F} \frac{\lambda}{\beta mc^2}, \quad (2.82)$$

and λ is the arbitrary scale length introduced in the discussion of the quadrupole magnetic field in Section 2.3.4. We also introduce the dimensionless constant

$$\alpha_\lambda \equiv \frac{q^2}{\lambda mc^2}, \quad (2.83)$$

the dimensionless electrostatic potential

$$\bar{\Phi}_{nm} \equiv \frac{\lambda^{n+m+1}}{q} \Phi_{nm}, \quad (2.84)$$

the dimensionless magnetic fields

$$\bar{B}_Q \equiv \frac{\lambda^2}{q} B_Q, \quad (2.85)$$

$$\bar{B}_z \equiv \frac{\lambda^2}{q} B_z, \quad (2.86)$$

and the dimensionless current

$$\bar{I} \equiv \frac{I\lambda}{qc}. \quad (2.87)$$

We can express Eqs. (2.78) and (2.79) in the dimensionless matrix form

$$\frac{d\bar{\mathbf{x}}}{d\bar{z}} = \bar{\mathbf{F}} \cdot \bar{\mathbf{x}}, \quad (2.88)$$

where

$$\bar{\mathbf{x}}(\bar{z}) \equiv \begin{pmatrix} \bar{x} \\ \bar{p}_x \\ \bar{y} \\ \bar{p}_y \end{pmatrix}, \quad (2.89)$$

$$\underline{\underline{\mathbf{F}}} \equiv \begin{pmatrix} 0 & \overline{F}_{x\overline{p}_x} & 0 & 0 \\ \overline{F}_{\overline{p}_x\overline{x}} & 0 & \overline{F}_{\overline{p}_x\overline{y}} & \overline{F}_{\overline{p}_x\overline{p}_y} \\ 0 & 0 & 0 & \overline{F}_{\overline{y}\overline{p}_y} \\ \overline{F}_{\overline{p}_y\overline{x}} & \overline{F}_{\overline{p}_y\overline{p}_x} & \overline{F}_{\overline{p}_y\overline{y}} & 0 \end{pmatrix}, \quad (2.90)$$

and the elements of $\underline{\underline{\mathbf{F}}}$ here are

$$\overline{F}_{x\overline{p}_x} = \overline{F}_{\overline{y}\overline{p}_y} = \frac{1}{\gamma\beta}, \quad (2.91)$$

$$\overline{F}_{\overline{p}_x\overline{x}} = \frac{\alpha_\lambda}{\beta} \left(-2\overline{\Phi}_{20} - \beta\overline{B}_Q + 2\beta^2\overline{\Phi}_{20}^{\rho 0} \right), \quad (2.92)$$

$$\overline{F}_{\overline{p}_x\overline{y}} = \frac{\alpha_\lambda}{\beta} \left(-\overline{\Phi}_{11} + \beta^2\overline{\Phi}_{11}^{\rho 0} + \beta \frac{d\overline{B}_z}{d\overline{z}} (1 - r_m) \right), \quad (2.93)$$

$$\overline{F}_{\overline{p}_y\overline{x}} = \frac{\alpha_\lambda}{\beta} \left(-\overline{\Phi}_{11} + \beta^2\overline{\Phi}_{11}^{\rho 0} - \beta \frac{d\overline{B}_z}{d\overline{z}} r_m \right), \quad (2.94)$$

$$\overline{F}_{\overline{p}_y\overline{y}} = \frac{\alpha_\lambda}{\beta} \left(-2\overline{\Phi}_{02} + \beta\overline{B}_Q + 2\beta^2\overline{\Phi}_{02}^{\rho 0} \right), \quad (2.95)$$

and

$$\overline{F}_{\overline{p}_x\overline{p}_y} = -\overline{F}_{\overline{p}_y\overline{p}_x} = \frac{\alpha_\lambda \overline{B}_z}{\gamma\beta}. \quad (2.96)$$

2.5 Particle Distribution Matrix

There exists a transfer matrix $\underline{\underline{\mathbf{T}}}$ that transforms an initial condition $\boldsymbol{\chi}_0$ into a final vector $\boldsymbol{\chi}$, i.e.,

$$\boldsymbol{\chi} = \underline{\underline{\mathbf{T}}} \cdot \boldsymbol{\chi}_0. \quad (2.97)$$

The relationship between the transfer matrix and the force matrix is explored by differentiating both sides of Eq. (2.97) to yield

$$\begin{aligned}
\frac{d\boldsymbol{\chi}}{dz} &= \frac{d}{dz} (\underline{\mathbf{T}} \cdot \boldsymbol{\chi}_0) \\
\underline{\mathbf{F}} \cdot \boldsymbol{\chi} &= \frac{d\underline{\mathbf{T}}}{dz} \cdot \boldsymbol{\chi}_0 \\
\underline{\mathbf{F}} \cdot \underline{\mathbf{T}} \cdot \boldsymbol{\chi}_0 &= \frac{d\underline{\mathbf{T}}}{dz} \cdot \boldsymbol{\chi}_0.
\end{aligned} \tag{2.98}$$

Since this is true for any initial condition $\boldsymbol{\chi}_0$, we have

$$\underline{\mathbf{F}} \cdot \underline{\mathbf{T}} = \frac{d\underline{\mathbf{T}}}{dz}. \tag{2.99}$$

Following Sacherer [26], let us introduce the symmetric matrix $\underline{\mathbf{M}}$ which defines the hyperellipsoid of the phase-space distribution of the particle beam through the equation

$$\boldsymbol{\chi}^T \cdot \underline{\mathbf{M}}^{-1} \cdot \boldsymbol{\chi} = 1, \tag{2.100}$$

where the superscript “ T ” denotes the transpose operation of a matrix, and

$$\underline{\mathbf{M}} = \begin{pmatrix} M_{xx} & M_{xp_x} & M_{xy} & M_{xp_y} \\ M_{p_x x} & M_{p_x p_x} & M_{p_x y} & M_{p_x p_y} \\ M_{yx} & M_{yp_x} & M_{yy} & M_{yp_y} \\ M_{p_y x} & M_{p_y p_x} & M_{p_y y} & M_{p_y p_y} \end{pmatrix}. \tag{2.101}$$

A uniform distribution of particles along this ellipsoidal hypersurface ensures a uniform charge density in position space, and thus the assumption of linear self fields is satisfied [26]. Familiar phase space plots can be obtained by taking projections of the 4D hyperellipsoid into a 2D subspace, yielding an ellipse, as shown in Figure 2.4.

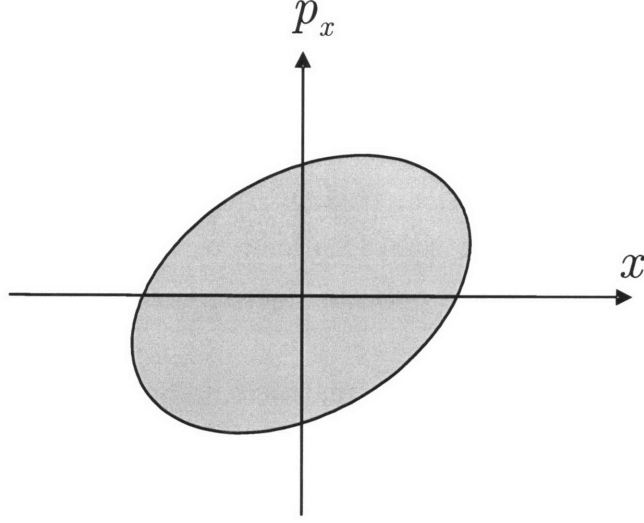


Figure 2.4: The projection of the 4D particle distribution hyperellipsoid onto the subspace (x, p_x) yields a filled 2D ellipse.

Since Eq. (2.100) holds for all z , we can write

$$\begin{aligned}
 \underline{\boldsymbol{\chi}}_0^T \cdot \underline{\mathbf{M}}_0^{-1} \cdot \underline{\boldsymbol{\chi}}_0 &= 1 \\
 &= \underline{\boldsymbol{\chi}}^T \cdot \underline{\mathbf{M}}^{-1} \cdot \underline{\boldsymbol{\chi}} \\
 &= (\underline{\mathbf{T}} \cdot \underline{\boldsymbol{\chi}}_0)^T \cdot \underline{\mathbf{M}}^{-1} \cdot (\underline{\mathbf{T}} \cdot \underline{\boldsymbol{\chi}}_0) \\
 &= \underline{\boldsymbol{\chi}}_0^T \cdot \underline{\mathbf{T}}^T \cdot \underline{\mathbf{M}}^{-1} \cdot \underline{\mathbf{T}} \cdot \underline{\boldsymbol{\chi}}_0.
 \end{aligned} \tag{2.102}$$

Since this holds for arbitrary $\underline{\boldsymbol{\chi}}_0$, we find $\underline{\mathbf{M}}_0^{-1} = \underline{\mathbf{T}}^T \cdot \underline{\mathbf{M}}^{-1} \cdot \underline{\mathbf{T}}$, and therefore

$$\underline{\mathbf{M}} = \underline{\mathbf{T}} \cdot \underline{\mathbf{M}}_0 \cdot \underline{\mathbf{T}}^T. \tag{2.103}$$

The evolution of the beam distribution is fully characterized by the distribution matrix $\underline{\mathbf{M}}$, which evolves according to

$$\begin{aligned}
 \frac{d\underline{\mathbf{M}}}{dz} &= \frac{d}{dz} (\underline{\mathbf{T}} \cdot \underline{\mathbf{M}}_0 \cdot \underline{\mathbf{T}}^T) \\
 &= \frac{d\underline{\mathbf{T}}}{dz} \cdot \underline{\mathbf{M}}_0 \cdot \underline{\mathbf{T}}^T + \underline{\mathbf{T}} \cdot \underline{\mathbf{M}}_0 \cdot \frac{d\underline{\mathbf{T}}^T}{dz} \\
 &= \underline{\mathbf{F}} \cdot \underline{\mathbf{T}} \cdot \underline{\mathbf{M}}_0 \cdot \underline{\mathbf{T}}^T + \underline{\mathbf{T}} \cdot \underline{\mathbf{M}}_0 \cdot \underline{\mathbf{T}}^T \cdot \underline{\mathbf{F}}^T \\
 &= \underline{\mathbf{F}} \cdot \underline{\mathbf{M}} + \underline{\mathbf{M}} \cdot \underline{\mathbf{F}}^T.
 \end{aligned} \tag{2.104}$$

2.6 Elements of the Distribution Matrix

The elements of the force matrix $\underline{\underline{\mathbf{F}}}$ have been expressed in terms of the beam envelope quantities such as the semi-major axis a , the semi-minor axis b , and the rotation angle θ . In order to close the matrix equation of motion (2.104), we must relate the elements of the distribution matrix $\underline{\underline{\mathbf{M}}}$ to the envelope quantities. These physical envelope quantities are directly related to the semi-axis lengths, inclination angles, and areas of 2D ellipses – projections of the 4D particle distribution hyperellipsoid as shown in Figure 2.4.

In Subsection 2.6.1, we describe the matrix equation for a 2D ellipse projected from the 4D particle distribution hyperellipsoid. In Subsection 2.6.2, we describe a geometric representation for a general 2D ellipse, the so-called standard form. In Subsection 2.6.3, the relationship between the matrix representation and standard form is obtained, which enables us to relate geometric quantities such as semi-axis lengths to matrix elements. In Subsection 2.6.4, we use the results of Subsection 2.6.3 to relate physical beam envelope parameters to elements of the 4D particle distribution hyperellipsoid.

For ease of notation we will suppress the overbars, but we will use dimensionless quantities for the remainder of this section.

2.6.1 Projection of the 4D Hyperellipsoid

As shown in Figure 2.4, the 4D hyperellipsoid represented by Eq. (2.100) forms a 2D ellipse when projected into any 2D subspace (x_1, x_2) where $x_1, x_2 \in (x, y, p_x, p_y)$. The equation for the projected ellipse is simply

$$1 = \boldsymbol{\chi}_{12}^T \cdot \underline{\underline{\mathbf{M}}}_{12}^{-1} \cdot \boldsymbol{\chi}_{12}, \quad (2.105)$$

where

$$\boldsymbol{\chi}_{12} \equiv \begin{pmatrix} x_1 \\ x_2 \end{pmatrix}, \quad (2.106)$$

and

$$\underline{\underline{\mathbf{M}}}_{12} \equiv \begin{pmatrix} M_{11} & M_{12} \\ M_{12} & M_{22} \end{pmatrix}. \quad (2.107)$$

The elements of $\underline{\underline{M}}_{12}$ are selected from the elements of $\underline{\underline{M}}$ in Eq. (2.101), i.e., $\underline{\underline{M}}_{12}$ is a submatrix of $\underline{\underline{M}}$. Proof of Eq. (2.105) is relegated to Appendix A, however, we can expand Eq. (2.105) as

$$M_{11}M_{22} - M_{12}^2 = M_{22}x_1^2 + M_{11}x_2^2 - 2M_{12}x_1x_2. \quad (2.108)$$

As an alternative to writing the equation for the ellipse in the matrix form as in Eq. (2.108), we can use the geometric (or standard) parameterization.

2.6.2 Standard Parameterization of the Ellipse

The standard form of the equation for an ellipse is given by

$$1 = \frac{\tilde{x}_1^2}{A^2} + \frac{\tilde{x}_2^2}{B^2}, \quad (2.109)$$

which describes an ellipse with semi axes A and B aligned along the $\hat{e}_{\tilde{x}_1}$ and $\hat{e}_{\tilde{x}_2}$ axes, respectively. We can express Eq. (2.109) in a rotated set of coordinates through the transformation

$$\begin{aligned} \tilde{x}_1 &= x_1 \cos \theta_{12} + x_2 \sin \theta_{12}, \\ \tilde{x}_2 &= -x_1 \sin \theta_{12} + x_2 \cos \theta_{12}, \end{aligned} \quad (2.110)$$

which yields for the ellipse

$$1 = x_1^2 \left(\frac{\cos^2 \theta_{12}}{A^2} + \frac{\sin^2 \theta_{12}}{B^2} \right) + x_2^2 \left(\frac{\sin^2 \theta_{12}}{A^2} + \frac{\cos^2 \theta_{12}}{B^2} \right) + x_1 x_2 \left(\frac{1}{A^2} - \frac{1}{B^2} \right) \sin(2\theta_{12}). \quad (2.111)$$

The relationship between the ellipse-aligned and rotated coordinate system is shown in Figure 2.5.

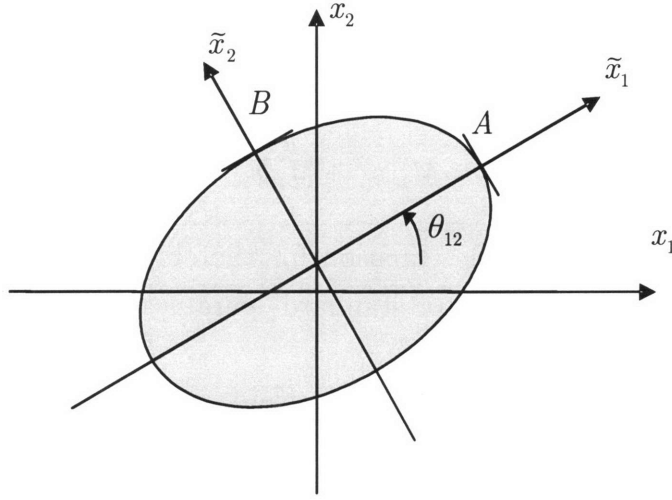


Figure 2.5: The ellipse-aligned coordinate system $(\tilde{x}_1, \tilde{x}_2)$ is rotated with respect to the rotated coordinate system (x_1, x_2) by an angle θ_{12} , as shown.

2.6.3 Relations Between Standard and Matrix Form

Equating the coefficients between the matrix form of Eq. (2.108) and the standard form of Eq. (2.111) allows us to write

$$M_{11} = A^2 \cos^2 \theta_{12} + B^2 \sin^2 \theta_{12}, \quad (2.112)$$

$$M_{12} = (A^2 - B^2) \sin \theta_{12} \cos \theta_{12}, \quad (2.113)$$

$$M_{22} = B^2 \cos^2 \theta_{12} + A^2 \sin^2 \theta_{12}, \quad (2.114)$$

and the inverse relations

$$A = \frac{1}{\sqrt{2}} \sqrt{M_{11} + M_{22} + \sqrt{M_{11}^2 + M_{22}^2 + 4M_{12}^2 - 2M_{11}M_{22}}}, \quad (2.115)$$

$$B = \frac{1}{\sqrt{2}} \sqrt{M_{11} + M_{22} - \sqrt{M_{11}^2 + M_{22}^2 + 4M_{12}^2 - 2M_{11}M_{22}}}, \quad (2.116)$$

$$\theta_{12} = \frac{1}{2} \arctan \left(\frac{2M_{12}}{M_{11} - M_{22}} \right). \quad (2.117)$$

Note that the area of the ellipse can be expressed using Eqs. (2.115) and (2.116) as

$$\pi AB = \pi \sqrt{M_{11}M_{22} - M_{12}^2}. \quad (2.118)$$

The results of this section are derived in Appendix B.

2.6.4 Relations Between Envelope Quantities and Matrix Elements

Making use of the results of Section 2.6.3 and setting $x = x_1$ and $y = x_2$, we express the envelope quantities in terms of the matrix elements as

$$a(z) = \frac{1}{\sqrt{2}} \sqrt{M_{xx}(z) + M_{yy}(z) + \sqrt{M_{xx}^2(z) + M_{yy}^2(z) + 4M_{xy}^2(z) - 2M_{xx}(z)M_{yy}(z)}}, \quad (2.119)$$

$$b(z) = \frac{1}{\sqrt{2}} \sqrt{M_{xx}(z) + M_{yy}(z) - \sqrt{M_{xx}^2(z) + M_{yy}^2(z) + 4M_{xy}^2(z) - 2M_{xx}(z)M_{yy}(z)}}, \quad (2.120)$$

$$\theta = \frac{1}{2} \arctan \left(\frac{2M_{xy}}{M_{xx} - M_{yy}} \right). \quad (2.121)$$

By taking a projection of the 4D particle distribution ellipsoid into the subspace (x, y) , we obtained Eqs. (2.119), (2.120), (2.121), which relate the three independent matrix quantities M_{xx} , M_{xy} , and M_{yy} to three physically meaningful quantities, namely, semi-major axis a , semi-minor axis b , and inclination angle θ . For the 4×4 symmetric matrix $\underline{\underline{\mathbf{M}}}$, there are 10 independent elements, overall, which can be related to 10 independent physically meaningful quantities by taking projections of the 4D ellipsoid into various 2D subspaces. The projection into the subspace (x, y) yielded the envelope semi-axes and inclination angle; projections into other subspaces will yield fluid velocities related to beam expansion and rotation as well as beam emittances. For our purposes, we define an emittance as the phase space area of a given 2D subspace divided by π .

In order to obtain simple relations between the physical parameters and the matrix elements, we will find it useful to introduce a beam-aligned symmetric matrix $\underline{\underline{\tilde{\mathbf{M}}}}$ with the elements in the rotated phase space

$$\underline{\underline{\tilde{\mathbf{M}}}} = \begin{pmatrix} M_{\tilde{x}\tilde{x}} & M_{\tilde{x}p_{\tilde{x}}} & M_{\tilde{x}\tilde{y}} & M_{\tilde{x}p_{\tilde{y}}} \\ M_{p_{\tilde{x}}\tilde{x}} & M_{p_{\tilde{x}}p_{\tilde{x}}} & M_{p_{\tilde{x}}\tilde{y}} & M_{p_{\tilde{x}}p_{\tilde{y}}} \\ M_{\tilde{y}\tilde{x}} & M_{\tilde{y}p_{\tilde{x}}} & M_{\tilde{y}\tilde{y}} & M_{\tilde{y}p_{\tilde{y}}} \\ M_{p_{\tilde{y}}\tilde{x}} & M_{p_{\tilde{y}}p_{\tilde{x}}} & M_{p_{\tilde{y}}\tilde{y}} & M_{p_{\tilde{y}}p_{\tilde{y}}} \end{pmatrix}. \quad (2.122)$$

This matrix describes an ellipsoid via the equation

$$\tilde{\boldsymbol{\chi}}^T \cdot \underline{\underline{\tilde{\mathbf{M}}}}^{-1} \cdot \tilde{\boldsymbol{\chi}} = 1, \quad (2.123)$$

where

$$\tilde{\boldsymbol{\chi}} \equiv \underline{\underline{\mathbf{R}}} \cdot \boldsymbol{\chi}, \quad (2.124)$$

or

$$\begin{pmatrix} \tilde{x} \\ p_{\tilde{x}} \\ \tilde{y} \\ p_{\tilde{y}} \end{pmatrix} = \begin{pmatrix} \cos \theta & 0 & \sin \theta & 0 \\ 0 & \cos \theta & 0 & \sin \theta \\ -\sin \theta & 0 & \cos \theta & 0 \\ 0 & -\sin \theta & 0 & \cos \theta \end{pmatrix} \cdot \begin{pmatrix} x \\ p_x \\ y \\ p_y \end{pmatrix}. \quad (2.125)$$

From this it is clear that $\underline{\underline{\mathbf{M}}} = \underline{\underline{\mathbf{R}}}^{-1} \cdot \underline{\underline{\tilde{\mathbf{M}}}} \cdot \underline{\underline{\mathbf{R}}}$ and $\underline{\underline{\tilde{\mathbf{M}}}} = \underline{\underline{\mathbf{R}}} \cdot \underline{\underline{\mathbf{M}}} \cdot \underline{\underline{\mathbf{R}}}^{-1}$. In terms of the beam-aligned distribution matrix elements, the envelope quantities take on simple forms since $M_{\tilde{x}\tilde{y}} = 0$. As a reminder, we make explicit the dimensionlessness of the envelope quantities by replacing the overbars. The 10 independent physical parameters are determined by analogy to the results of Section 2.6.3, yielding

$$\bar{a} \equiv \frac{a}{\lambda} = \sqrt{M_{\tilde{x}\tilde{x}}}, \quad (2.126)$$

$$\bar{b} \equiv \frac{b}{\lambda} = \sqrt{M_{\tilde{y}\tilde{y}}}, \quad (2.127)$$

$$\theta = \frac{1}{2} \arctan \left(\frac{2M_{xy}}{M_{xx} - M_{yy}} \right), \quad (2.128)$$

$$\theta_{\tilde{x}p_{\tilde{x}}} = \frac{1}{2} \arctan \left(\frac{2M_{\tilde{x}p_{\tilde{x}}}}{M_{\tilde{x}\tilde{x}} - M_{p_{\tilde{x}}p_{\tilde{x}}}} \right), \quad (2.129)$$

$$\bar{\varepsilon}_{\tilde{x}p_{\tilde{x}}} = \sqrt{M_{\tilde{x}\tilde{x}}M_{p_{\tilde{x}}p_{\tilde{x}}} - M_{\tilde{x}p_{\tilde{x}}}^2}, \quad (2.130)$$

$$\theta_{\tilde{y}p_{\tilde{y}}} = \frac{1}{2} \arctan \left(\frac{2M_{\tilde{y}p_{\tilde{y}}}}{M_{\tilde{y}\tilde{y}} - M_{p_{\tilde{y}}p_{\tilde{y}}}} \right), \quad (2.131)$$

$$\bar{\varepsilon}_{\tilde{y}p_{\tilde{y}}} = \sqrt{M_{\tilde{y}\tilde{y}}M_{p_{\tilde{y}}p_{\tilde{y}}} - M_{\tilde{y}p_{\tilde{y}}}^2}, \quad (2.132)$$

$$\theta_{\tilde{x}p_{\tilde{y}}} = \frac{1}{2} \arctan\left(\frac{2M_{\tilde{x}p_{\tilde{y}}}}{M_{\tilde{x}\tilde{x}} - M_{p_{\tilde{y}}p_{\tilde{y}}}}\right), \quad (2.133)$$

$$\theta_{\tilde{y}p_{\tilde{x}}} = \frac{1}{2} \arctan\left(\frac{2M_{\tilde{y}p_{\tilde{x}}}}{M_{\tilde{y}\tilde{y}} - M_{p_{\tilde{x}}p_{\tilde{x}}}}\right), \quad (2.134)$$

$$\theta_{p_{\tilde{x}}p_{\tilde{y}}} = \frac{1}{2} \arctan\left(\frac{2M_{p_{\tilde{x}}p_{\tilde{y}}}}{M_{p_{\tilde{x}}p_{\tilde{x}}} - M_{p_{\tilde{y}}p_{\tilde{y}}}}\right). \quad (2.135)$$

The dimensionless normalized emittance $\bar{\varepsilon}_{\tilde{x}p_{\tilde{x}}}$ or $\bar{\varepsilon}_{\tilde{y}p_{\tilde{y}}}$ appearing in Eq. (2.130) or (2.132) is defined as $1/\pi$ times the phase-space area of the projected ellipse in the associated subspace $(\tilde{x}, p_{\tilde{x}})$ or $(\tilde{y}, p_{\tilde{y}})$. Further discussion on emittance is deferred until Section 4.4.1.

The tangents of the angles $\theta_{\tilde{x}p_{\tilde{x}}}$ and $\theta_{\tilde{y}p_{\tilde{y}}}$ defined in Eqs. (2.129) and (2.131) characterize beam expansion. In the cold-fluid limit, the emittances vanish, the distribution ellipse collapses to an inclined line segment in the subspaces $(\tilde{x}, p_{\tilde{x}})$ and $(\tilde{y}, p_{\tilde{y}})$, and we find $\tan\theta_{\tilde{x}p_{\tilde{x}}} = p_{\tilde{x}}/\tilde{x}$ and $\tan\theta_{\tilde{y}p_{\tilde{y}}} = p_{\tilde{y}}/\tilde{y}$. In this case, it is easy to relate $\theta_{\tilde{x}p_{\tilde{x}}}$ and $\theta_{\tilde{y}p_{\tilde{y}}}$ to the normalized variables $\mu_x = a^{-1} da/dz$ and $\mu_y = b^{-1} db/dz$ in the terminology of Ref. [19], i.e.,

$$\begin{aligned} \tan\theta_{\tilde{x}p_{\tilde{x}}} &= \frac{\beta\gamma}{\tilde{x}} \frac{d\tilde{x}}{d\tilde{z}} \\ &= \beta\gamma\lambda\mu_x, \end{aligned} \quad (2.136)$$

$$\begin{aligned} \tan\theta_{\tilde{y}p_{\tilde{y}}} &= \frac{\beta\gamma}{\tilde{y}} \frac{d\tilde{y}}{d\tilde{z}} \\ &= \beta\gamma\lambda\mu_y. \end{aligned} \quad (2.137)$$

Similarly, the tangents of the angles $\theta_{\tilde{x}p_{\tilde{y}}}$ and $\theta_{\tilde{y}p_{\tilde{x}}}$ defined in Eqs. (2.133) and (2.134) characterize beam rotation. In the cold-fluid limit, the emittances vanish, the distribution ellipse collapses to an inclined line segment in the subspaces $(\tilde{x}, p_{\tilde{y}})$ and $(\tilde{y}, p_{\tilde{x}})$, and we find $\tan\theta_{\tilde{x}p_{\tilde{y}}} = p_{\tilde{y}}/\tilde{x}$ and $\tan\theta_{\tilde{y}p_{\tilde{x}}} = p_{\tilde{x}}/\tilde{y}$. In this case, it is easy to relate $\theta_{\tilde{x}p_{\tilde{y}}}$ and $\theta_{\tilde{y}p_{\tilde{x}}}$ to the normalized variables α_x and α_y in the terminology of Ref. [19], i.e.,

$$\begin{aligned}\tan\theta_{\tilde{x}p_{\tilde{y}}} &= \frac{\beta\gamma}{\tilde{x}} \frac{d\tilde{y}}{d\tilde{z}} \\ &= \beta\gamma\lambda\alpha_y,\end{aligned}\tag{2.138}$$

$$\begin{aligned}\tan\theta_{\tilde{y}p_{\tilde{x}}} &= \frac{\beta\gamma}{\tilde{y}} \frac{d\tilde{y}}{d\tilde{z}} \\ &= -\beta\gamma\lambda\alpha_x.\end{aligned}\tag{2.139}$$

The angle $\theta_{p_{\tilde{x}}p_{\tilde{y}}}$ defined in Eq. (2.135) is not an independent quantity in the cold-fluid limit, and thus there is no standard notation to relate it to. Nonetheless, it is clear that it represents a correlation between the two transverse velocities.

Equations (2.126) - (2.135) define physical distribution quantities in terms of the matrix elements, but for purposes of computation we require the inverse relations, i.e.,

$$M_{\tilde{x}\tilde{x}} = \bar{a}^2,\tag{2.140}$$

$$M_{\tilde{y}\tilde{y}} = \bar{b}^2,\tag{2.141}$$

$$M_{\tilde{x}\tilde{y}} = 0,\tag{2.142}$$

$$M_{\tilde{x}p_{\tilde{x}}} = \left(\sqrt{\csc^2(2\theta_{\tilde{x}p_{\tilde{x}}}) - \frac{\bar{\epsilon}_{\tilde{x}p_{\tilde{x}}}^2}{M_{\tilde{x}\tilde{x}}^2}} - \cot(2\theta_{\tilde{x}p_{\tilde{x}}}) \right) M_{\tilde{x}\tilde{x}},\tag{2.143}$$

$$M_{p_{\tilde{x}}p_{\tilde{x}}} = M_{\tilde{x}\tilde{x}} - 2M_{\tilde{x}p_{\tilde{x}}} \cot(2\theta_{\tilde{x}p_{\tilde{x}}}),\tag{2.144}$$

$$M_{\tilde{y}p_{\tilde{y}}} = \left(\sqrt{\csc^2(2\theta_{\tilde{y}p_{\tilde{y}}}) - \frac{\bar{\epsilon}_{\tilde{y}p_{\tilde{y}}}^2}{M_{\tilde{y}\tilde{y}}^2}} - \cot(2\theta_{\tilde{y}p_{\tilde{y}}}) \right) M_{\tilde{y}\tilde{y}},\tag{2.145}$$

$$M_{p_{\tilde{y}}p_{\tilde{y}}} = M_{\tilde{y}\tilde{y}} - 2M_{\tilde{y}p_{\tilde{y}}} \cot(2\theta_{\tilde{y}p_{\tilde{y}}}),\tag{2.146}$$

$$M_{\tilde{x}p_{\tilde{y}}} = \frac{1}{2} (M_{\tilde{x}\tilde{x}} - M_{p_{\tilde{y}}p_{\tilde{y}}}) \tan(2\theta_{\tilde{x}p_{\tilde{y}}}),\tag{2.147}$$

$$M_{\tilde{y}p_{\tilde{x}}} = \frac{1}{2} (M_{\tilde{y}\tilde{y}} - M_{p_{\tilde{x}}p_{\tilde{x}}}) \tan(2\theta_{\tilde{y}p_{\tilde{x}}}),\tag{2.148}$$

$$M_{p_{\tilde{x}}p_{\tilde{y}}} = \frac{1}{2} (M_{p_{\tilde{x}}p_{\tilde{x}}} - M_{p_{\tilde{y}}p_{\tilde{y}}}) \tan(2\theta_{p_{\tilde{x}}p_{\tilde{y}}}).\tag{2.149}$$

This set of equations fully specifies all 10 independent components of the beam-aligned distribution matrix $\underline{\underline{\tilde{\mathbf{M}}}}$ in terms of projection quantities in the various 2-dimensional subspaces. With these in hand, as well as the relationship $\underline{\underline{\mathbf{M}}} = \underline{\underline{\mathbf{R}}}^{-1} \cdot \underline{\underline{\tilde{\mathbf{M}}}} \cdot \underline{\underline{\mathbf{R}}}$, the matrix equation of motion (2.104) can be integrated to determine the evolution of the particle distribution function. Numerical examples of such integrations are discussed later in Sections 5.7, 6.2.4, and 6.3.3.

3 Single Particle Dynamics

3.1 Overview

With the elements of the force matrix $\underline{\mathbf{F}}$ and the distribution matrix $\underline{\mathbf{M}}$ specified, we can proceed to solve Eq. (2.104) for the evolution of the particle phase-space distribution, given a set of initial and boundary conditions. This is a set of 10 coupled, nonlinear, first-order differential equations, and thus cannot be solved in full generality. Fortunately, we do not require general solutions. We are only interested in solutions which satisfy some desired beam envelope evolution.

New devices are increasingly sought for high-power, high-frequency operation [13] [18]. In this régime, since high voltage is often limited by engineering considerations, high-current (and thus space-charge-dominated) beams are desirable. Moreover, since high-frequency applications require small-scale-length structures, high aspect-ratio elliptic beams are sought because they serve the dual purpose of allowing coupling to higher frequencies (by minimizing their minor axis) and carrying large current (by maximizing their area). Since most elliptic beam device concepts involve coupling to planar structures (comparatively easy to fabricate), it is generally required that the beam be confined without bending, expanding, or rotating. For these reasons, we focus on finding solutions for paraxial, space-charge-dominated, non-twisting elliptic beams with $|\theta| \ll 1$.

The task of finding a desired beam solution to Eq. (2.104) can be quite challenging due to the large number of free parameters and functions embedded in the initial and boundary conditions, e.g., the beam current, the axial potential, the applied fields, the starting values for the beam envelope quantities, etc. If the initial and boundary conditions are not fixed properly, Eq. (2.104) will not yield a confined beam solution. The beam may immediately expand to impact upon its containing vessel, fail to maintain laminar flow, change direction, or otherwise frustrate expectations. Clearly, certain constraints on the initial and boundary conditions are required in order to ensure a desired beam outcome.

Let us define a desired beam as one in which the trajectory of each particle (\bar{x}, \bar{y}) very nearly satisfies a desired trajectory $(\bar{x}_{\text{des}}, \bar{y}_{\text{des}})$ as it propagates longitudinally such that

$$(\bar{x}, \bar{y}) = (\bar{x}_{\text{des}}, \bar{y}_{\text{des}}) + (\delta\bar{x}, \delta\bar{y}), \quad (3.1)$$

where the perturbations satisfy

$$|\delta\bar{x}| \ll \bar{a}, \quad (3.2)$$

$$|\delta\bar{y}| \ll \bar{b}. \quad (3.3)$$

Moreover, let us assume that the trajectories and axial potential are slowly-varying over a dimensionless longitudinal length scale \bar{S}_{des} such that

$$\left| \frac{1}{\bar{a}} \frac{d\bar{x}}{d\bar{z}} \right| \ll \frac{1}{\bar{S}_{\text{des}}}, \quad (3.4)$$

$$\left| \frac{1}{\bar{b}} \frac{d\bar{y}}{d\bar{z}} \right| \ll \frac{1}{\bar{S}_{\text{des}}}, \quad (3.5)$$

$$\left| \frac{1}{\bar{\Phi}_{00}} \frac{d\bar{\Phi}_{00}}{d\bar{z}} \right| \ll \frac{1}{\bar{S}_{\text{des}}}. \quad (3.6)$$

Notice the overbar notation; we employ the dimensionless forms in this chapter.

Since we are interested in space-charge-dominated beams, we ignore the effect of emittance in the beam dynamics [16] [27] [28] and concentrate, for the moment, on the equations of motion for single particles in a self-similar cold-fluid. By a self-similar cold-fluid, we mean that the transverse flow velocity of a fluid element is proportional to the transverse displacement of that fluid element.

In this chapter, we return to the dimensionless single particle equation of motion (2.88) in order to derive some of the constraints on the boundary and initial conditions in several limiting cases. In Section 3.2, we examine particle dynamics in the wide (\bar{x}) dimension of the beam and apply the conditions of Eqs. (3.2) and (3.4), yielding certain constraints on the applied fields. Similarly, in Section 3.3, we examine particle dynamics in the narrow (\bar{y}) dimension of the beam and apply the conditions of Eqs. (3.3) and (3.5), yielding other constraints on the applied fields. In Section 3.4, these constraints on the applied fields are combined and analyzed in numerous cases, several of which result in practical, realizable equilibrium configurations which will be the subject of later chapters.

3.2 Wide-Dimension Dynamics

3.2.1 Axial and Quadrupole Magnetic Field Contributions to the Momentum

Let us examine Eq. (2.88). We begin by considering evolution in (\bar{x}, \bar{p}_x) , involving the terms $\bar{F}_{\bar{x}\bar{p}_x}$, $\bar{F}_{\bar{p}_x\bar{x}}$, $\bar{F}_{\bar{p}_x\bar{y}}$, and $\bar{F}_{\bar{p}_y\bar{p}_x}$. Since $|\theta| \ll 1$, by assumption, the $\bar{\Phi}_{11}^{\rho 0}$ term in the electrostatic potential in Eq. (2.93) can be made small [see Eqs. (2.5)]. In addition, if we set the applied quadrupole electrostatic field angle small such that $\tan 2\theta_Q \ll 1$, the $\bar{\Phi}_{11}$ term in Eq. (2.93) also becomes small [see Eqs. (2.34) and (2.40)], and the following ordering is suggested

$$\left| -\bar{\Phi}_{11} + \beta^2 \bar{\Phi}_{11}^{\rho 0} \right| \ll \left| \beta \frac{d\bar{B}_z}{d\bar{z}} (1 - r_m) \right|. \quad (3.7)$$

This implies

$$\bar{F}_{\bar{p}_x\bar{y}} \cong \alpha_\lambda \frac{d\bar{B}_z}{d\bar{z}} (1 - r_m), \quad (3.8)$$

and that the momentum \bar{p}_x evolves according to

$$\begin{aligned} \frac{d\bar{p}_x}{d\bar{z}} &= \bar{F}_{\bar{p}_x\bar{x}}\bar{x} + \bar{F}_{\bar{p}_x\bar{y}}\bar{y} + \bar{F}_{\bar{p}_x\bar{p}_y}\bar{p}_y \\ &= \frac{\alpha_\lambda}{\beta} \left[\bar{x}(-2\bar{\Phi}_{20} - \beta\bar{B}_Q + 2\beta^2\bar{\Phi}_{20}^{\rho 0}) + \bar{y}\beta \frac{d\bar{B}_z}{d\bar{z}} (1 - r_m) + \bar{p}_y\gamma^{-1}\bar{B}_z \right]. \end{aligned} \quad (3.9)$$

It is useful to split Eq. (3.9) (and \bar{p}_x) into two parts as

$$\bar{p}_x \equiv \bar{p}_x^z + \bar{p}_x^Q, \quad (3.10)$$

where

$$\frac{d\bar{p}_x^z}{d\bar{z}} = \frac{\alpha_\lambda}{\beta} \left(\bar{y}\beta \frac{d\bar{B}_z}{d\bar{z}} (1 - r_m) + \bar{p}_y\gamma^{-1}\bar{B}_z \right), \quad (3.11)$$

$$\frac{d\bar{p}_x^Q}{d\bar{z}} = \frac{\alpha_\lambda}{\beta} \bar{x}(-2\bar{\Phi}_{20} - \beta\bar{B}_Q + 2\beta^2\bar{\Phi}_{20}^{\rho 0}). \quad (3.12)$$

It is evident that \bar{p}_x^z is generated by the axial magnetic field \bar{B}_z , while \bar{p}_x^Q is generated by the quadrupole magnetic field \bar{B}_Q . We consider the evolution of these two parts of the momentum, separately, in Sections 3.2.2 and 3.2.3.

3.2.2 Momentum Evolution due to the Axial Magnetic Field

Combining Eqs. (3.11) and (2.78), we find

$$\begin{aligned} \frac{d\bar{p}_x^z}{d\bar{z}} &= \alpha_\lambda \left(\bar{y} \frac{d\bar{B}_z}{d\bar{z}} (1 - r_m) + \frac{d\bar{y}}{d\bar{z}} \bar{B}_z \right) \\ &= \alpha_\lambda \left(\frac{d}{d\bar{z}} [\bar{y} \bar{B}_z (1 - r_m)] + \bar{B}_z r_m \frac{d\bar{y}}{d\bar{z}} + \bar{B}_z \bar{y} \frac{dr_m}{d\bar{z}} \right). \end{aligned} \quad (3.13)$$

We shall take $|r_m| \ll 1$ which allows us to obtain approximately

$$\bar{p}_x^z(\bar{z}) \cong \alpha_\lambda \bar{y} \bar{B}_z (1 - r_m) + \left\{ \bar{p}_x^z(\bar{z}_0) - \alpha_\lambda \bar{y}(\bar{z}_0) \bar{B}_z(\bar{z}_0) [1 - r_m(\bar{z}_0)] \right\}, \quad (3.14)$$

where \bar{z}_0 denotes an initial value of the axial coordinate \bar{z} .

3.2.3 Momentum Evolution due to the Quadrupole Magnetic Field

Combining Eqs. (3.12) and (2.32), we find

$$\frac{d\bar{p}_x^Q}{d\bar{z}} = \frac{\alpha_\lambda}{\beta} \bar{x} \left(-2\bar{\Phi}_{20}^\rho - 2\bar{\Phi}_Q - \beta \bar{B}_Q + 2\beta^2 \bar{\Phi}_{20}^{\rho 0} \right). \quad (3.15)$$

Let us define a “residual” quadrupole field $\delta \bar{B}_Q$ through the equation

$$\beta \delta \bar{B}_Q \equiv (\beta \bar{B}_Q + 2\bar{\Phi}_Q) + 2\bar{\Phi}_{20}^\rho - 2\beta^2 \bar{\Phi}_{20}^{\rho 0}, \quad (3.16)$$

or, equivalently, using Eqs. (2.4) and (2.38) to replace the self-field terms,

$$\beta \delta \bar{B}_Q \equiv (\beta \bar{B}_Q + 2\bar{\Phi}_Q) - \left(\frac{2\bar{I}}{\bar{a}\bar{b}\beta\gamma^2} + \frac{1}{2} \bar{\Phi}_{00}'' \right) \frac{\bar{a} + \bar{b} - (\bar{a} - \bar{b}) \cos 2\theta}{\bar{a} + \bar{b}}. \quad (3.17)$$

Rewriting Eq. (3.15) in terms of the residual quadrupole field defined in Eq. (3.16), we find

$$\frac{d\bar{p}_x^Q}{d\bar{z}} = -a_s \bar{x} \delta \bar{B}_Q. \quad (3.18)$$

Notice that the magnetic quadrupole term \bar{B}_Q and electric quadrupole term $\bar{\Phi}_Q$ enter Eq. (3.17) in essentially the same manner; both quadrupole fields have the same effect on beam dynamics. As long as the sum $\beta \bar{B}_Q + 2\bar{\Phi}_Q$ is held constant, we can trade off between an applied electric quadrupole and an applied magnetic quadrupole as convenient.

3.2.4 Displacement Evolution and Ordering Conditions

The evolution of the displacement \bar{x} is determined by the first component of Eq. (2.88), i.e.,

$$\frac{d\bar{x}}{d\bar{z}} = \bar{p}_x \bar{F}_{\bar{x}\bar{p}_x}. \quad (3.19)$$

Making use of Eqs. (3.1), (3.10), and (2.91), we can express Eq. (3.19) as

$$\frac{d(\bar{x}_{\text{des}} + \delta\bar{x})}{d\bar{z}} = \frac{\bar{p}_x^Q + \bar{p}_x^z}{\gamma\beta}. \quad (3.20)$$

We make the ansatz that the terms in Eq. (3.20) can be equated piecewise to yield

$$\frac{d(\bar{x}_{\text{des}} + \delta\bar{x}^Q)}{d\bar{z}} = \frac{\bar{p}_x^Q}{\gamma\beta}, \quad (3.21)$$

$$\frac{d\delta\bar{x}^z}{d\bar{z}} = \frac{\bar{p}_x^z}{\gamma\beta}, \quad (3.22)$$

where we've defined

$$\delta\bar{x} = \delta\bar{x}^Q + \delta\bar{x}^z. \quad (3.23)$$

Note that this association of the desired trajectory \bar{x}_{des} with the quadrupole field is the most natural choice. We can see that Eq. (3.14) couples the \bar{x} and \bar{y} motion through the axial magnetic field \bar{B}_z , leading to a rotation of the beam. By associating this rotational momentum \bar{p}_x^z with only a perturbed displacement $\delta\bar{x}^z$ in Eq. (3.22), we hope to ensure that the rotation remains small, i.e., $|\theta| \ll 1$.

The constraints on the trajectories described in Section 3.1 imply certain restrictions on the allowed forms and magnitude of the applied fields. For example, we can obtain a condition on $\delta\bar{B}_Q$ by combining Eqs. (3.21) and (3.4) to find

$$\left| \frac{\bar{p}_x^Q}{\bar{a}\gamma\beta} \right| \ll \frac{1}{\bar{S}_{\text{des}}}, \quad (3.24)$$

which we can rewrite using Eqs. (3.18) as

$$\left| \frac{\alpha_\lambda}{\bar{a}\gamma\beta} \int_{\bar{S}_{\text{des}}} \bar{x} \delta\bar{B}_Q d\bar{z} \right| \ll \frac{1}{\bar{S}_{\text{des}}}, \quad (3.25)$$

where the limit on the integral denotes any length of order \bar{S}_{des} or smaller. We can make use of $\bar{x} \cong \bar{x}_{\text{des}}$ [see Eq. (3.2)] and the fact that \bar{x}_{des} is nearly constant over a length scale of \bar{S}_{des} [see Eq. (3.4)] in order to take it outside of the integral appearing in Eq. (3.25). With these simplifications, Eq. (3.25) becomes

$$\left| \frac{\alpha_\lambda}{\gamma\beta} \frac{\bar{x}_{\text{des}}}{\bar{a}} \int_{\bar{S}_{\text{des}}} \delta\bar{B}_Q d\bar{z} \right| \ll \frac{1}{\bar{S}_{\text{des}}}. \quad (3.26)$$

Because Eq. (3.26) must hold for all trajectories \bar{x}_{des} in the beam, we can look at the extremal case, i.e., $\bar{x}_{\text{des}} \rightarrow \bar{a}$, which gives the more stringent condition

$$\left| \frac{\alpha_\lambda}{\gamma\beta} \int_{\bar{S}_{\text{des}}} \delta\bar{B}_Q d\bar{z} \right| \ll \frac{1}{\bar{S}_{\text{des}}}, \quad (3.27)$$

implying either $|\delta\bar{B}_Q \alpha_\lambda / \gamma\beta| \ll \bar{S}_{\text{des}}^{-2}$ or else $\delta\bar{B}_Q$ is oscillatory with a negligible integral as defined by Eq. (3.27). The residual quadrupole field $\delta\bar{B}_Q$ must satisfy Eq. (3.27) in order to ensure that particle trajectories do not vary too rapidly in the wide dimension of the beam, which would invalidate the expressions for the self-fields, such as those given in Section 2.2.2.

Similarly, we can obtain a condition on \bar{B}_z by combining Eqs. (3.2) and (3.22) to yield

$$\left| \frac{1}{\bar{a}} \int_{\bar{S}_{\text{des}}} \frac{\bar{p}_x^z}{\gamma\beta} d\bar{z} \right| \ll 1. \quad (3.28)$$

Using Eq. (3.14) to substitute for \bar{p}_x^z in Eq. (3.28), we find

$$\left| \frac{1}{\bar{a}} \int_{\bar{S}_{\text{des}}} \frac{\alpha_\lambda \bar{y} \bar{B}_z (1 - r_m) + \left\{ \bar{p}_x^z(\bar{z}_0) - \alpha_\lambda \bar{y}(\bar{z}_0) \bar{B}_z(\bar{z}_0) [1 - r_m(\bar{z}_0)] \right\}}{\gamma \beta} d\bar{z} \right| \ll 1. \quad (3.29)$$

We can choose the initial values at $\bar{z} = \bar{z}_0$ such that the term in braces vanishes in Eq. (3.29). We can also use of $\bar{y} \cong \bar{y}_{\text{des}}$ [see Eq. (3.3)] and the fact that \bar{y}_{des} is nearly constant over a length scale of \bar{S}_{des} [see Eq. (3.5)] in order to take it outside of the integral appearing in Eq. (3.29). Similarly, Eq. (3.6) implies that we can take the product $\gamma \beta$ outside of the integral, as well. With these simplifications, and noting that $r_m \ll 1$, Eq. (3.29) becomes

$$\left| \frac{\bar{y}_{\text{des}}}{\bar{a}} \frac{\alpha_\lambda}{\gamma \beta} \int_{\bar{S}_{\text{des}}} \bar{B}_z d\bar{z} \right| \ll 1. \quad (3.30)$$

Once again, looking at the extremal case, i.e., $\bar{y}_{\text{des}} \rightarrow \bar{b}$, Eq. (3.30) becomes more stringent, yielding

$$\left| \frac{\bar{b}}{\bar{a}} \frac{\alpha_\lambda}{\gamma \beta} \int_{\bar{S}_{\text{des}}} \bar{B}_z d\bar{z} \right| \ll 1. \quad (3.31)$$

which implies either $\left| \bar{B}_z \bar{b} \alpha_\lambda / (\bar{a} \gamma \beta) \right| \ll \bar{S}_{\text{des}}^{-1}$ or else \bar{B}_z is oscillatory with a negligible integral as defined by Eq. (3.31). The axial magnetic field \bar{B}_z must satisfy Eq. (3.31) to ensure that particle trajectory perturbations in the wide dimension of the beam are not large compared to the beam size.

3.3 Narrow-Dimension Dynamics

3.3.1 Momentum Evolution

Let us examine Eq. (2.88) and consider evolution in (\bar{y}, \bar{p}_y) , involving the terms $\bar{F}_{\bar{y}\bar{p}_y}$, $\bar{F}_{\bar{p}_y\bar{y}}$, $\bar{F}_{\bar{p}_y\bar{x}}$, and $\bar{F}_{\bar{p}_y\bar{p}_x}$. The momentum \bar{p}_y evolves according to

$$\frac{d\bar{p}_y}{d\bar{z}} = \bar{F}_{\bar{p}_y\bar{y}} \bar{y} + \bar{F}_{\bar{p}_y\bar{p}_x} \bar{p}_x + \bar{F}_{\bar{p}_y\bar{x}} \bar{x}, \quad (3.32)$$

and we shall examine each term in Eq. (3.32) in turn.

Combining Eqs. (2.95) and (2.33), we can express the first term $\overline{F}_{\overline{p}_y \overline{y}}$ in Eq. (3.32) as

$$\overline{F}_{\overline{p}_y \overline{y}} = \frac{\alpha_\lambda}{\beta} \overline{y} \left(-2\overline{\Phi}_{02}^\rho + 2\overline{\Phi}_Q + \beta \overline{B}_Q + 2\beta^2 \overline{\Phi}_{02}^{\rho 0} \right), \quad (3.33)$$

which can be further simplified using Eq. (3.16) to yield

$$\overline{F}_{\overline{p}_y \overline{y}} = \frac{\alpha_\lambda}{\beta} \overline{y} \left[-2(\overline{\Phi}_{20}^\rho + \overline{\Phi}_{02}^\rho) + \beta \delta \overline{B}_Q + 2\beta^2 (\overline{\Phi}_{20}^{\rho 0} + \overline{\Phi}_{02}^{\rho 0}) \right]. \quad (3.34)$$

Making use of Eqs. (2.4), (2.6), and (2.35), we can express Eq. (3.34) as

$$\overline{F}_{\overline{p}_y \overline{y}} = \frac{\alpha_\lambda}{\beta} \overline{y} \left(\frac{4\overline{I}}{\overline{a}\overline{b}\beta\gamma^2} + \overline{\Phi}_{00}'' + \beta \delta \overline{B}_Q \right). \quad (3.35)$$

The second term $\overline{F}_{\overline{p}_y \overline{p}_x}$ in Eq. (3.32) can be expressed using Eqs. (2.96), (3.10), and (3.14) as

$$\overline{F}_{\overline{p}_y \overline{p}_x} \cong -\frac{\alpha_\lambda \overline{B}_z}{\gamma\beta} \left[\alpha_\lambda \overline{y} \overline{B}_z (1 - r_m) + \overline{p}_x^Q \right], \quad (3.36)$$

where we have once again chosen the initial conditions such that the term in braces in Eq. (3.14) vanishes.

The final term $\overline{F}_{\overline{p}_y \overline{x}}$ in Eq. (3.32) can be written using Eq. (2.94) as

$$\overline{F}_{\overline{p}_y \overline{x}} = \frac{\alpha_\lambda \overline{x}}{\beta} \left(-\overline{\Phi}_{11} + \beta^2 \overline{\Phi}_{11}^{\rho 0} - r_m \beta \frac{d\overline{B}_z}{d\overline{z}} \right). \quad (3.37)$$

By paralleling the argument given at the beginning of Section 3.2.1, we can see that for $|\theta| \ll 1$, $|\tan 2\theta_Q| \ll 1$, and $|r_m| \ll 1$, the $\overline{F}_{\overline{p}_y \overline{x}}$ term can be made negligibly small. This allows us to rewrite Eq. (3.32) as

$$\frac{d\overline{p}_y}{d\overline{z}} \cong \frac{\alpha_\lambda \overline{y}}{\beta} \left(\frac{4\overline{I}}{\overline{a}\overline{b}\beta\gamma^2} + \overline{\Phi}_{00}'' + \beta \delta \overline{B}_Q \right) - \frac{\alpha_\lambda \overline{B}_z}{\gamma\beta} \left[\alpha_\lambda \overline{y} \overline{B}_z (1 - r_m) + \overline{p}_x^Q \right]. \quad (3.38)$$

3.3.2 Displacement Evolution and Ordering Conditions

The evolution of the displacement \overline{y} is determined by the third component of Eq. (2.88), i.e.,

$$\frac{d\bar{y}}{d\bar{z}} = \bar{p}_y \bar{F}_{y\bar{p}_y}. \quad (3.39)$$

We can obtain a condition on \bar{p}_y by combining Eqs. (3.39) and (3.5) to yield

$$\left| \frac{\bar{p}_y}{\bar{b}\gamma\beta} \right| \ll \frac{1}{\bar{S}_{\text{des}}}. \quad (3.40)$$

If we now make the substitution

$$\bar{p}_y = \int_{\bar{s}_{\text{des}}} \frac{d\bar{p}_y}{d\bar{z}} d\bar{z}, \quad (3.41)$$

into Eq. (3.40), we find

$$\left| \frac{1}{\bar{b}\gamma\beta} \int_{\bar{s}_{\text{des}}} \frac{d\bar{p}_y}{d\bar{z}} d\bar{z} \right| \ll \frac{1}{\bar{S}_{\text{des}}}. \quad (3.42)$$

which implies either $\left| \bar{p}'_y / (\bar{b}\gamma\beta) \right| \ll \bar{S}_{\text{des}}^{-2}$ or else \bar{p}'_y is oscillatory with a negligible integral as defined by Eq. (3.42). The derivative of the narrow-dimension momentum \bar{p}'_y must satisfy Eq. (3.42) in order to ensure that particle trajectories do not vary too rapidly in the narrow dimension of the beam, which would invalidate the expressions for the self-fields, such as those given in Section 2.2.2.

3.4 Survey of Ordering Regimes for Applied Fields

3.4.1 Summary of Ordering Regimes

In Section 3.2.4 we obtained conditions on the applied longitudinal magnetic field \bar{B}_z and the residual quadrupole field $\delta\bar{B}_Q$ which must be satisfied in order to maintain desired trajectories of the form given in Eq. (3.1). A similar condition was obtained on the derivative of the momentum \bar{p}'_y in Section 3.3.2. We summarize these conditions here, for convenience.

We may choose either a small $\delta\bar{B}_Q$ satisfying

$$\left| \frac{\alpha_\lambda}{\gamma\beta} \delta\bar{B}_Q \right| \ll \frac{1}{\bar{S}_{\text{des}}^2}, \quad (3.43)$$

or an oscillatory $\delta \bar{B}_Q$ satisfying

$$\left| \frac{\alpha_\lambda}{\gamma\beta} \int_{\bar{s}_{\text{des}}} \delta \bar{B}_Q d\bar{z} \right| \ll \frac{1}{\bar{S}_{\text{des}}}; \quad (3.44)$$

we may choose either a small \bar{B}_z satisfying

$$\left| \frac{\alpha_\lambda \bar{b}}{\gamma\beta \bar{a}} \bar{B}_z \right| \ll \frac{1}{\bar{S}_{\text{des}}}, \quad (3.45)$$

or an oscillatory \bar{B}_z satisfying

$$\left| \frac{\alpha_\lambda \bar{b}}{\gamma\beta \bar{a}} \int_{\bar{s}_{\text{des}}} \bar{B}_z d\bar{z} \right| \ll 1; \quad (3.46)$$

and we may choose either a small \bar{p}'_y satisfying

$$\left| \frac{1}{\bar{b}\gamma\beta} \frac{d\bar{p}'_y}{d\bar{z}} \right| \ll \frac{1}{\bar{S}_{\text{des}}^2}, \quad (3.47)$$

or an oscillatory \bar{p}'_y satisfying

$$\left| \frac{1}{\bar{b}\gamma\beta} \int_{\bar{s}_{\text{des}}} \frac{d\bar{p}'_y}{d\bar{z}} d\bar{z} \right| \ll \frac{1}{\bar{S}_{\text{des}}}. \quad (3.48)$$

We also reproduce Eq. (3.24) here,

$$\left| \frac{\bar{p}_x^Q}{\bar{a}\gamma\beta} \right| \ll \frac{1}{\bar{S}_{\text{des}}}, \quad (3.49)$$

which must hold independent of any of the choices above.

In the next several subsections, we apply various combinations of these alternative ordering conditions [Eqs. (3.43) or (3.44), (3.45) or (3.46), (3.47) or (3.48), and (3.49)] and deduce the implications for the elliptic beam equilibrium.

3.4.2 Small Fields, Non-Oscillatory Regime

The simplest possible ordering is in the *small fields, non-oscillatory* regime, i.e., Eqs. (3.43), (3.45), and (3.47). In this regime, Eq. (3.38) can be rearranged as

$$\begin{aligned} \frac{\alpha_\lambda \bar{y}}{\beta} \left(\frac{4\bar{I}}{\bar{a}\bar{b}\beta\gamma^2} + \bar{\Phi}_{00}'' \right) &= \frac{d\bar{p}_y}{d\bar{z}} - \alpha_\lambda \bar{y} \delta \bar{B}_Q + \frac{\alpha_\lambda \bar{B}_z}{\gamma\beta} \left[\alpha_\lambda \bar{y} \bar{B}_z (1 - r_m) + \bar{p}_x^Q \right], \\ \left| \frac{\alpha_\lambda \bar{y}}{\beta} \left(\frac{4\bar{I}}{\bar{a}\bar{b}\beta\gamma^2} + \bar{\Phi}_{00}'' \right) \right| &\sim O \left(\bar{S}_{\text{des}}^{-2} \left[2|\bar{y}\gamma\beta| + 2 \left| \frac{\bar{x}^2}{\bar{y}} \beta\gamma \right| \right] \right). \end{aligned} \quad (3.50)$$

which implies

$$\left| \frac{\alpha_\lambda \bar{y}}{\beta} \left(\frac{4\bar{I}}{\bar{a}\bar{b}\beta\gamma^2} + \bar{\Phi}_{00}'' \right) \right| \sim O \left(\frac{1}{\bar{S}_{\text{des}}^2} \left[2\bar{b}\gamma\beta + 2 \frac{\bar{a}^2}{\bar{b}} \beta\gamma \right] \right), \quad (3.51)$$

where we have used Eqs. (3.43), (3.45), (3.47), and (3.49) to rewrite the right-hand side of Eq. (3.51) to show that it becomes negligible for large \bar{S}_{des} .

If the beam is coasting (i.e., not accelerating, therefore $\bar{\Phi}_{00}'' \cong 0$), the *small fields, non-oscillatory* regime will require either a small length scale \bar{S}_{des} (implying that the right side is *not* negligible) or low current (low self-fields) such that this situation essentially corresponds to an unfocused beam expanding under its own space charge. On the other hand, the current and axial potential terms can negate one another to satisfy Eq. (3.51) in regions where the beam is accelerating. This corresponds to the Child-Langmuir [29] space-charge flow solution, which is applied to the beam formation problem in Chapter 4. For a coasting beam, however, the *small fields, non-oscillatory* regime does not provide a satisfactory equilibrium.

3.4.3 Small Fields, Momentum Oscillation Regime

Suppose we relax the above constraints somewhat and allow \bar{p}_y' to be oscillatory while we maintain small fields, i.e., Eqs. (3.43), (3.45), and (3.48). In this *small fields, momentum oscillation* regime, Eq. (3.38) can be rearranged as

$$\frac{d\bar{p}_y}{d\bar{z}} - \frac{\alpha_\lambda \bar{y}}{\beta} \left(\frac{4\bar{I}}{\bar{a}\bar{b}\beta\gamma^2} + \bar{\Phi}_{00}'' \right) = \alpha_\lambda \bar{y} \delta \bar{B}_Q - \frac{\alpha_\lambda \bar{B}_z}{\gamma\beta} (\alpha_\lambda \bar{y} \bar{B}_z + \bar{p}_x^Q), \quad (3.52)$$

which implies

$$\frac{d\bar{p}_y}{d\bar{z}} - \frac{\alpha_\lambda \bar{y}}{\beta} \left(\frac{4\bar{I}}{\bar{a}\bar{b}\beta\gamma^2} + \bar{\Phi}'_{00} \right) \sim \mathcal{O} \left(\frac{1}{\bar{S}_{\text{des}}^2} \left[\bar{b}\gamma\beta + 2\frac{\bar{a}^2}{\bar{b}}\beta\gamma \right] \right). \quad (3.53)$$

Integrating Eq. (3.53) produces

$$\int_{\bar{S}_{\text{des}}} \frac{d\bar{p}_y}{d\bar{z}} d\bar{z} - \frac{\alpha_\lambda \bar{y}}{\beta} \left(\frac{4\bar{I} \bar{S}_{\text{des}}}{\bar{a}\bar{b}\beta\gamma^2} + \bar{\Phi}'_{00} \right) \sim \mathcal{O} \left(\frac{1}{\bar{S}_{\text{des}}} \left[\bar{b}\gamma\beta + 2\frac{\bar{a}^2}{\bar{b}}\beta\gamma \right] \right), \quad (3.54)$$

which can be simplified, using Eq. (3.48), to

$$\frac{\alpha_\lambda \bar{y}}{\beta} \left(\frac{4\bar{I} \bar{S}_{\text{des}}}{\bar{a}\bar{b}\beta\gamma^2} + \bar{\Phi}'_{00} \right) \sim \mathcal{O} \left(\frac{1}{\bar{S}_{\text{des}}} \left[2\bar{b}\gamma\beta + 2\frac{\bar{a}^2}{\bar{b}}\beta\gamma \right] \right). \quad (3.55)$$

By conservation of charge, the current is held fixed, and so cannot be oscillatory. The axial potential term can be oscillatory (as in the case of certain types of electrostatic focusing), but it is clear from Eq. (3.55) that a net accelerating electric field (proportional to $\bar{\Phi}'_{00}$) is required to counterbalance the current term. Thus we conclude that the *small fields, momentum oscillation* regime can only produce solutions for accelerating beams of the same type that are produced more simply by the *small fields, non-oscillatory* regime discussed in Section 3.4.2. Moreover, we are led to the conclusion that a useful non-accelerating beam solution will require at least \bar{B}_z or $\delta\bar{B}_Q$ to be oscillatory.

3.4.4 Oscillatory Residual Quadrupole Field Regime

Suppose we allow an *oscillatory residual quadrupole field* $\delta\bar{B}_Q$ while we maintain \bar{B}_z and \bar{p}'_y small, i.e., Eqs. (3.44), (3.45), and (3.47). In this regime, Eq. (3.38) can be rearranged as

$$\frac{\alpha_\lambda \bar{y}}{\beta} \left(\frac{4\bar{I}}{\bar{a}\bar{b}\beta\gamma^2} + \bar{\Phi}'_{00} + \beta\delta\bar{B}_Q \right) = \frac{d\bar{p}_y}{d\bar{z}} + \frac{\alpha_\lambda \bar{B}_z}{\gamma\beta} (\alpha_\lambda \bar{y} \bar{B}_z + \bar{p}_x^Q), \quad (3.56)$$

which implies

$$\frac{\alpha_\lambda \bar{y}}{\beta} \left(\frac{4\bar{I}}{\bar{a}\bar{b}\beta\gamma^2} + \bar{\Phi}'_{00} + \beta\delta\bar{B}_Q \right) \sim \mathcal{O} \left(\frac{1}{\bar{S}_{\text{des}}^2} \left[\bar{b}\gamma\beta + 2\frac{\bar{a}^2}{\bar{b}}\beta\gamma \right] \right). \quad (3.57)$$

Integrating Eq. (3.57) produces

$$\frac{\alpha_\lambda \bar{y}}{\beta} \left(\frac{4\bar{I} \bar{S}_{\text{des}}}{\bar{a}\bar{b}\beta\gamma^2} + \bar{\Phi}'_{00} + \int_{\bar{S}_{\text{des}}} \beta \delta \bar{B}_Q d\bar{z} \right) \sim \mathcal{O} \left(\frac{1}{\bar{S}_{\text{des}}} \left[\bar{b}\gamma\beta + 2\frac{\bar{a}^2}{\bar{b}}\beta\gamma \right] \right), \quad (3.58)$$

which can be simplified, using Eq. (3.44), to

$$\frac{\alpha_\lambda \bar{y}}{\beta} \left(\frac{4\bar{I} \bar{S}_{\text{des}}}{\bar{a}\bar{b}\beta\gamma^2} + \bar{\Phi}'_{00} \right) \sim \mathcal{O} \left(\frac{1}{\bar{S}_{\text{des}}} \left[2\bar{b}\gamma\beta + 2\frac{\bar{a}^2}{\bar{b}}\beta\gamma \right] \right). \quad (3.59)$$

This is the same result as Eq. (3.55), and thus we conclude that simply allowing an oscillatory $\delta \bar{B}_Q$, while maintaining a small \bar{p}'_y and \bar{B}_z does not permit any qualitatively new solutions.

3.4.5 Small Axial Field Regime

We try maintaining a *small axial field* \bar{B}_z , while allowing \bar{p}'_y and $\delta \bar{B}_Q$ to be oscillatory, i.e., Eqs. (3.44), (3.45), and (3.48). In this regime, Eq. (3.38) can be rearranged as

$$\frac{d\bar{p}_y}{d\bar{z}} - \frac{\alpha_\lambda \bar{y}}{\beta} \left(\frac{4\bar{I}}{\bar{a}\bar{b}\beta\gamma^2} + \bar{\Phi}''_{00} + \beta \delta \bar{B}_Q \right) = -\frac{\alpha_\lambda \bar{B}_z}{\gamma\beta} (\alpha_\lambda \bar{y} \bar{B}_z + \bar{p}_x^Q), \quad (3.60)$$

which implies

$$\frac{d\bar{p}_y}{d\bar{z}} - \frac{\alpha_\lambda \bar{y}}{\beta} \left(\frac{4\bar{I}}{\bar{a}\bar{b}\beta\gamma^2} + \bar{\Phi}''_{00} + \beta \delta \bar{B}_Q \right) \sim \mathcal{O} \left(\bar{S}_{\text{des}}^{-2} 2\frac{\bar{a}^2}{\bar{b}}\beta\gamma \right). \quad (3.61)$$

After integrating Eq. (3.61) and making use of Eqs. (3.44) and (3.48), we again find

$$\frac{\alpha_\lambda \bar{y}}{\beta} \left(\frac{4\bar{I} \bar{S}_{\text{des}}}{\bar{a}\bar{b}\beta\gamma^2} + \bar{\Phi}'_{00} \right) \sim \mathcal{O} \left(2\bar{b}\gamma\beta + 2\frac{\bar{a}^2}{\bar{b}}\beta\gamma \right), \quad (3.62)$$

which is the same result as Eqs. (3.55) and (3.59). Therefore, we conclude that qualitatively new solutions cannot be constructed if we require a small \bar{B}_z , i.e., Eq. (3.45).

3.4.6 Oscillatory Axial Field Regime

We consider an *oscillatory axial field* \bar{B}_z , while maintaining a small \bar{p}'_y and $\delta \bar{B}_Q$, i.e., Eqs. (3.43), (3.46), and (3.47). In this regime, Eq. (3.38) can be rearranged as

$$\frac{\alpha_\lambda \bar{y}}{\beta} \left(\frac{4\bar{I}}{\bar{a}\bar{b}\beta\gamma^2} + \bar{\Phi}_{00}'' - \frac{\alpha_\lambda}{\gamma} \bar{B}_z^2 \right) = \frac{d\bar{p}_y}{d\bar{z}} - \alpha_\lambda \bar{y} \delta \bar{B}_Q + \frac{\alpha_\lambda \bar{B}_z}{\gamma\beta} \bar{p}_x^Q, \quad (3.63)$$

which implies

$$\frac{\alpha_\lambda \bar{y}}{\beta} \left(\frac{4\bar{I}}{\bar{a}\bar{b}\beta\gamma^2} + \bar{\Phi}_{00}'' - \frac{\alpha_\lambda}{\gamma} \bar{B}_z^2 \right) \sim \mathcal{O} \left(\frac{1}{\bar{S}_{\text{des}}^2} \left[2\bar{b}\gamma\beta + \frac{\bar{a}^2}{\bar{b}}\beta\gamma \right] \right). \quad (3.64)$$

Notice that in the coasting beam limit ($\bar{\Phi}_{00}'' \rightarrow 0$), Eq. (3.64) requires the current term on its left-hand side to be negated by the axial-field-squared term \bar{B}_z^2 , which is not possible. The axial field \bar{B}_z must have a zero-crossing, by Eq. (3.46), and therefore so must its square \bar{B}_z^2 , however the current term is nowhere vanishing. Therefore we conclude that $\bar{\Phi}_{00}''$ cannot be vanishing in this *oscillatory axial field* regime.

A novel solution is possible, however, if the axial potential $\bar{\Phi}_{00}''$ term is fixed to be oscillatory in such a way as to negate the oscillatory component of \bar{B}_z^2 , while the average value of \bar{B}_z^2 is chosen to negate the current term. This type of hybrid longitudinal magnetic-electrostatic focusing permits very precise control of beam evolution, however oscillatory electrostatic focusing introduces significant complexity for device geometry modeling and construction. For this reason, it is not discussed further in the present work, but remains as a subject for further exploration.

3.4.7 Small Residual Quadrupole Field Regime

The final simple ordering we will consider maintains a *small residual quadrupole field* $\delta \bar{B}_Q$, while allowing \bar{p}'_y and \bar{B}_z to oscillate, i.e., Eqs. (3.43), (3.46), and (3.48). In this regime, Eq. (3.38) can be rearranged as

$$\frac{d\bar{p}_y}{d\bar{z}} - \frac{\alpha_\lambda \bar{y}}{\beta} \left(\frac{4\bar{I}}{\bar{a}\bar{b}\beta\gamma^2} + \bar{\Phi}_{00}'' - \frac{\alpha_\lambda}{\gamma} \bar{B}_z^2 \right) = \alpha_\lambda \bar{y} \delta \bar{B}_Q - \frac{\alpha_\lambda \bar{B}_z}{\gamma\beta} \bar{p}_x^Q, \quad (3.65)$$

which implies

$$\frac{d\bar{p}_y}{d\bar{z}} - \frac{\alpha_\lambda \bar{y}}{\beta} \left(\frac{4\bar{I}}{\bar{a}\bar{b}\beta\gamma^2} + \bar{\Phi}_{00}'' - \frac{\alpha_\lambda}{\gamma} \bar{B}_z^2 \right) \sim \mathcal{O} \left(\frac{1}{\bar{S}_{\text{des}}^2} \left[\bar{b}\gamma\beta + \frac{\bar{a}^2}{\bar{b}}\beta\gamma \right] \right). \quad (3.66)$$

From Eq. (3.66), we find that a novel solution is possible even in the coasting beam limit ($\bar{\Phi}_{00}'' \rightarrow 0$). The oscillating momentum \bar{p}'_y can play the same role that the oscillating axial potential $\bar{\Phi}_{00}''$ did in Section 3.4.6, namely, the momentum \bar{p}'_y is

determined to be oscillatory in such a way as to negate the oscillatory component of \overline{B}_z^2 , while the average value of \overline{B}_z^2 is chosen to negate the current term. This type of oscillatory magnetic focusing will be further discussed in Chapter 5 as a solution for coasting elliptic beam transport. In Chapter 6, we also discuss the beam matching problem which occurs when the axial potential term in Eq. (3.66) is of the same order as the other terms on the left-hand side.

4 Elliptic Beam Formation

4.1 Overview

Although elliptic beams present numerous advantages, their inherent three-dimensional nature has made the design of elliptic beam-forming diodes a challenging process, both analytically and numerically. For the types of applications discussed in Chapter 1, and consistent with the assumptions introduced in Chapter 2, desirable beam diode characteristics include uniform current density and parallel, paraxial, laminar flow. These properties are consistent with the one-dimensional Child-Langmuir [29] solution, in which the electrostatic potential varies as $\Phi \propto z^{4/3}$, where z is the beam propagation distance.

In general, these Child-Langmuir flows are difficult to produce [30]. Recent studies of 2D and 3D [31] [32] [33] [34] [35] extensions of the Child-Langmuir law in an infinite applied magnetic field have shown that the beam exhibits significant current density enhancements near the beam-vacuum boundary. In the absence of an infinite confining magnetic field, the beam will tend to spread in phase-space, resulting in a degradation of beam quality. As shown by Pierce [36], it is possible to avoid these effects and to induce the space-charge flow in a higher-dimensional system to take the 1D Child-Langmuir flow form by calculating an equipotential geometry that is consistent with the 1D Child-Langmuir electric field within the beam and by constructing external electrodes lying along the equipotentials as prescribed that focus the beam. Such a beam can, in theory, exhibit extremely low emittance and laminar flow.

Pierce's approach [36] was to view diode design as an inverse problem – the beam plasma properties and electric field solution were known (they followed the Child-Langmuir form), but the boundary conditions (electrode geometry) were to be determined. His techniques, while valid for an infinite sheet (2D) beam, proved difficult to generalize to 3D. Advances in numerical computation since then have greatly aided the forward problem, but not the inverse problem. As a result, for the construction of physical beam diodes today, designers, guided by rough analytic results, make extensive use of ray-tracing software such as the 2D EGUN [37], the 3D OMNITRAK [38], and MICHELLE [39], and particle-in-cell software WARP [40]. In these codes, the boundary conditions are prescribed first, and then the solver computes the resulting beam profile. Since these powerful new tools are not directly applicable to the inverse problem, they must be used as part of a time-consuming iterative optimization process (i.e., guessing a

geometry, computing the beam, adjusting the geometry, and repeating the process) in order to arrive at an approximate set of external electrodes which support the desired beam profile. While such optimization problems may be tractable for 2D circular beams, with the added dimensionality of elliptical beams, they easily exceed computational limits.

In this chapter, a generalization of Pierce's technique is presented which permits direct analytic solution of the inverse diode design problem for elliptical Child-Langmuir beams. In addition to being useful for diode design in their own right, these analytic results can also be used in conjunction with numerical tools in order to speed the optimization process or to provide benchmarking comparisons. In order to clarify the treatment of the elliptic beam diode problem, we briefly discuss some important space-charge flow results in Section 4.2. We then present the elliptic diode design methodology in Section 4.3, followed by OMNITRAK [38] simulation results and tolerance studies in Section 4.4.

4.2 Review of Previous Space-Charge Flow Results

4.2.1 Relativistic Child-Langmuir Flow

We can quickly derive the relativistic formulation for elliptic beam Child-Langmuir flow by adopting the formalism of Chapter 3 and the ordering of Eq. (3.51). In this regime, we require

$$\frac{d^2\bar{\Phi}_{00}}{dz^2} = -\frac{4\bar{I}}{\bar{a}\bar{b}\beta\gamma^2}. \quad (4.1)$$

In order to connect our results most directly with the literature, we shall henceforth use the fully dimensional forms in this chapter. Using Eqs. (2.81), (2.84), and (2.87) to restore the full dimensionality of Eq. (4.1), and making use of $\gamma^{-2} = 1 - \beta^2$, we find

$$\bar{\Phi}_{00}'(z) = -\frac{4I}{abc\gamma\sqrt{\gamma^2 - 1}}, \quad (4.2)$$

where, in Eq. (4.2) and henceforth in this chapter, primes shall denote differentiation with respect to z . If we now make use of the paraxial approximation to write $\gamma = \gamma_{00}$ and employ Eq. (2.19), we find

$$\bar{\Phi}_{00}'' = -\frac{4I}{abc} \left[\left(\gamma_0 - \frac{q\Phi_{00}}{mc^2} \right) \sqrt{\left(\gamma_0 - \frac{q\Phi_{00}}{mc^2} \right)^2 - 1} \right]^{-1}. \quad (4.3)$$

Equation (4.3) is a nonlinear ordinary differential equation for the electrostatic potential that can be integrated numerically with appropriate boundary conditions, e.g., space-charge limited boundary conditions with $\Phi_{00}(0) = 0 = \Phi'_{00}(0)$. Once the potential is determined, the other beam properties in the paraxial approximation follow straightforwardly. Equation (4.3) is accurate within the paraxial approximation and relativistically correct, including the self-magnetic term neglected by Jory and Trivelpiece [41]. Nonetheless, it is unwieldy to work with because of the lack of an analytic solution.

Fortunately, Eq. (4.3) permits a closed-form solution in the nonrelativistic limit which is applicable to a wide variety of electron diodes and virtually all ion diodes. For the remainder of this work, we will focus on the nonrelativistic beam formation problem and defer solution of the fully relativistic elliptic beam Child-Langmuir flow equation (4.3) for future work. Moreover, since our concern is largely with space-charge limited diodes, we assume the initial beam velocity is vanishing, i.e. $\gamma_0 = 1$.

In the space-charge-limited ($\gamma_0 = 1$), nonrelativistic ($|q\Phi_{00}|/mc^2 \ll 1$) limit, we can Taylor expand Eq. (4.3), obtaining

$$\bar{\Phi}_{00}'' \cong -\frac{4I}{abc} \left(-2 \frac{q\Phi_{00}}{mc^2} \right)^{-1/2} \left(1 + \frac{5}{4} \frac{q\Phi_{00}}{mc^2} \right). \quad (4.4)$$

Multiplying both sides of Eq. (4.4) by Φ'_{00} , we obtain

$$\frac{1}{2} \frac{d}{dz} (\Phi'_{00})^2 \cong \frac{8I}{abcq} \left[\sqrt{\frac{mc^2}{2}} \frac{d}{dz} (-q\Phi_{00})^{1/2} - \frac{5}{12} \sqrt{\frac{1}{2mc^2}} \frac{d}{dz} (-q\Phi_{00})^{3/2} \right], \quad (4.5)$$

which can be integrated to yield

$$\frac{1}{2} (\Phi'_{00})^2 \cong \frac{8I}{abcq} \sqrt{\frac{mc^2}{2}} (-q\Phi_{00})^{1/2} \left[1 + \frac{5}{12} \frac{q\Phi_{00}}{mc^2} \right], \quad (4.6)$$

assuming the space-charge-limited boundary conditions

$$\Phi_{00}(0) = 0, \quad (4.7)$$

$$\Phi'_{00}(0) = 0. \quad (4.8)$$

To lowest order, we may express Eq. (4.6) as

$$\frac{1}{2}(\Phi'_{00})^2 \cong \frac{8I}{abq} \sqrt{\frac{m}{2}} (-q\Phi_{00})^{1/2}, \quad (4.9)$$

which is solved by

$$\Phi_{00} = -\frac{1}{q} \left(\frac{9Iq}{ab} \sqrt{\frac{m}{2}} \right)^{2/3} z^{4/3}, \quad (4.10)$$

or

$$\Phi_{00} = -\frac{1}{q} \left(9\pi Jq \sqrt{\frac{m}{2}} \right)^{2/3} z^{4/3}, \quad (4.11)$$

where the current density is $J = I/(\pi ab)$. Equation (4.11) is simply the nonrelativistic Child-Langmuir law, which will be derived in a more standard manner in Section 4.2.2. The second term in the brackets in Eq. (4.6) allows us to estimate the significance of any relativistic corrections to the nonrelativistic Child-Langmuir law, i.e., if $5q\Phi_{00}/12mc^2 \ll 1$, the nonrelativistic Child-Langmuir law is a good approximation.

4.2.2 Nonrelativistic Child-Langmuir Flow

We consider two infinite, parallel plates located at $z = 0$ and $z = d$ and held at fixed potentials $\Phi = 0$ and $\Phi = \Phi_d$, respectively. If the $z = 0$ plate is a charge emitter and the $z = d$ plate a charge absorber, a 1D laminar, space-charge-limited flow solution of the nonrelativistic Child-Langmuir [29] form is established by applying the nonrelativistic cold fluid equations:

$$\frac{\partial n}{\partial t} + \nabla \cdot (n\mathbf{v}) = 0, \quad (4.12)$$

$$\frac{\partial \mathbf{v}}{\partial t} + (\mathbf{v} \cdot \nabla)\mathbf{v} = -\frac{q}{m} \nabla \Phi, \quad (4.13)$$

$$\nabla^2 \Phi = -4\pi qn, \quad (4.14)$$

where m is the particle mass, q , the particle charge, n , the number density, and \mathbf{v} , the fluid velocity. By requiring a 1D steady-state solution, all quantities become functions of z alone. The continuity equation (4.12) implies constant current density $J\hat{\mathbf{e}}_z$, while the equation of motion (4.13) yields conservation of energy. Combining these with Poisson's equation (4.14) yields a differential equation for the electrostatic potential Φ :

$$\frac{\partial^2 \Phi}{\partial z^2} = -4\pi J \left(-\frac{2q}{m} \Phi \right)^{-1/2}. \quad (4.15)$$

Equation (4.15) is integrable, yielding the electrostatic potential

$$\Phi(z) = \Phi_d \left(\frac{z}{d} \right)^{4/3}, \quad (4.16)$$

the fluid velocity

$$\mathbf{v}(z) = \left(\frac{2q}{m} \Phi_d \right)^{1/2} \left(\frac{z}{d} \right)^{2/3} \hat{\mathbf{e}}_z, \quad (4.17)$$

the current density

$$J(z) = \frac{\sqrt{2}mc^3}{9\pi qd^2} \left(\frac{q\Phi_d}{mc^2} \right)^{3/2}, \quad (4.18)$$

and the number density

$$n(z) = \left(\frac{\Phi_d}{9\pi qd^2} \right) \left(\frac{z}{d} \right)^{-2/3}. \quad (4.19)$$

While this is a powerful and simple solution for a laminar flow, its infinite transverse extent makes it unphysical. Nonetheless, if the emitting and absorbing electrodes are sufficiently large, the central flow profile far (from the edges) will resemble the Child-Langmuir flow.

4.2.3 Pierce Sheet-Beam Diode

Pierce [72] noted that, while such an infinitely wide flow is not realizable, a portion of such a flow is, provided one used “electrodes outside of the beam shaped so that they would fool the electrons in the beam into thinking that they were part of a larger

planar, or cylindrical, or spherical flow." Mathematically, this is achieved by postulating a beam boundary and specifying boundary conditions there which are consistent with the Child-Langmuir (C-L) [29] solution. Since the particles in the beam interior are influenced only by local fields, the C-L boundary conditions on the beam edge are sufficient to enforce the C-L flow in the beam interior.

For example, the infinite beam solution becomes a semi-infinite one if a beam boundary exists along the $x = 0$ plane. Along this boundary, according to the C-L solution, the electric potential and its derivative are both specified, giving the following set of Cauchy boundary conditions:

$$\Phi(x = 0) = \Phi_d \left(\frac{z}{d} \right)^{4/3}, \quad (4.20)$$

$$\left. \frac{\partial \Phi}{\partial x} \right|_{x=0} = 0. \quad (4.21)$$

In the vacuum region outside the beam, the potential satisfies Laplace's equation, $\nabla^2 \Phi = 0$. While the *interior* beam problem is solved by C-L, Pierce's *exterior* problem requires solving Laplace's equation in the region outside the beam, subject to the boundary conditions (4.20) and (4.21) on the beam edge. Solutions to elliptic-equation Cauchy problems are difficult or impossible to obtain, and standard numerical methods fail due to the exponential growth of errors which is characteristic of such problems [42]. Pierce [36] saw a solution by inspection, however, writing

$$\begin{aligned} \Phi(z, x) &= \Phi_d \operatorname{Re} \left[\left(\frac{z + ix}{d} \right)^{4/3} \right] \\ &= \Phi_d \left(\frac{r}{d} \right)^{4/3} \cos \left(\frac{4\theta}{3} \right), \end{aligned} \quad (4.22)$$

where $z = r \cos \theta$ and $x = r \sin \theta$. Equation (4.22) for the potential is valid in the region $x \geq 0$ outside the beam, and electrodes placed along equipotentials of Eq. (4.22) will enforce the C-L flow on a semi-infinite charged particle stream. In Figure 4.1, we plot several equipotentials of Eq. (4.22) in the plane $(z - x)$ outside the beam. (The $x = 0$ surface corresponds to the beam edge.) Notice that the surface corresponding to $\Phi = 0$ is a straight line inclined at the Pierce angle of $\theta_p = 3\pi/8$ with respect to the beam edge.

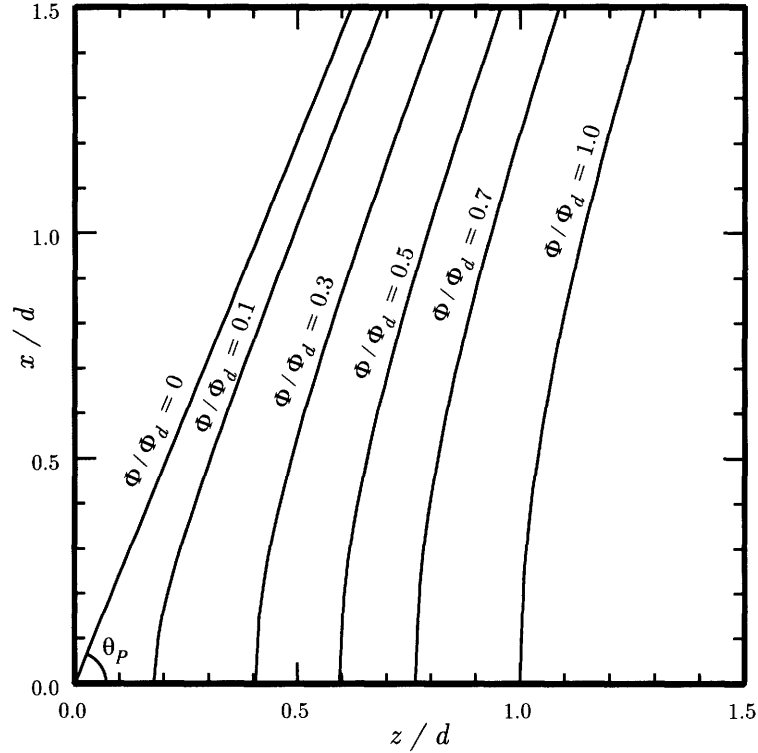


Figure 4.1: Several equipotentials of Eq. (4.22) are plotted in the plane $(z-x)$ outside the beam. The $x=0$ surface corresponds to the beam edge. Notice that the surface corresponding to $\Phi=0$ is a straight line inclined at the Pierce angle of $\theta_p = 3\pi/8$ with respect to the beam edge.

A similar operation can be performed to create another beam boundary (and corresponding set of electrodes) at some $x = x_b < 0$, which results in an infinitely wide sheet beam confined in the space $x_b < x < 0$. This 2D sheet beam, however, is unbounded in the y direction.

4.2.4 Radley Cylindrical Beam Diode

Radley [43] resolved the unboundedness problem by finding a solution for a circular beam of radius a . In the cylindrical coordinates (r, θ) , one can express the C-L boundary conditions for the circular beam as

$$\Phi|_{r=a} = \Phi_d \left(\frac{z}{d} \right)^{4/3}, \quad (4.23)$$

$$\left. \frac{\partial \Phi}{\partial r} \right|_{r=a} = 0, \quad (4.24)$$

for $r > a$. Note that $\partial \Phi / \partial \theta|_{r=a} = 0$ is also a boundary condition, but it is implied by Eq. (4.23).

A simple solution of the Pierce planar form does not hold in the cylindrical geometry, since the analog between Laplace's equation and the Cauchy-Riemann conditions for analytic functions only exists in the 2D Cartesian coordinates. Radley's method [43] employs a separation of variables technique and an expression of the potential as a complex contour integral of a sum of Bessel functions chosen to satisfy the boundary conditions at the beam edge. Rather than review this method in detail, we present the 3D generalization to the elliptic geometry in the following section and note where reductions to Radley's form can be made. Nakai [44], attempted to generalize Radley's technique to the 3D elliptic beam problem, but neglected the full functional dependence of the angular Mathieu functions, and as a result, arrived at a simple, but incorrect expression for the exterior potential.

4.3 Elliptical Diode Theory

4.3.1 Overview

We consider a nonrelativistic charged-particle beam of length d and elliptic cross-section with semi-major axis a and semi-minor axis b , as shown in Figure 4.2. The charged particles are emitted from a flat elliptic plate, held at potential $\Phi = 0$, in the $z = 0$ plane and collected by another flat elliptic plate, held at potential $\Phi = \Phi_d$, in the $z = d$ plane.

It is useful to introduce the elliptic cylindrical coordinate system (ξ, η, z) , i.e.,

$$x = f \cosh(\xi) \cos(\eta), \quad (4.25)$$

$$y = f \sinh(\xi) \sin(\eta), \quad (4.26)$$

where $0 \leq \xi < \infty$ is a radial coordinate, $0 \leq \eta < 2\pi$ is an angular coordinate, and $f = \sqrt{a^2 - b^2}$ is the distance from the center of the ellipse to either of its foci, as illustrated in Figure 4.2. The elliptic beam boundary is specified by the surface $\xi = \xi_0 = \coth^{-1}(a/b)$.

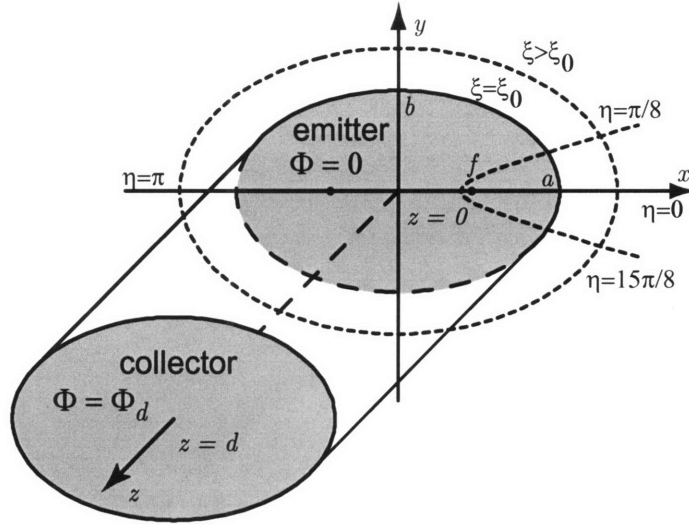


Figure 4.2: A beam of elliptic cross-section with semi-major axis a and semi-minor axis b is shown in the Cartesian and elliptic cylindrical coordinates. The beam is emitted from an elliptic plate at $\Phi = 0$ in the $z = 0$ plane and collected by an elliptic plate at $\Phi = \Phi_d$ in the $z = d$ plane. The beam fills the area enclosed by the surface $\zeta = \zeta_0$. In any z -plane, lines of constant ζ are ellipses, and lines of constant η are semi-hyperbolas.

To determine the potential distribution in the beam exterior, we solve Laplace's equation while matching the interior and exterior electric fields on the elliptic beam boundary. From the C-L solution, the matching conditions on the elliptic beam boundary imply [45], for $0 \leq z \leq d$,

$$\Phi|_{\zeta=\zeta_0} = \Phi_d \left(\frac{z}{d} \right)^{4/3}, \quad (4.27)$$

$$\frac{\partial \Phi}{\partial \zeta} \Big|_{\zeta=\zeta_0} = 0, \quad (4.28)$$

where the condition $\partial \Phi / \partial \eta|_{\zeta=\zeta_0} = 0$ is implied by Eq. (4.27).

We aim to find exterior equipotential surfaces corresponding to the emitter and collector potentials $\Phi = 0$ and $\Phi = \Phi_d$, respectively. If electrodes at the given potentials are made to lie along these surfaces, they will enforce the conditions in Eqs. (4.27) and (4.28) on the interval $0 \leq z \leq d$.

4.3.2 Mathieu Series Solution

In the elliptic cylindrical coordinates, Laplace's equation is expressed as

$$\frac{2}{f^2(\cosh 2\xi - \cos 2\eta)} \left(\frac{\partial^2 \Phi}{\partial \eta^2} + \frac{\partial^2 \Phi}{\partial \xi^2} \right) + \frac{\partial^2 \Phi}{\partial z^2} = 0. \quad (4.29)$$

We can write a product solution of the form $\Phi(\xi, \eta, z) = \Xi(\xi)\Theta(\eta)Z(z)$ and apply separation of variables to Eq. (4.29) to yield [45]

$$\frac{d^2 Z}{dz^2} - k^2 Z = 0, \quad (4.30)$$

$$\frac{d^2 \Theta}{d\eta^2} + \left(\tau - \frac{1}{2} k^2 f^2 \cos 2\eta \right) \Theta = 0, \quad (4.31)$$

$$\frac{d^2 \Xi}{d\xi^2} - \left(\tau - \frac{1}{2} k^2 f^2 \cosh 2\xi \right) \Xi = 0, \quad (4.32)$$

where k and τ are separation constants. Equation (4.30) leads simply to exponential solutions $Z = e^{kz}$.

Equation (4.31) is the angular Mathieu equation, but we are only interested in those angular Mathieu functions which have a periodicity of 2π and are even about $\eta = 0$ and $\eta = \pi/2$, since the boundary conditions in Eqs. (4.27) and (4.28) possess these same symmetries. Such solutions exist only for discrete eigenvalues of the separation constant τ , and we adopt the convention of Morse and Feshbach [46] to denote these angular Mathieu functions by $\Theta = \text{Se}_{2n}(kf, \eta)$ and the associated normalization constants $M_{2n}^e \equiv \int_0^{2\pi} [\text{Se}_{2n}(kf, u)]^2 du$, where n is a non-negative integer indexing the eigenvalues τ , as detailed in Ref. [46].

The corresponding solutions of Eq. (4.32), $\Xi = \text{Je}_{2n}(kf, \xi)$ and $\Xi = \text{Ne}_{2n}(kf, \xi)$ are radial Mathieu functions of the first and second kind, respectively.

We note that, in the Radley circular beam solution [43], there is no angular dependence. Consequently, Radley finds only two sets of relevant eigenfunctions: the exponentials and Bessel functions.

Any superposition of product solutions of the separated equations must satisfy Laplace's equation (4.29). Hence, we write [45]

$$\Phi(\xi, \eta, z) = \int_C dk A(k) e^{kz} G(kf, \xi, \eta), \quad (4.33)$$

where the transverse dependence is carried in

$$G(h, \xi, \eta) \equiv \sum_{n=0}^{\infty} \alpha_{2n}(h) \text{Se}_{2n}(h, \eta) [\text{Je}_{2n}(h, \xi) \text{Ne}'_{2n}(h, \xi_0) - \text{Ne}_{2n}(h, \xi) \text{Je}'_{2n}(h, \xi_0)], \quad (4.34)$$

we have chosen $\alpha_{2n}(h) \equiv [M_{2n}^c]^{-1} \int_0^{2\pi} \text{Se}_{2n}(h, u) du$, and the primes denote differentiation with respect to ξ . The integration contour C appearing in Eq. (4.33) is yet to be defined (see Figure 4.3). Note that the corresponding expression in Nakai [44] does not have $\text{Se}_{2n}(h, \eta)$ and omits the normalization factor α_{2n} .

The expansion in Eq. (4.33) assures that Φ satisfies Laplace's equation (4.29), and it is readily seen that the particular linear combination of radial Mathieu functions in Eq. (4.34) satisfies the boundary condition in Eq. (4.28). Moreover, using the Wronskian for the radial Mathieu functions and the orthogonality of the angular Mathieu functions, it can be shown that our definition of α_{2n} assures $G(h, \eta, \eta_0) = 1$, which assures that $\partial\Phi/\partial\eta|_{\xi=\xi_0} = 0$. Note that in the Radley circular beam solution [43], a superposition of the form of Eq. (16) is still used, but G takes the simple form

$$G(k, \rho) = ka \frac{\pi}{2} [J_1(ka) N_0(kr) - N_1(ka) J_0(kr)]. \quad (4.35)$$

Boundary condition (4.27) now implies

$$\Phi_d \left(\frac{z}{d} \right)^{4/3} = \int_C A(k) e^{kz} dk. \quad (4.36)$$

To invert this, we make use of the integral representation of the Gamma function Γ [47] to obtain

$$z^{4/3} = \frac{1}{\Gamma(-\frac{4}{3})} \frac{i}{2 \sin(\frac{4\pi}{3})} \int_C e^{kz} k^{-7/3} dk, \quad (4.37)$$

where the Hankel contour C is taken around the branch cut defined by the line $-\infty < \text{Re}(k) < 0$ on the $\text{Re}(k)$ axis, as shown in Figure 4.3.

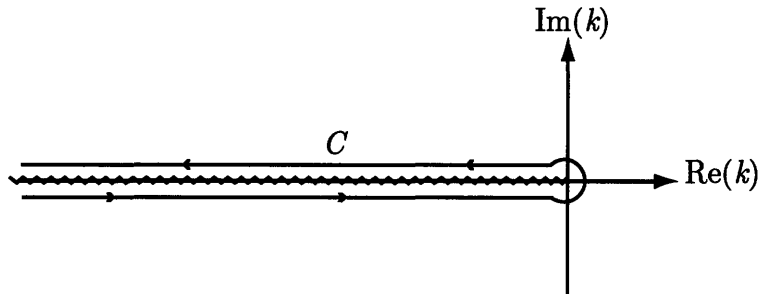


Figure 4.3: The Hankel contour C in the complex k plane is taken around the branch cut on the $\text{Re}(k)$ axis with $-\infty < \text{Re}(k) < 0$.

Equations (4.36) and (4.37) may be combined to yield

$$A(k) = \frac{\Phi_d d^{-4/3}}{\Gamma(-\frac{4}{3})} \frac{i}{2 \sin(\frac{4\pi}{3})} k^{-7/3}, \quad (4.38)$$

which completes the specification of the potential Φ in Eq. (4.33) with the Hankel contour of Figure 4.3 used for integration.

4.4 Numerical Results

4.4.1 Overview

Having derived an expression for the electrostatic potential external to the beam (the *exterior* problem), we proceed to compute the potential outside a 1D Child-Langmuir flow beam of arbitrary elliptic-cylindrical geometry. Generally, diode construction requires knowledge of the equipotentials corresponding to $\Phi = 0$ and $\Phi = \Phi_d$ electrodes, for which we apply a numeric root-finding scheme to the potential defined in Eq. (4.33). The Hankel contour integral is numerically evaluated employing standard techniques for the evaluation of the Mathieu functions [42] [48].

In order to verify the theory, the equipotential surfaces computed using this method are used as electrode boundaries in a 3D cold-beam space-charge-limited emission simulation using the commercially-available ray-tracing code OMNITRAK [38]. It is found that beams produced by such simulations exhibit essentially the parallel, laminar, uniform density Child-Langmuir flow.

Beam laminarity is often characterized by the 4 times rms emittances [49]

$$\varepsilon_x \equiv 4\sqrt{\langle x^2 \rangle \langle x'^2 \rangle - \langle xx' \rangle^2}, \quad (4.39)$$

$$\varepsilon_y \equiv 4\sqrt{\langle y^2 \rangle \langle y'^2 \rangle - \langle yy' \rangle^2}, \quad (4.40)$$

where the averages of transverse particle position (x, y) and divergence $(x', y') \equiv (dx/dz, dy/dz)$ are taken over a slice of the beam at $z = d$.

For a uniform density elliptic beam, the 4 times rms emittances can be related to the effective beam temperatures [50] by the relations

$$\varepsilon_x = a \sqrt{\frac{2kT_{\text{eff},x}}{q\Phi_d}}, \quad (4.41)$$

$$\varepsilon_y = b \sqrt{\frac{2kT_{\text{eff},y}}{q\Phi_d}}. \quad (4.42)$$

While thermal effects are generally not included in the simulations discussed in the present work, we point out that, in a physical system, the effective beam temperature cannot be reduced below the intrinsic temperature of the beam emitter which is about 1500 K. The effective temperature is an approximate measure of the beam temperature growth (beyond intrinsic) associated with non-ideal diode optics. In simulations, however, the effective temperature can also have a significant component generated by numerical noise. Uncorrelated emittances add quadratically, thus we expect the intrinsic emitter temperature to add linearly to the effective temperature predicted by a cold-beam simulation. Therefore, if a cold-beam simulation predicts an effective temperature well below the intrinsic value of 1500 K, we conclude that a physical beam will experience very little temperature growth as it is extracted from the emitter and accelerated through the diode, i.e., we have an ideal or near-ideal diode geometry.

Note that we use the effective beam temperature (rather than emittance) as a measure of beam quality in our discussion because it allows for a uniform comparison with the intrinsic limit imposed by the hot emitter across a wide range of beam parameters. The intrinsic (emitter-temperature-limited) emittance, on the other hand, is a function both of emitter size and diode voltage, and thus not as useful for comparisons between simulations of different beams.

In the following subsections, we consider a few specific diode geometries as examples.

4.4.2 10:1 Elliptic Electron Beam

In Figure 4.4, we depict the level curves of electrodes (a) $\Phi = 0$ and (b) $\Phi = \Phi_d$ for a 10:1 space-charge-limited elliptical electron diode with semi-major axis $a = 6.0$ mm, semi-minor axis $b = 0.6$ mm, and diode gap $d = 5.2$ mm, diode voltage $\Phi_d = 2.9$ kV, and current density $J = 1$ A/cm². Such a beam may have applications in high-efficiency microwave tubes, however for high-power or high-frequency applications where greater current density is desired, further beam compression will be required.

The level contours are roughly elliptical in shape, and the $\Phi = \Phi_d$ surface is more steeply inclined to the beam than the $\Phi = 0$ surface, as expected from the 2D Pierce theory [36]. It should be noted that these results differ significantly from those obtained using the method of Nakai [44]. For example, the $z/b = 3.3$ equipotential of Figure 4.4a intersects the x -axis at $x/b = 33.2$ and the y -axis at $y/b = 9.2$. The same $z/b = 3.3$ equipotential, computed using Nakai's expression, incorrectly gives an ellipse which intersects the axes at $x/b = 15.7$ and $y/b = 12.1$, respectively.

OMNITRAK [38] simulation results are shown in for Figure 4.5 for the same geometry as in Figure 4.4, using a variable-resolution computational mesh with x -spacing of 0.1 mm for $0 \leq x \leq 8$ mm and 0.5 mm for $8 \leq x \leq 15$ mm, y -spacing of 0.05 mm for $0 \leq y \leq 1$ mm, 0.1 mm for $1 \leq y \leq 5$ mm, and 0.4 mm for $5 \leq y \leq 12$ mm, and z -spacing of 0.05 mm for $0 \leq z \leq 0.8$ mm, 0.02 mm for $0.8 \leq z \leq 1.2$ mm, 0.05 mm for $1.2 \leq z \leq 2$ mm, 0.1 mm for $2 \leq z \leq 5.7$ mm, 0.05 mm for $5.7 \leq z \leq 7$ mm, and 0.1 mm for $7 \leq z \leq 10$ mm. The mesh resolution is higher in x and y across the cross-section of the beam, and in z where the beam intersects the emitter and collector. The 3D electrode structure was linearly interpolated between the equipotentials in Figure 4.4, each sampled at 46 points evenly distributed in η , for $0 \leq \eta \leq \pi/2$. Nearby computational nodes are shifted to conform to the electrode surfaces using the OMNITRAK *surface* flag. Neumann boundaries were used for the symmetry planes of the beam as well as for the outer boundaries of the simulation region, which is shown in Figure 4.5 along with computed equipotentials and particle trajectories projected to the planes $x = 0$ and $y = 0$. The entire simulation runs in approximately 30 minutes on a 3 GHz personal computer.

The beam produced by the simulation is essentially the parallel, laminar, uniform density Child-Langmuir flow, as verified by beam temperature measurements of $T_{\text{eff},x} = 6$ K and $T_{\text{eff},y} = 27$ K. Since the simulated temperatures are small compared to the intrinsic limit of 1500 K, we can infer that the emittance of an elliptical diode

constructed using the above prescription will approach the theoretical limits imposed by finite emitter temperature.

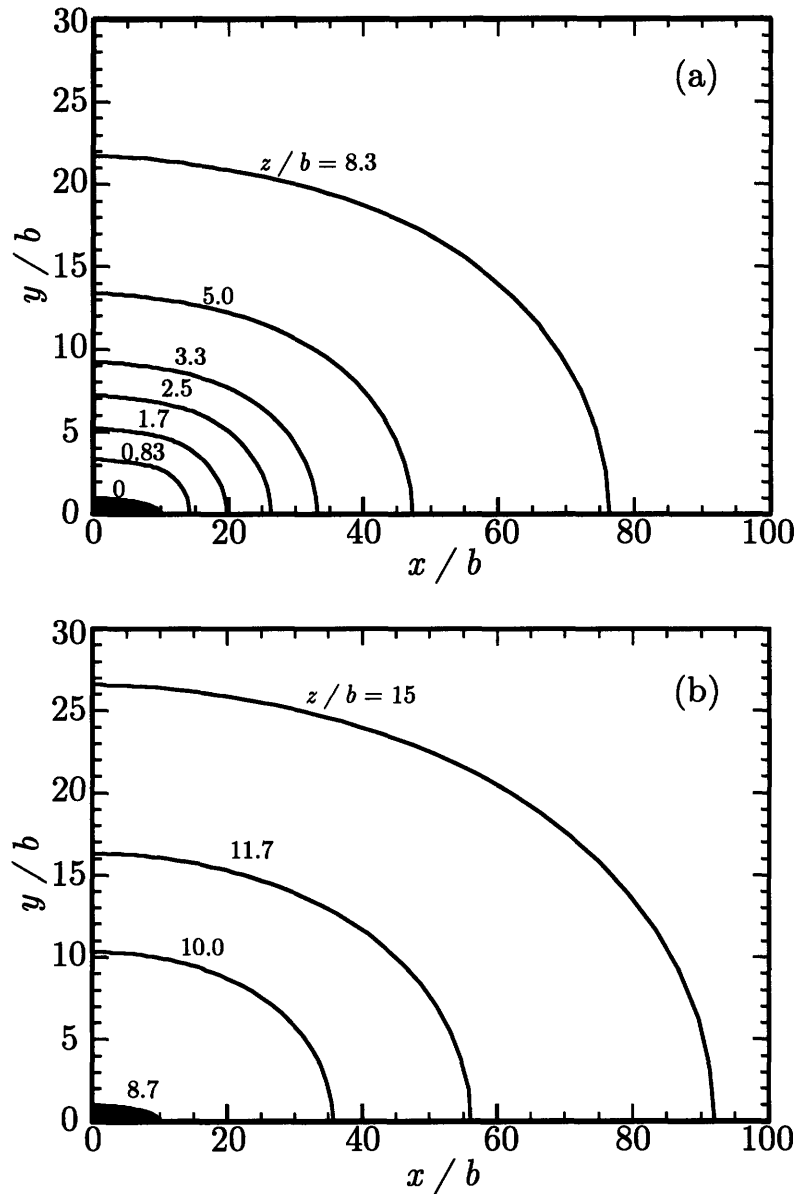


Figure 4.4: Level curves shown at various values of z for equipotential surfaces (a) $\Phi = 0$ and (b) $\Phi = \Phi_d$ of a 10:1 space-charge-limited elliptical electron diode with semi-major axis $a = 6.0$ mm, semi-minor axis $b = 0.6$ mm, and diode gap $d = 5.2$ mm.

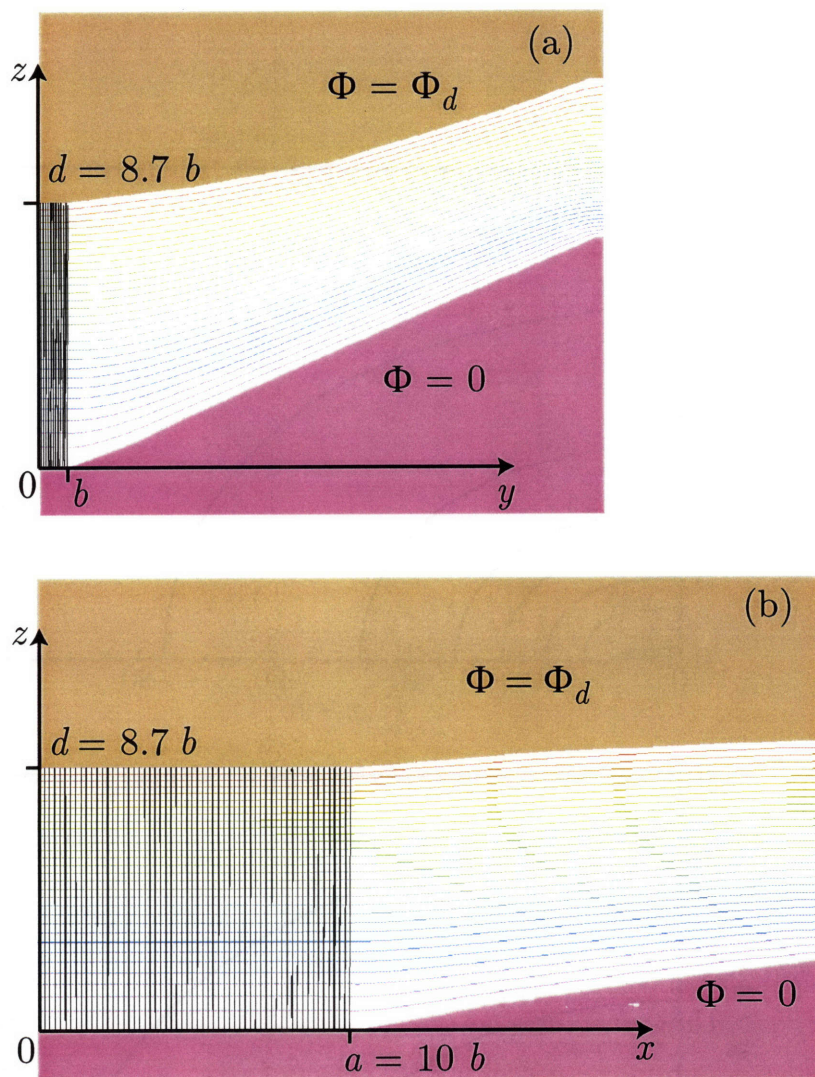


Figure 4.5: A 3D OMNITRAK simulation of a 10:1 space-charge-limited elliptical electron diode with semi-major axis $a = 6.0$ mm, semi-minor axis $b = 0.6$ mm, and diode gap $d = 5.2$ mm. Particle trajectories and equipotentials are shown in the planes corresponding to (a) $x = 0$ and (b) $y = 0$.

4.4.3 3:2 Elliptic Heavy Ion Beam

In Figure 4.6, we depict the level curves of electrodes (a) $\Phi = 0$ and (b) $\Phi = \Phi_d$ for a 3:2 space-charge-limited elliptical Na^+ diode with semi-major axis $a = 6$ cm, semi-minor axis $b = 4$ cm, diode gap $d = 33.5$ cm, diode voltage $\Phi_d = 1.0$ MV, and current density $J = 10$ mA/cm². Such a beam could find application in ion beam accelerators for high-energy density physics research.

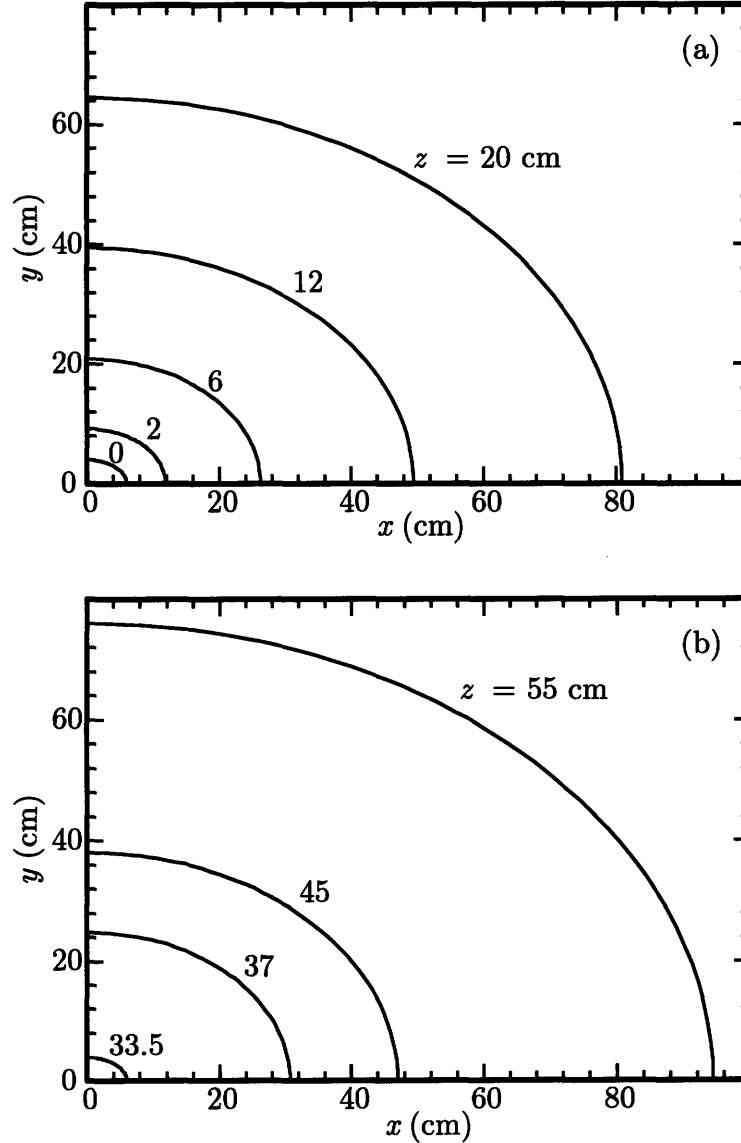


Figure 4.6: Level curves shown at various values of z for equipotential surfaces (a) $\Phi = 0$ and (b) $\Phi = \Phi_d$ of a 3:2 space-charge-limited elliptical Na^+ diode with semi-major axis $a = 6$ cm, semi-minor axis $b = 6$ cm, and diode gap $d = 33.5$ cm.

4.4.4 6:1 Electron Beam with Tolerance Studies

4.4.4.1 Simulation Overview

In Figure 4.7, we depict the level curves of electrodes (a) $\Phi = 0$ and (b) $\Phi = \Phi_d$ for a 6:1 space-charge-limited elliptical electron diode with semi-major axis $a = 3.73$ mm, semi-minor axis $b = 0.62$ mm, diode gap $d = 4.11$ mm, diode voltage $\Phi_d = 2290$ V, and current density $J = 1.5$ A/cm². Such a beam may have applications in high-efficiency microwave tubes. However, for high-power or high-frequency applications where greater current density is desired, further beam compression will be required.

As with the earlier example, the surfaces computed in Figure 4.7 are used as electrode boundaries in a 3D cold-beam space-charge-limited emission simulation using the commercially-available ray-tracing code OMNITRAK [38]. As shown in Figure 4.8, the beam produced by the simulation is essentially the parallel, laminar, uniform density Child-Langmuir flow. The OMNITRAK simulation predicts the effective beam temperatures $T_{\text{eff},x} = 17$ K and $T_{\text{eff},y} = 100$ K, which are well below the intrinsic thermal limit (1500 K), thus further reduction of the beam temperature in the simulation is not physically significant.

Whether a diode can approach the intrinsic thermal limit depends on its geometric design as well as its tolerance to perturbations and limitations of the sort likely to be encountered in a realistic device: finite extent, part misalignment, and allowances for thermal isolation. In the next several subsections, we examine each of these issues and also estimate the effect of a finite emitter temperature on the beam transport.

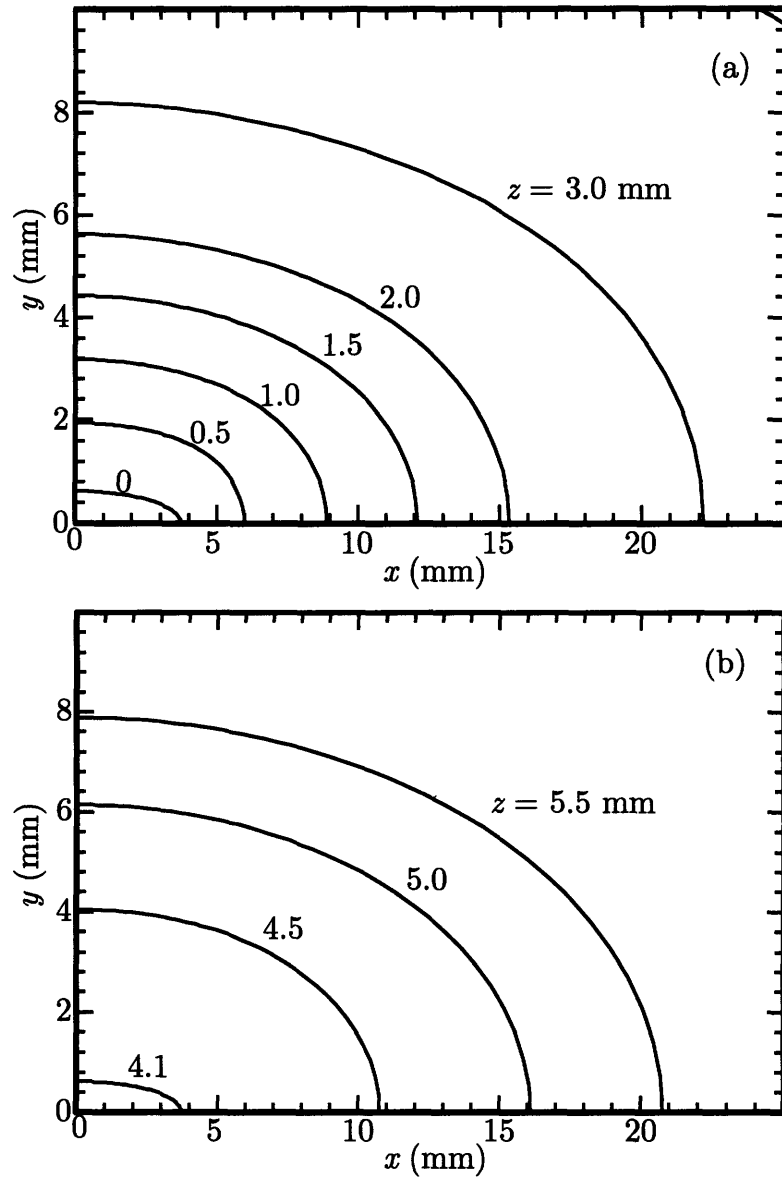


Figure 4.7: Level curves shown at various values of z for equipotential surfaces (a) $\Phi = 0$ and (b) $\Phi = \Phi_d$ of a 6:1 space-charge-limited elliptical electron diode with semi-major axis $a = 3.73$ mm, semi-minor axis $b = 0.62$ mm, and diode gap $d = 4.11$ mm.

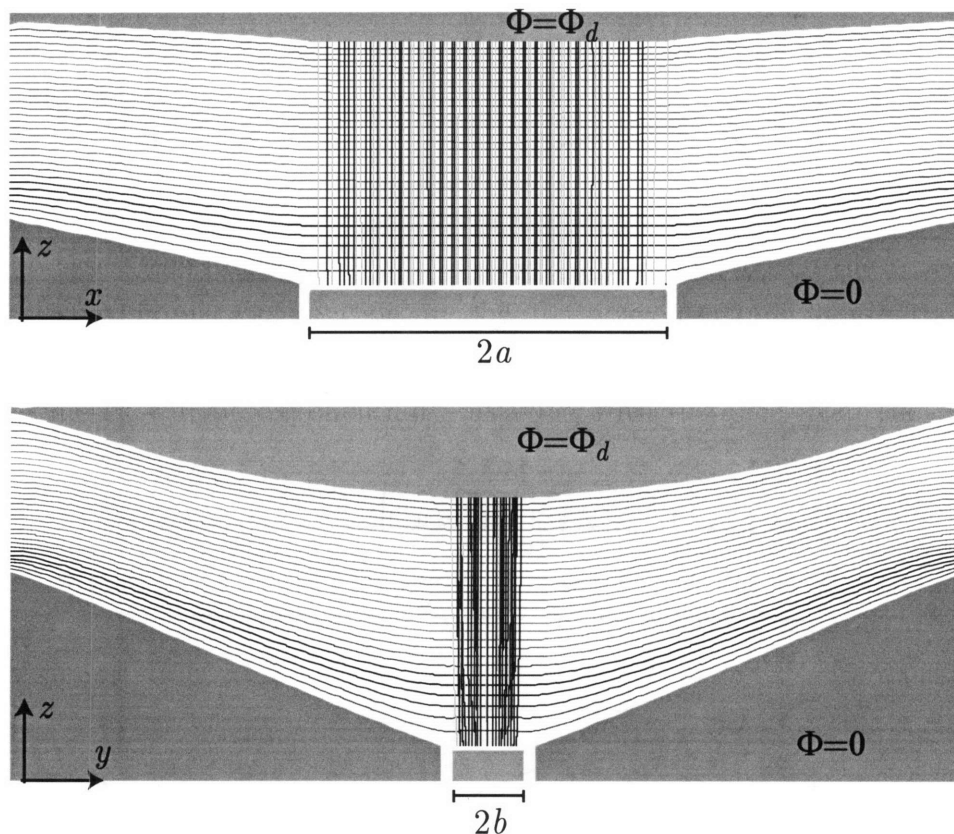


Figure 4.8: Results of an OMNITRAK simulation for a 6:1 elliptic electron beam diode with semi-major axis $a = 3.73$ mm, semi-minor axis $b = 0.62$ mm, diode gap $d = 4.11$ mm, and diode voltage $\Phi_d = 2290$ V. Particle trajectories are projected to the center planes $y = 0$ (above) and $x = 0$ (below) in the figure.

4.4.4.2 Sensitivity to Finite Extent of Electrodes

The theory of Ref. [45] computes equipotentials extending infinitely far from the beam. In practice, electrodes lying along these equipotentials will have a finite length, and it is important to assess the impact of the edge effects thus admitted on the beam. Since the potential satisfies Laplace's equation in the free-space region outside the beam, we expect that electrostatic potential variations caused by localized perturbations of the electrode geometry will be exponentially decaying with distance from the perturbation point.

We test this hypothesis by performing several cold-beam OMNITRAK simulations for the 6:1 electron diode example where the radial extent of the electrodes is varied and

the Neumann boundaries at the edge of the simulation region are kept fixed. The effective temperatures at the anode are shown as a function of electrode radius in Figure 4.9. The dashed line in Figure 4.9 indicates the intrinsic temperature 1500 K, and the figure clearly shows that the beam temperatures do not exceed intrinsic thermal levels unless the focusing electrodes are curtailed below a 6 mm radius.

We also notice that, because the effective temperatures do not reduce as the electrode radii are increased from 8 mm to 13 mm, these temperatures ($T_{\text{eff},x} = 17$ K and $T_{\text{eff},y} = 100$ K) effectively represent a noise floor for our simulation. Further reduction is not possible, given the limits imposed on particle number and mesh resolution by the finite computational memory.

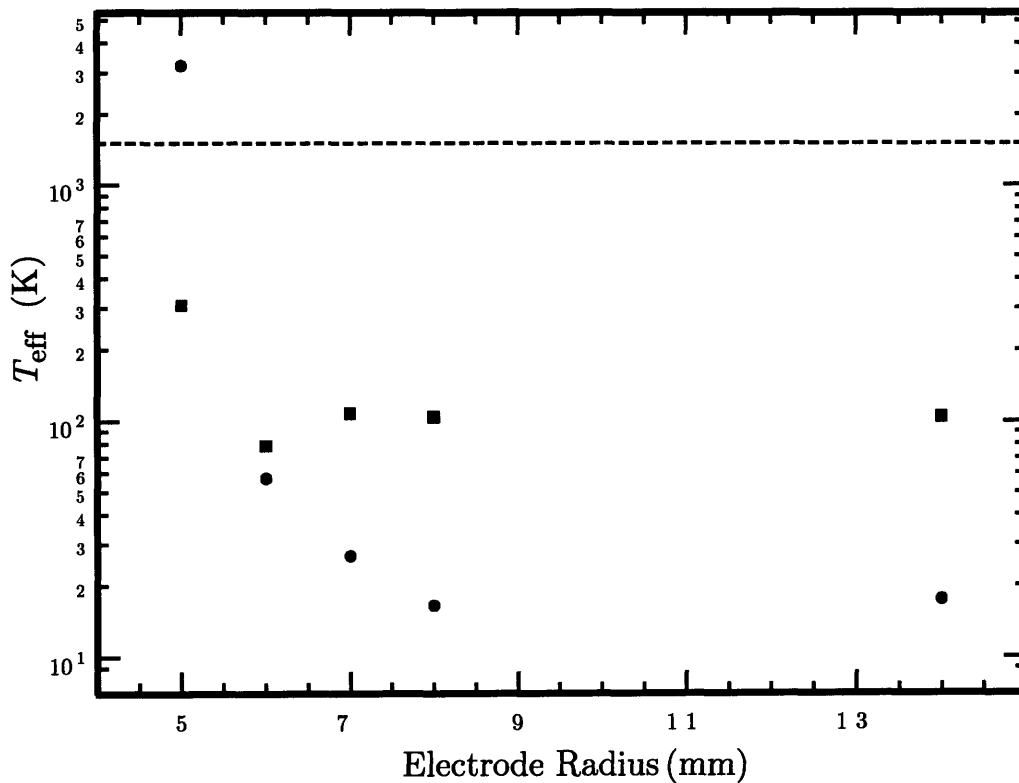


Figure 4.9: The effective beam temperature T_{eff} is plotted as the termination radius of the beam-focusing electrodes is varied. The circles indicate $T_{\text{eff},x}$, while the squares indicate $T_{\text{eff},y}$. The dashed line indicates the intrinsic temperature 1500 K.

4.4.4.3 Sensitivity to Part Misalignment

While the electrode extent study establishes the insensitivity of the beam quality to geometry perturbations far from the beam, we must allow for machining tolerances in the cutting and alignment of parts close to the beam as well. Several cold-beam OMNITRAK simulations were performed with small shifts in the emitter stalk position. Results for beam temperature variation with respect to transverse emitter stalk misalignments are shown in Figure 4.10, while results for beam temperature variation with respect to longitudinal emitter stalk misalignments are shown in Figure 4.11. The dashed lines in both figures indicate the intrinsic temperature 1500 K.

Particular sensitivity is observed with respect to transverse misalignments in Figure 4.10, however we believe that this effect is largely a numerical artifact resulting from the broken symmetry between the computation grid and model geometry when subject to transverse perturbations. Nonetheless, transverse emitter shifts of less than 0.04 mm can still be assured to yield a high-quality beam with an effective temperature near the intrinsic value of 1500 K.

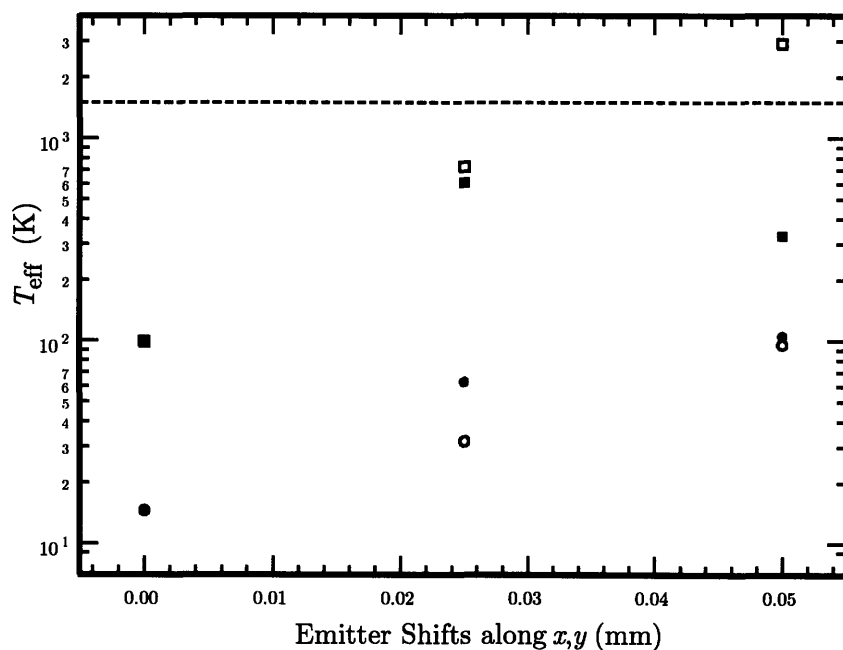


Figure 4.10: The effective beam temperature, T_{eff} is plotted as the emitter is shifted in the transverse plane ($x - y$). The circles indicate $T_{\text{eff},x}$, while the squares indicate $T_{\text{eff},y}$. The solid circles and squares represent shifts along x , while the open circles and squares represent shifts along y . The dashed line indicates the intrinsic temperature 1500 K.

The effective temperature is much less sensitive to symmetry-preserving longitudinal emitter shifts in the negative z -direction as seen in Figure 4.11. The positive z shifts lead to a greater effective temperature, largely because of enhanced edge emission. A slight depression of the emitter to a position near $z \cong -0.1$ mm ensures effective temperatures near the intrinsic limit for an alignment tolerance of $\Delta z = \pm 0.1$ mm.

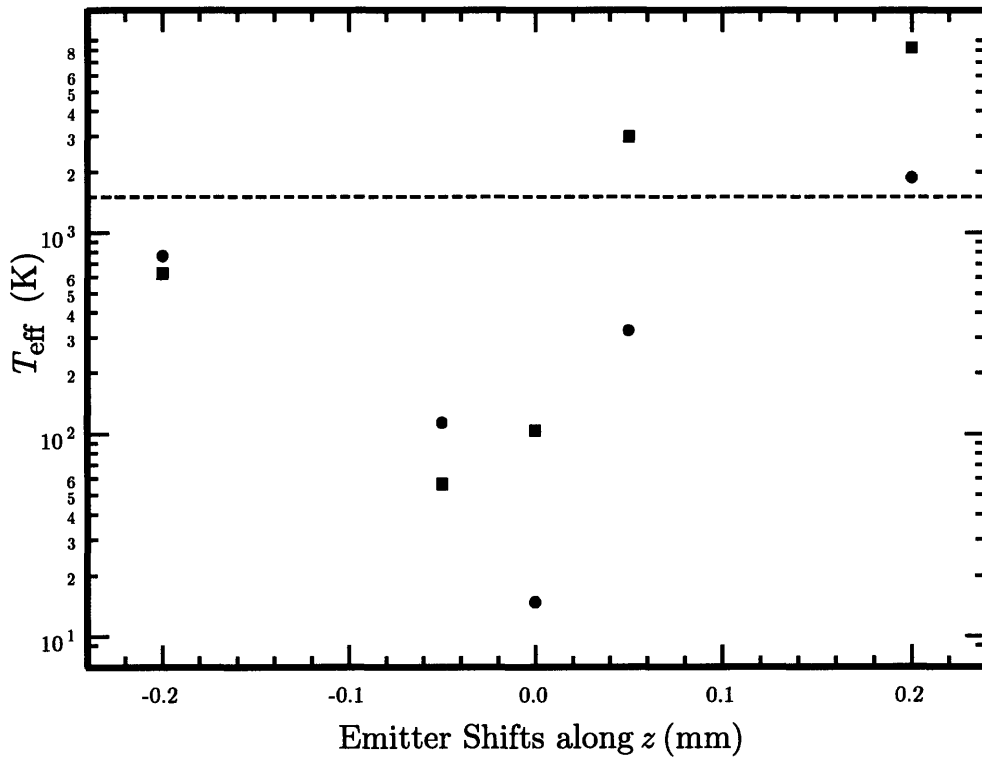


Figure 4.11: The effective beam temperature, T_{eff} is plotted as the emitter is shifted along the longitudinal coordinate z . The circles indicate $T_{\text{eff},x}$, while the squares indicate $T_{\text{eff},y}$. The dashed line indicates the intrinsic temperature 1500 K.

4.4.4.4 Sensitivity to Thermally-Insulating Gap

A hot thermionic emitter is often thermally isolated from the focus electrode by a vacuum gap. Several cold-beam OMNITRAK simulations were performed as we varied the elliptical gap width by a single parameter, δ_g , which represents the difference between the semi-major/minor radii of the inner edge of the focus electrode and the semi-major/minor radii of the emitter. The results, shown in Figure 4.12, generally indicate an effective temperature increasing with gap width, as expected. We note, however, that all the measure temperatures are below the intrinsic limit of 1500 K denoted by the dashed line in Figure 4.12. We conclude that the beam quality is insensitive to thermal gap widths of less than 0.25 mm.

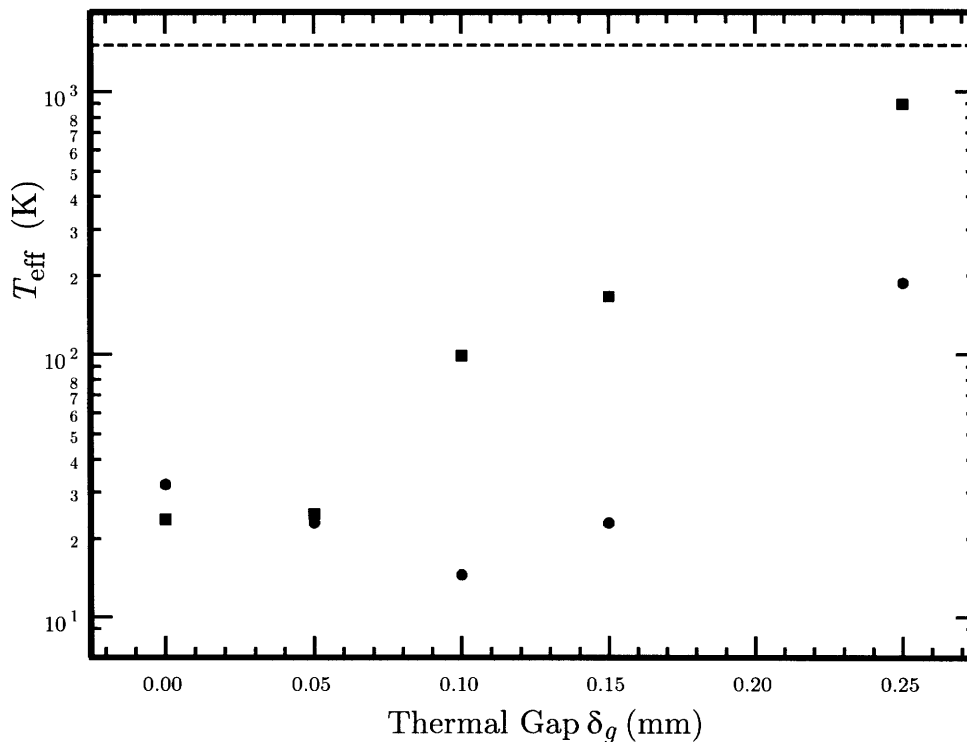


Figure 4.12: The effective beam temperature, T_{eff} is plotted as the vacuum gap thickness δ_g around the emitter is varied. The circles indicate $T_{\text{eff},x}$, while the squares indicate $T_{\text{eff},y}$. The dashed line indicates the intrinsic temperature 1500 K.

4.4.4.5 Warm Beam Simulations

While all the previous simulations have been performed using cold beams (zero initial thermal spread), we are able to assess the effect of a finite emitter temperature on the diode by artificially imposing an angular spread on the initial particle velocities using the OMNITRAK flag *dtheta*. Since the particles are emitted uniformly per unit solid angle up to an angle $\Delta\theta$ with respect to the surface normal, this yields a mean square divergence given by

$$\begin{aligned} \langle x'^2 \rangle &= \frac{\int_0^{\Delta\theta} d\theta \sin\theta \int_0^{2\pi} d\phi (\cos\phi \sin\theta)^2}{\int_0^{\Delta\theta} d\theta \sin\theta \int_0^{2\pi} d\phi} \\ &= \frac{1}{3} (2 + \cos\Delta\theta) \sin^2\left(\frac{\Delta\theta}{2}\right). \end{aligned} \quad (4.43)$$

Using Eq. (4.43) along with the defining relation of the rms emittance, Eq. (4.39), and its relation to temperature, Eq. (4.41), we are able to translate the initial angular spread to an effective emitter temperature T_0 , finding

$$T_0 = \frac{2q\Phi_d}{3k} (2 + \cos\Delta\theta) \sin^2\left(\frac{\Delta\theta}{2}\right). \quad (4.44)$$

We perform several OMNITRAK simulations and measure the effective temperature of the beam at the collector T_{eff} as a function of the effective emitter temperature T_0 . Results for several cases are shown in Figure 4.13. The dashed lines indicate the intrinsic temperature 1500 K. An ideal diode geometry simulation would have negligible temperature growth associated with beam optics or numerical noise, and thus it should produce effective temperatures that lie along the $T_{\text{eff}} = T_0$ line, indicated by the diagonal dotted line in Figure 4.13. We see that the noise floor of the simulation prevents the results from adhering to the $T_{\text{eff}} = T_0$ line for very low values of T_0 , but as T_0 approaches and exceeds the intrinsic temperature of 1500 K, temperature growth associated with diode geometry is negligible.

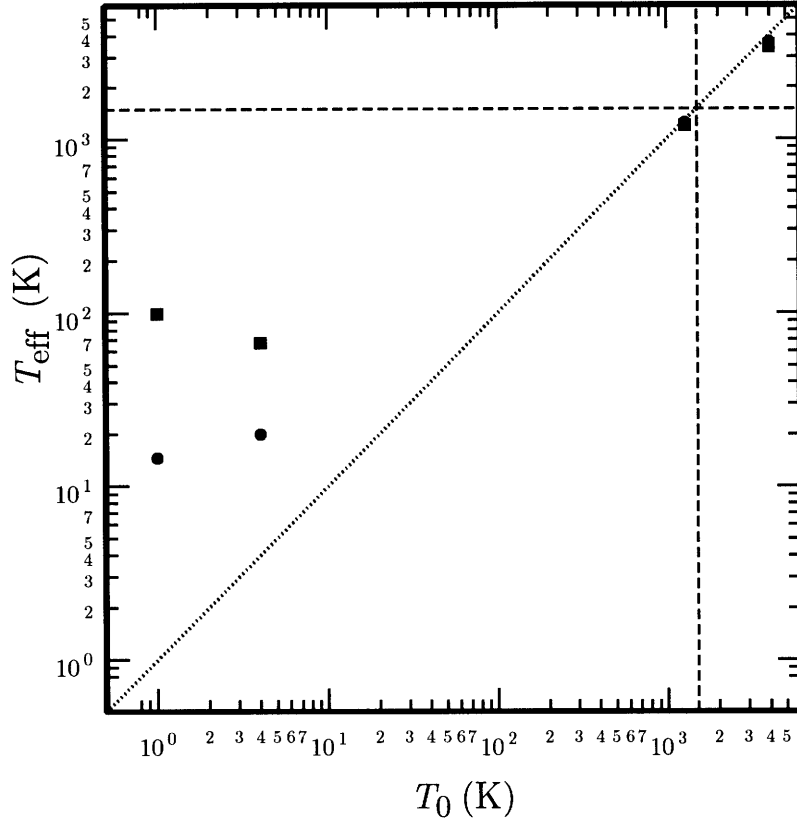


Figure 4.13: The effective beam temperature, T_{eff} is plotted as the effective emitter temperature T_0 is varied. The circles indicate $T_{\text{eff},x}$, while the squares indicate $T_{\text{eff},y}$. The dashed lines indicate the intrinsic temperature 1500 K. An ideal diode geometry simulation would produce temperatures along the $T_{\text{eff}} = T_0$ line, indicated by the diagonal dotted line.

4.5 Summary

We have obtained a novel relativistic generalization of paraxial, elliptic beam Child-Langmuir flow. In the nonrelativistic limit, we are able to define and analytically solve an inverse problem to determine the electrode geometries that support high-quality elliptic beam formation for use in vacuum electron devices and particle accelerators. 3D simulations have been performed which support the theory, and the sensitivity of the electrode specification theory to finite emitter temperature and to physical geometry and machining limitations such as finite extent, part misalignment, and allowances for mechanical and thermal stresses is studied. An achievable tolerance range is established for low-emittance, low effective-temperature beam generation.

5 Elliptic Beam Transport

5.1 Overview

Cost-effective, laminar transport (parallel focusing) of space-charge-dominated, large-aspect-ratio, elliptic beams is a long-standing problem that has stymied efforts to build devices that can make use of the geometric advantages of these beams. The conventional approaches to magnetic focusing for circular beams are not easily transferable to elliptic beams. Alternating-gradient quadrupole magnets have been used since the 1950s to focus charged-particle beams in particle accelerators (see Ref. [51] and references therein). In such focusing lattices, the beam semi-axes undergo large-amplitude oscillations, and as a result the beam envelope is, on average, circular – not elliptical, when the beam is space-charge-dominated. Uniform solenoidal magnets are often used to provide beam focusing in conventional microwave tubes [52], but their size and weight can be prohibitive. Moreover, for elliptical beams, the diocotron instability [23] [53] can cause the beam to disrupt in a solenoidal field. Circularly symmetric periodic solenoidal fields can be generated with permanent magnets that are smaller and more light-weight than uniformly solenoidal magnets and can provide comparable beam focusing for circular beams [52], however their azimuthally symmetric fields cannot balance the asymmetric space-charge forces of an elliptic beam, and the consequent beam twisting [16] and deformation is often not tolerable.

Alternative focusing methods have been developed for asymmetric beams. Periodic transverse (wiggler) magnetic focusing [21] [22] has been used for free-electron laser applications, but it can lead to excessive centroid motion for space-charge-dominated beams [14] [23] [24]. Promising results have been obtained through recent studies of period-averaged two-plane focusing in periodic permanent magnet (PPM) and quadrupole magnet configurations for space-charge-dominated [14] [15] [23] [53] [54] and emittance-dominated [14] [55] elliptic beams. Significant envelope oscillations and emittance growth are sometimes seen and may be rectified by a more thorough treatment which does not employ period-averaging and self-consistently includes the effect of beam twisting and evolving self-fields which are neglected in the two-plane approximation. Recent efforts in this vein [19] have led to a deeper understanding of space-charge-dominated elliptic beam propagation in a non-axisymmetric PPM field. Pure non-axisymmetric PPM focusing, however, is unsuited for sheet-like elliptic beams

with very large aspect-ratios as magnetic field nonlinearities in the wide tails of the beam become appreciable.

In this chapter, we develop a self-consistent solution for the focusing of coasting, sheet-like, space-charge-dominated elliptic beams using the most general formulation of centroid-preserving linear fields – a hybrid of non-axisymmetric PPM and quadrupole magnets and/or electrostatic quadrupoles suggested by the ordering in Eq. (3.66) when the axial potential $\bar{\Phi}_{00}$ is uniform. The desired elliptic beam profile has very nearly constant semi-axes, i.e.,

$$\bar{a} = \bar{a}_{\text{des}} + \delta\bar{a}, \quad (5.1)$$

$$\bar{b} = \bar{b}_{\text{des}} + \delta\bar{b}, \quad (5.2)$$

where \bar{a}_{des} and \bar{b}_{des} are the desired semi-major and semi-minor axes,

$$\delta\bar{a} \ll \bar{a}_{\text{des}}, \quad (5.3)$$

$$\delta\bar{b} \ll \bar{b}_{\text{des}}. \quad (5.4)$$

It also has a large aspect-ratio, i.e.,

$$\bar{b}_{\text{des}} \ll \bar{a}_{\text{des}}, \quad (5.5)$$

a small twist angle, i.e.,

$$\theta \ll 1, \quad (5.6)$$

and negligible velocity spread (emittance).

Note that we have set up the problem in a manner similar to Chapter 3, including use of the overbar notations to denote dimensionless variables and parameters. In this chapter, however, we concentrate on laminar beam dynamics rather than single particle dynamics. Because we address only parallel coasting beam transport in this chapter, unlike the more general approach of Chapter 3, the desired beam envelopes are assumed not just slowly-varying, but constant, i.e.,

$$\frac{d\bar{a}_{\text{des}}}{d\bar{z}} = 0 = \frac{d\bar{b}_{\text{des}}}{d\bar{z}}, \quad (5.7)$$

and the axial potential is constant, implying

$$\frac{d\bar{\Phi}_{00}}{d\bar{z}} = 0 = \frac{dy}{d\bar{z}} = 0 = \frac{d\beta}{d\bar{z}}. \quad (5.8)$$

We adopt the *small residual quadrupole field* regime of Section 3.4.7, which implies that the axial field \bar{B}_z (generated by the non-axisymmetric PPM magnets) should be oscillatory while satisfying Eq. (3.46). This condition can be satisfied by taking an oscillatory form for \bar{B}_z such as

$$\bar{B}_z(\bar{z}) = \bar{B}_0 \sin(\bar{k}\bar{z}), \quad (5.9)$$

where

$$\bar{k} \equiv \frac{2\pi}{\bar{S}}, \quad (5.10)$$

and provided that

$$\frac{\alpha_z}{\gamma\beta} \frac{\bar{b}}{\bar{a}} \pi \ll \frac{1}{\bar{S}}. \quad (5.11)$$

Equation (5.11) is implied when the parameter \bar{S} is regarded as an arbitrary dimensionless wavelength that allows the axial magnetic field profile to satisfy the constraint equation (3.46) for the *small residual quadrupole field* regime. Later, in Section 5.6, we will derive additional constraints on \bar{S} .

We also assume (pursuant to the discussion in Section 3.2.2) that the aspect ratio parameter of the magnetic field is constant and small, i.e.,

$$|r_m| \ll 1. \quad (5.12)$$

Equation (2.104) for the particle distribution evolution can be integrated if the starting values for the elements of the distribution matrix $\underline{\underline{\mathbf{M}}}$ and the applied fields are known. We have shown, in Section 2.6.4, how knowledge of the envelope quantities implies knowledge of the distribution matrix elements, and so in this chapter we concentrate on finding a self-consistent set of envelope quantities and applied fields that support the desired elliptic beam. We begin in Section 5.2 by relating particle trajectory perturbations to beam envelope perturbations. In Section 5.3, the trajectory perturbations and envelope twist angle θ are determined in terms of the desired elliptic beam envelope parameters. A similar procedure yields the residual quadrupole magnetic field $\delta\bar{B}_Q$ in Section 5.4, the longitudinal magnetic field strength \bar{B}_0 in Section 5.4.3,

and the envelope semi-axis perturbations $\delta\bar{a}$ and $\delta\bar{b}$ in Section 5.5. A number of ordering constraints which arise in the analysis are discussed in Section 5.6. With these results, we have sufficient information to integrate Equation (2.104) for the evolution of the particle distribution, and some numerical examples are explored in Section 5.7.

5.2 Envelope Perturbations

Particle trajectories in the desired elliptic beam can be written using Eq. (3.1) as

$$(\bar{x}, \bar{y}) = (\bar{x}_{\text{des}}, \bar{y}_{\text{des}}) + (\delta\bar{x}, \delta\bar{y}), \quad (5.13)$$

where we assume the desired trajectories are constant, i.e.,

$$\frac{d\bar{x}_{\text{des}}}{d\bar{z}} = \frac{d\bar{y}_{\text{des}}}{d\bar{z}} = 0, \quad (5.14)$$

and the perturbations are small

$$\delta\bar{x} \ll \bar{x}_{\text{des}}, \quad (5.15)$$

$$\delta\bar{y} \ll \bar{y}_{\text{des}}. \quad (5.16)$$

Since we are neglecting velocity spread, all beam quantities are functions of position only, thus the particle trajectory perturbations can be further expanded as

$$\delta\bar{x} = \bar{x}\delta\bar{x}_x + \bar{y}\delta\bar{x}_y, \quad (5.17)$$

$$\delta\bar{y} = \bar{x}\delta\bar{y}_x + \bar{y}\delta\bar{y}_y. \quad (5.18)$$

These particle trajectory perturbations can be related to the envelope perturbations $\delta\bar{a}$, $\delta\bar{b}$, θ by considering the equation for the bounding ellipse of the desired particle distribution in the phase space (\bar{x}, \bar{y}) , i.e., by analogy to Eq. (2.109),

$$1 = \frac{\bar{x}_{\text{des}}^2}{\bar{a}_{\text{des}}^2} + \frac{\bar{y}_{\text{des}}^2}{\bar{b}_{\text{des}}^2}. \quad (5.19)$$

Note that the desired twist angle is $\theta = 0$, hence the simple form for Eq. (5.19).

Substituting Eqs. (5.13), (5.17), and (5.18) into Eq. (5.19) and collecting terms, we find

$$\begin{aligned}
1 = \bar{x}^2 \left(\frac{1 - 2\delta\bar{x}_x + \delta\bar{x}_x^2}{\bar{a}_{\text{des}}^2} + \frac{\delta\bar{y}_x^2}{\bar{b}_{\text{des}}^2} \right) - 2\bar{x}\bar{y} \left(\frac{\delta\bar{x}_y - \delta\bar{x}_x\delta\bar{x}_y}{\bar{a}_{\text{des}}^2} + \frac{\delta\bar{y}_x - \delta\bar{y}_x\delta\bar{y}_y}{\bar{b}_{\text{des}}^2} \right) \\
+ \bar{y}^2 \left(\frac{1 - 2\delta\bar{y}_y + \delta\bar{y}_y^2}{\bar{b}_{\text{des}}^2} + \frac{\delta\bar{x}_y^2}{\bar{a}_{\text{des}}^2} \right),
\end{aligned} \tag{5.20}$$

which can be compared with the matrix form of the equation for the ellipse (2.108) to yield

$$M_{\bar{x}\bar{x}} = \frac{\bar{b}_{\text{des}}^2 \delta\bar{x}_y^2 + \bar{a}_{\text{des}}^2 (1 - \delta\bar{y}_y)^2}{(1 - \delta\bar{x}_x - \delta\bar{x}_y\delta\bar{y}_x - \delta\bar{y}_y + \delta\bar{x}_x\delta\bar{y}_y)^2}, \tag{5.21}$$

$$M_{\bar{x}\bar{y}} = \frac{\bar{b}_{\text{des}}^2 (\delta\bar{x}_y - \delta\bar{x}_x\delta\bar{x}_y) - \bar{a}_{\text{des}}^2 (\delta\bar{y}_x - \delta\bar{y}_x\delta\bar{y}_y)}{(1 - \delta\bar{x}_x - \delta\bar{x}_y\delta\bar{y}_x - \delta\bar{y}_y + \delta\bar{x}_x\delta\bar{y}_y)^2}, \tag{5.22}$$

$$M_{\bar{y}\bar{y}} = \frac{\bar{a}_{\text{des}}^2 \delta\bar{y}_x^2 + \bar{b}_{\text{des}}^2 (1 - \delta\bar{x}_x)^2}{(1 - \delta\bar{x}_x - \delta\bar{x}_y\delta\bar{y}_x - \delta\bar{y}_y + \delta\bar{x}_x\delta\bar{y}_y)^2}. \tag{5.23}$$

We use Eqs. (5.21), (5.22), and (5.23) to find the envelope parameters \bar{a} , \bar{b} , and θ through Eqs. (2.119), (2.120), and (2.121). After some simplification, this allows us to express the envelope perturbations, to lowest order in each of the trajectory perturbations, as

$$\delta\bar{a} = \bar{a}_{\text{des}} \left(\delta\bar{x}_x + \frac{1}{2} \frac{\bar{b}_{\text{des}}^2 \delta\bar{x}_y^2 + \bar{a}_{\text{des}}^2 \delta\bar{y}_x^2 + 2\bar{a}_{\text{des}}^2 \delta\bar{x}_y\delta\bar{y}_x}{\bar{a}_{\text{des}}^2 - \bar{b}_{\text{des}}^2} \right), \tag{5.24}$$

$$\delta\bar{b} = \bar{b}_{\text{des}} \left(\delta\bar{y}_y - \frac{1}{2} \frac{\bar{b}_{\text{des}}^2 \delta\bar{x}_y^2 + \bar{a}_{\text{des}}^2 \delta\bar{y}_x^2 + 2\bar{b}_{\text{des}}^2 \delta\bar{x}_y\delta\bar{y}_x}{\bar{a}_{\text{des}}^2 - \bar{b}_{\text{des}}^2} \right), \tag{5.25}$$

$$\theta = \frac{\bar{a}_{\text{des}}^2 \delta\bar{y}_x + \bar{b}_{\text{des}}^2 \delta\bar{x}_y}{\bar{a}_{\text{des}}^2 - \bar{b}_{\text{des}}^2}. \tag{5.26}$$

5.3 Trajectory Perturbations and Envelope Twist Angle

5.3.1 Wide-Dimension Trajectory Perturbations

An easy path to determining the wide-dimension trajectory perturbations $\delta\bar{x}_x$ and $\delta\bar{x}_y$ is suggested by the results of Section 3.2, in particular, Eqs. (3.14), (3.18), (3.21), and (3.22). We make the identifications

$$\delta\bar{x}^Q = \bar{x}\delta\bar{x}_x, \quad (5.27)$$

$$\delta\bar{x}^z = \bar{y}\delta\bar{x}_y. \quad (5.28)$$

Substituting Eq. (5.27) into Eq. (3.21) and making use of Eq. (3.18), we find

$$\frac{d^2\delta\bar{x}_x}{d\bar{z}^2} \cong -\frac{\alpha_\lambda}{\gamma\beta}\delta\bar{B}_Q, \quad (5.29)$$

where we used the fact that $\gamma\beta$ and $\bar{x} \cong \bar{x}_{\text{des}}$ are nearly constant. Because the residual quadrupole field $\delta\bar{B}_Q$ has not been determined, we will return to solve Eq. (5.29) in Section 5.5.

Substituting Eq. (5.28) into Eq. (3.22) and using Eq. (3.14), we find

$$\frac{d\delta\bar{x}_y}{d\bar{z}} \cong \frac{\alpha_\lambda\bar{B}_z}{\gamma\beta}(1-r_m) + \frac{1}{\bar{y}\gamma\beta}\left\{\bar{p}_x^z(\bar{z}_0) - \alpha_\lambda\bar{y}(\bar{z}_0)\bar{B}_z(\bar{z}_0)[1-r_m(\bar{z}_0)]\right\}. \quad (5.30)$$

We substitute Eq. (5.9) into Eq. (5.30), set $\bar{z}_0 = 0$, and specify the initial condition $\bar{p}_x^z(0) = 0$ to obtain

$$\frac{d\delta\bar{x}_y}{d\bar{z}} \cong \frac{\alpha_\lambda\bar{B}_0}{\gamma\beta}(1-r_m)\sin(\bar{k}\bar{z}), \quad (5.31)$$

and the solution

$$\delta\bar{x}_y \cong \bar{X}_y - \frac{\alpha_\lambda\bar{B}_0}{\bar{k}\gamma\beta}(1-r_m)\cos(\bar{k}\bar{z}), \quad (5.32)$$

where the additive constant \bar{X}_y appears due to the integration that resulted in Eq. (5.32) and is determined by the initial conditions. Since we seek solutions which minimize trajectory and envelope perturbations, we require $\bar{X}_y = 0$, yielding

$$\delta \bar{x}_y \cong -\frac{\alpha_\lambda \bar{B}_0}{\bar{k} \gamma \beta} (1 - r_m) \cos(\bar{k} \bar{z}). \quad (5.33)$$

Equation (5.33) will be used in Sections 5.3.2 and 5.3.3.

5.3.2 Narrow-Dimension Trajectory Perturbations

We find the narrow-dimension trajectory perturbations in a process analogous to that for the wide-dimension perturbations in Section 5.3.1. Let us consider the equation of motion in the short dimension (3.32), which can be expressed as

$$\begin{aligned} \frac{d\bar{p}_y}{d\bar{z}} = & \frac{\alpha_\lambda \bar{y}}{\beta} \left(\frac{4\bar{I}}{\bar{a}\bar{b}\beta\gamma^2} + \beta\delta\bar{B}_Q \right) - \frac{\alpha_\lambda \bar{B}_z}{\gamma\beta} \left[\alpha_\lambda \bar{y} \bar{B}_z (1 - r_m) + \bar{p}_x^Q \right] \\ & + \frac{\alpha_\lambda \bar{x}}{\beta} \left(-\bar{\Phi}_{11} + \beta^2 \bar{\Phi}_{11}^{\rho 0} - r_m \beta \frac{d\bar{B}_z}{d\bar{z}} \right). \end{aligned} \quad (5.34)$$

Rearranging terms in Eq. (5.34) and using Eqs. (3.21) and (5.27) to rewrite \bar{p}_x^Q , we find

$$\begin{aligned} \frac{d\bar{p}_y}{d\bar{z}} = & \frac{\alpha_\lambda \bar{y}}{\beta} \left(\frac{4\bar{I}}{\bar{a}\bar{b}\beta\gamma^2} - \frac{\alpha_\lambda}{\gamma} \bar{B}_z^2 (1 - r_m) + \beta\delta\bar{B}_Q \right) \\ & + \frac{\alpha_\lambda \bar{x}}{\beta} \left(-\bar{\Phi}_{11} + \beta^2 \bar{\Phi}_{11}^{\rho 0} - r_m \beta \frac{d\bar{B}_z}{d\bar{z}} - \beta \bar{B}_z \frac{d\delta\bar{x}_x}{d\bar{z}} \right), \end{aligned} \quad (5.35)$$

which we simplify using Eqs. (2.5), (2.34) for the electrostatic terms, and the small angle approximation $\theta \ll 1$, to yield

$$\begin{aligned} \frac{d\bar{p}_y}{d\bar{z}} = & \frac{\alpha_\lambda \bar{y}}{\beta} \left(\frac{4\bar{I}}{\bar{a}\bar{b}\beta\gamma^2} - \frac{\alpha_\lambda}{\gamma} \bar{B}_z^2 (1 - r_m) + \beta\delta\bar{B}_Q \right) \\ & + \frac{\alpha_\lambda \bar{x}}{\beta} \left(-\frac{4\bar{I}\theta(\bar{a} - \bar{b})}{\bar{a}\bar{b}(\bar{a} + \bar{b})\beta\gamma^2} - \bar{\Phi}_Q \tan 2\theta_Q - r_m \beta \frac{d\bar{B}_z}{d\bar{z}} - \beta \bar{B}_z \frac{d\delta\bar{x}_x}{d\bar{z}} \right), \end{aligned} \quad (5.36)$$

where use has been made of $\bar{\Phi}_{11}^\rho = \bar{\Phi}_{11}^{\rho 0}$, since the beam is not accelerating.

By analogy to the procedure of Section 3.2.1, Eq. (5.36) motivates us to write

$$\frac{d\bar{p}_y}{d\bar{z}} = \gamma\beta \left(\bar{x} \frac{d^2 \delta \bar{y}_x}{d\bar{z}^2} + \bar{y} \frac{d^2 \delta \bar{y}_y}{d\bar{z}^2} \right), \quad (5.37)$$

where

$$\frac{d^2\delta\bar{y}_x}{d\bar{z}^2} = -\frac{\alpha_\lambda}{\gamma\beta} \left(\frac{4\bar{I}\theta(\bar{a} - \bar{b})}{\bar{a}\bar{b}(\bar{a} + \bar{b})\beta^2\gamma^2} + \frac{\bar{\Phi}_Q}{\beta} \tan 2\theta_Q + r_m \frac{d\bar{B}_z}{d\bar{z}} + \bar{B}_z \frac{d\delta\bar{x}_x}{d\bar{z}} \right), \quad (5.38)$$

and

$$\frac{d^2\delta\bar{y}_y}{d\bar{z}^2} = \frac{\alpha_\lambda}{\gamma\beta} \left(\frac{4\bar{I}}{\bar{a}\bar{b}\beta^2\gamma^2} - \frac{\alpha_\lambda\bar{B}_z^2}{\beta\gamma} (1 - r_m) + \delta\bar{B}_Q \right). \quad (5.39)$$

To first order in the perturbed envelope quantities, Eqs. (5.38) and (5.39) become

$$\frac{d^2\delta\bar{y}_x}{d\bar{z}^2} \cong -\frac{\alpha_\lambda}{\gamma\beta} \left[\frac{4\bar{I}\theta(\bar{a}_{\text{des}} - \bar{b}_{\text{des}})}{\bar{a}_{\text{des}}\bar{b}_{\text{des}}(\bar{a}_{\text{des}} + \bar{b}_{\text{des}})\beta^2\gamma^2} + \frac{\bar{\Phi}_Q \tan 2\theta_Q}{\beta} + \bar{k}r_m\bar{B}_0 \cos(\bar{k}\bar{z}) + \bar{B}_z \frac{d\delta\bar{x}_x}{d\bar{z}} \right], \quad (5.40)$$

and

$$\frac{d^2\delta\bar{y}_y}{d\bar{z}^2} = \frac{\alpha_\lambda}{\gamma\beta} \left\{ \frac{4\bar{I}}{\bar{a}_{\text{des}}\bar{b}_{\text{des}}\beta^2\gamma^2} \left(1 - \frac{\delta\bar{a}}{\bar{a}_{\text{des}}} - \frac{\delta\bar{b}}{\bar{b}_{\text{des}}} \right) - \frac{\alpha_\lambda\bar{B}_0^2}{2\beta\gamma} (1 - r_m) [1 - \cos(2\bar{k}\bar{z})] + \delta\bar{B}_Q \right\}, \quad (5.41)$$

where we have made use of Eq. (5.9) for the axial magnetic field \bar{B}_z .

Because the residual quadrupole field $\delta\bar{B}_Q$ is still unknown, we will return to solve Eq. (5.41) in Section 5.5. Proceeding with Eq. (5.40), we make use of Eq. (5.26) for θ , obtaining

$$\begin{aligned} \frac{d^2\delta\bar{y}_x}{d\bar{z}^2} \cong & -\frac{\alpha_\lambda}{\gamma\beta} \left\{ \frac{4\bar{I}(\bar{a}_{\text{des}}^2\delta\bar{y}_x + \bar{b}_{\text{des}}^2\delta\bar{x}_y)}{\bar{a}_{\text{des}}\bar{b}_{\text{des}}(\bar{a}_{\text{des}} + \bar{b}_{\text{des}})^2\beta^2\gamma^2} + \frac{\bar{\Phi}_Q \tan 2\theta_Q}{\beta} \right. \\ & \left. + \bar{B}_0 \left[kr_m \cos(\bar{k}\bar{z}) + \frac{d\delta\bar{x}_x}{d\bar{z}} \sin(\bar{k}\bar{z}) \right] \right\}. \end{aligned} \quad (5.42)$$

After some simplification, we can express Eq. (5.42) using Eq. (5.33) as

$$\begin{aligned} \frac{d^2\delta\bar{y}_x}{d\bar{z}^2} \cong & -k_0^2 \left[\delta\bar{y}_x + \frac{\bar{\Phi}_Q \tan 2\theta_Q}{\beta} \frac{\alpha_\lambda}{\bar{k}_0^2\gamma\beta} + \frac{\alpha_\lambda\bar{B}_0}{\bar{k}\gamma\beta} \frac{\bar{k}}{\bar{k}_0^2} \frac{d\delta\bar{x}_x}{d\bar{z}} \sin(\bar{k}\bar{z}) \right. \\ & \left. + (1 - r_m) \frac{\alpha_\lambda\bar{B}_0}{\bar{k}\gamma\beta} \cos(\bar{k}\bar{z}) \left(\frac{r_m}{1 - r_m} \frac{\bar{k}^2}{\bar{k}_0^2} - \frac{\bar{b}_{\text{des}}^2}{\bar{a}_{\text{des}}^2} \right) \right], \end{aligned} \quad (5.43)$$

where we have defined

$$\bar{k}_0^2 \equiv \frac{4\bar{I}\alpha_\lambda \bar{a}_{\text{des}}}{\gamma^3 \beta^3 \bar{b}_{\text{des}} (\bar{a}_{\text{des}} + \bar{b}_{\text{des}})^2}. \quad (5.44)$$

We can proceed to solve Eq. (5.43) for $\delta\bar{y}_x$ if we assume that the $d\delta\bar{x}_x/d\bar{z}$ term appearing on the right-hand side of Eq. (5.43) is negligible. This is verified for cases of interest in Appendix C, but relies on a result for $\delta\bar{x}_x$ derived in Section 5.5. Neglecting this term, we can integrate Eq. (5.43) to find the solution

$$\begin{aligned} \delta\bar{y}_x \cong & \frac{\bar{k}_0^2}{\bar{k}^2 - \bar{k}_0^2} (1 - r_m) \frac{\alpha_\lambda \bar{B}_0}{\bar{k}\gamma\beta} \left(\frac{r_m}{1 - r_m} \frac{\bar{k}^2}{\bar{k}_0^2} - \frac{\bar{b}_{\text{des}}^2}{\bar{a}_{\text{des}}^2} \right) \cos(\bar{k}\bar{z}) \\ & + \bar{Y}_x \cos(\bar{k}_0\bar{z} + \varphi_0) - \frac{\bar{\Phi}_Q \tan 2\theta_Q}{\beta} \frac{\alpha_\lambda}{\bar{k}_0^2 \gamma \beta}, \end{aligned} \quad (5.45)$$

where the constants \bar{Y}_x and φ_0 are determined by initial conditions. Notice that a destabilizing resonance is implied by Eq. (5.45) when $\bar{k}^2 \cong \bar{k}_0^2$. However, we will show in Section 5.6 that this resonance is avoided by the condition

$$\bar{k}_0^2 \ll \bar{k}^2, \quad (5.46)$$

which is implied by Eq. (5.4), i.e., the requirement that envelope oscillations in the narrow dimension of the beam remain small.

In order to minimize the long-wavelength trajectory oscillations with wavenumber \bar{k}_0 , we require $\bar{Y}_x = 0$. Moreover, we see that the electrostatic quadrupole rotation angle θ_Q should be such that $\tan \theta_Q = 0$ in order to eliminate the constant part of the trajectory displacement in Eq. (5.45). With these simplifications, we find

$$\delta\bar{y}_x \cong (1 - r_m) \left(\frac{r_m}{1 - r_m} - \frac{\bar{b}_{\text{des}}^2 \bar{k}_0^2}{\bar{a}_{\text{des}}^2 \bar{k}^2} \right) \frac{\alpha_\lambda \bar{B}_0}{\bar{k}\gamma\beta} \cos(\bar{k}\bar{z}). \quad (5.47)$$

If we retain only the lowest order terms in the small quantities r_m , $\bar{b}_{\text{des}}^2/\bar{a}_{\text{des}}^2$, and \bar{k}_0^2/\bar{k}^2 , Eq. (5.47) becomes

$$\delta\bar{y}_x \cong \frac{\alpha_\lambda \bar{B}_0}{\bar{k}\gamma\beta} \left(r_m - \frac{\bar{b}_{\text{des}}^2 \bar{k}_0^2}{\bar{a}_{\text{des}}^2 \bar{k}^2} \right) \cos(\bar{k}\bar{z}). \quad (5.48)$$

Note that while we know each of the parameters r_m , $\bar{b}_{\text{des}}^2/\bar{a}_{\text{des}}^2$, and \bar{k}_0^2/\bar{k}^2 to be small compared to unity, we make no assumptions regarding their relative ordering. Therefore, as we proceed, we shall retain the lowest order terms in each of the small parameters.

5.3.3 Envelope Twist Angle

The envelope angle can now be computed using Eqs. (5.26), (5.33), and (5.48) as

$$\theta \cong \frac{\alpha_\lambda \bar{B}_0}{k\gamma\beta} \frac{\bar{a}_{\text{des}}^2}{\bar{a}_{\text{des}}^2 - \bar{b}_{\text{des}}^2} \left[r_m - \frac{\bar{b}_{\text{des}}^2}{\bar{a}_{\text{des}}^2} \left(1 - r_m + \frac{\bar{k}_0^2}{\bar{k}^2} \right) \right] \cos(\bar{k}\bar{z}), \quad (5.49)$$

which becomes, to lowest order in the small quantities r_m , $\bar{b}_{\text{des}}^2/\bar{a}_{\text{des}}^2$, and \bar{k}_0^2/\bar{k}^2 ,

$$\theta \cong \frac{\alpha_\lambda \bar{B}_0}{k\gamma\beta} \frac{\bar{a}_{\text{des}}^2}{\bar{a}_{\text{des}}^2 - \bar{b}_{\text{des}}^2} \left(r_m - \frac{\bar{b}_{\text{des}}^2}{\bar{a}_{\text{des}}^2} \right) \cos(\bar{k}\bar{z}). \quad (5.50)$$

If we now introduce the notation

$$\varepsilon_r \equiv \frac{\bar{b}_{\text{des}}^2}{\bar{a}_{\text{des}}^2} - r_m, \quad (5.51)$$

then Eq. (5.50) becomes

$$\theta \cong -\varepsilon_r \frac{\bar{a}_{\text{des}}^2}{\bar{a}_{\text{des}}^2 - \bar{b}_{\text{des}}^2} \frac{\alpha_\lambda \bar{B}_0}{k\gamma\beta} \cos(\bar{k}\bar{z}). \quad (5.52)$$

Note that with the proper choice of the aspect ratio parameter of the magnetic field, i.e.,

$$r_m = r_{\text{crit}} \equiv \frac{\bar{b}_{\text{des}}^2}{\bar{a}_{\text{des}}^2 + \bar{b}_{\text{des}}^2}, \quad (5.53)$$

we force $\varepsilon_r = 0$, making the envelope twist vanish. We make this observation parenthetically, however; we shall continue to treat the aspect ratio parameter of the magnetic field r_m as an independent small parameter.

5.4 Applied Fields

5.4.1 Relations for Envelope Perturbations

With the results of Section 5.3 in hand, we derive some intermediate relations for the envelope perturbations, which we will need in order to determine the residual

quadrupole field $\delta\bar{B}_Q$ in Section 5.4.2. For the semi-major axis, we use Eqs. (5.24), (5.33), and (5.48) to find

$$\begin{aligned} \frac{\delta\bar{a}}{\bar{a}_{\text{des}}} - \delta\bar{x}_x &\cong \frac{1}{2(\bar{a}_{\text{des}}^2 - \bar{b}_{\text{des}}^2)} \left(\frac{\alpha_2 \bar{B}_0}{\bar{k}\gamma\beta} \right)^2 \cos^2(\bar{k}\bar{z}) \\ &\times \left[(1 - r_m)^2 \bar{b}_{\text{des}}^2 + \bar{a}_{\text{des}}^2 \left(r_m - \frac{\bar{b}_{\text{des}}^2 \bar{k}_0^2}{\bar{a}_{\text{des}}^2 \bar{k}^2} \right)^2 - 2\bar{a}_{\text{des}}^2 (1 - r_m) \left(r_m - \frac{\bar{b}_{\text{des}}^2 \bar{k}_0^2}{\bar{a}_{\text{des}}^2 \bar{k}^2} \right) \right]. \end{aligned} \quad (5.54)$$

Transforming the cosine term and retaining only the lowest order terms in the small quantities r_m , $\bar{b}_{\text{des}}^2/\bar{a}_{\text{des}}^2$, and \bar{k}_0^2/\bar{k}^2 in Eq. (5.54), we find

$$\frac{\delta\bar{a}}{\bar{a}_{\text{des}}} - \delta\bar{x}_x \cong \frac{\bar{a}_{\text{des}}^2}{4(\bar{a}_{\text{des}}^2 - \bar{b}_{\text{des}}^2)} \left(\frac{\alpha_2 \bar{B}_0}{\bar{k}\gamma\beta} \right)^2 \left(\frac{\bar{b}_{\text{des}}^2}{\bar{a}_{\text{des}}^2} - 2r_m \right) [1 + \cos(2\bar{k}\bar{z})]. \quad (5.55)$$

Similarly, for the semi-minor axis, we use Eqs. (5.25), (5.33), and (5.48) to find

$$\begin{aligned} \frac{\delta\bar{b}}{\bar{b}_{\text{des}}} - \delta\bar{y}_y &\cong \frac{-1}{2(\bar{a}_{\text{des}}^2 - \bar{b}_{\text{des}}^2)} \left(\frac{\alpha_2 \bar{B}_0}{\bar{k}\gamma\beta} \right)^2 \cos^2(\bar{k}\bar{z}) \\ &\times \left[(1 - r_m)^2 \bar{b}_{\text{des}}^2 + \bar{a}_{\text{des}}^2 \left(r_m - \frac{\bar{b}_{\text{des}}^2 \bar{k}_0^2}{\bar{a}_{\text{des}}^2 \bar{k}^2} \right)^2 - 2\bar{b}_{\text{des}}^2 (1 - r_m) \left(r_m - \frac{\bar{b}_{\text{des}}^2 \bar{k}_0^2}{\bar{a}_{\text{des}}^2 \bar{k}^2} \right) \right]. \end{aligned} \quad (5.56)$$

Transforming the cosine term and retaining only the lowest order terms in the small quantities r_m , $\bar{b}_{\text{des}}^2/\bar{a}_{\text{des}}^2$, and \bar{k}_0^2/\bar{k}^2 in Eq. (5.56), we find

$$\frac{\delta\bar{b}}{\bar{b}_{\text{des}}} - \delta\bar{y}_y \cong \frac{-\bar{a}_{\text{des}}^2}{4(\bar{a}_{\text{des}}^2 - \bar{b}_{\text{des}}^2)} \left(\frac{\alpha_2 \bar{B}_0}{\bar{k}\gamma\beta} \right)^2 \left(\frac{\bar{b}_{\text{des}}^2}{\bar{a}_{\text{des}}^2} + r_m^2 \right) [1 + \cos(2\bar{k}\bar{z})]. \quad (5.57)$$

Note that for $r_m = r_{\text{crit}} \cong \bar{b}_{\text{des}}^2/\bar{a}_{\text{des}}^2$, we have

$$\frac{\delta\bar{a}}{\bar{a}_{\text{des}}} - \delta\bar{x}_x \cong \frac{\delta\bar{b}}{\bar{b}_{\text{des}}} - \delta\bar{y}_y \cong \frac{-\bar{b}_{\text{des}}^2}{4(\bar{a}_{\text{des}}^2 - \bar{b}_{\text{des}}^2)} \left(\frac{\alpha_2 \bar{B}_0}{\bar{k}\gamma\beta} \right)^2 [1 + \cos(2\bar{k}\bar{z})]. \quad (5.58)$$

5.4.2 Applied Quadrupole Fields

We are now ready to compute the residual quadrupole field $\delta\bar{B}_Q$, which we will need in order to solve Eqs. (5.29) and (5.41). Let us recall that $\delta\bar{B}_Q$ is defined in Eq. (3.17), i.e.,

$$\beta\delta\bar{B}_Q \equiv (\beta\bar{B}_Q + 2\bar{\Phi}_Q) - \frac{2\bar{I}}{\bar{a}\bar{b}\beta\gamma^2} \frac{\bar{a} + \bar{b} - (\bar{a} - \bar{b})\cos 2\theta}{\bar{a} + \bar{b}}, \quad (5.59)$$

for a non-accelerating beam with $\bar{\Phi}_{00}'' = 0$. Expanding Eq. (5.59) to first order in the perturbed envelope quantities, we find

$$\beta\delta\bar{B}_Q \equiv (\beta\bar{B}_Q + 2\bar{\Phi}_Q) - \frac{4\bar{I}}{\bar{a}_{\text{des}}(\bar{a}_{\text{des}} + \bar{b}_{\text{des}})\beta\gamma^2} \left(1 - \frac{\delta\bar{a}}{\bar{a}_{\text{des}}} - \frac{\delta\bar{a} + \delta\bar{b}}{\bar{a}_{\text{des}} + \bar{b}_{\text{des}}} + \theta^2 \frac{\bar{a}_{\text{des}} - \bar{b}_{\text{des}}}{\bar{b}_{\text{des}}} \right), \quad (5.60)$$

which can be expressed using Eqs. (5.50), (5.55), and (5.57) as

$$\begin{aligned} \delta\bar{B}_Q \equiv & \frac{-4\bar{I}}{\bar{a}_{\text{des}}(\bar{a}_{\text{des}} + \bar{b}_{\text{des}})\beta^2\gamma^2} \left\{ 1 - \frac{2\bar{a}_{\text{des}} + \bar{b}_{\text{des}}}{\bar{a}_{\text{des}} + \bar{b}_{\text{des}}} \delta\bar{x}_x - \frac{\bar{b}_{\text{des}}}{\bar{a}_{\text{des}} + \bar{b}_{\text{des}}} \delta\bar{y}_y \right. \\ & - \frac{2\bar{a}_{\text{des}} + \bar{b}_{\text{des}}}{\bar{a}_{\text{des}} + \bar{b}_{\text{des}}} \frac{\bar{a}_{\text{des}}^2 [1 + \cos(2\bar{k}\bar{z})]}{4(\bar{a}_{\text{des}}^2 - \bar{b}_{\text{des}}^2)} \left(\frac{\alpha_\lambda \bar{B}_0}{\bar{k}\gamma\beta} \right)^2 \left(\frac{\bar{b}_{\text{des}}^2}{\bar{a}_{\text{des}}^2} - 2r_m \right) \\ & + \frac{\bar{b}_{\text{des}}}{\bar{a}_{\text{des}} + \bar{b}_{\text{des}}} \frac{\bar{a}_{\text{des}}^2 [1 + \cos(2\bar{k}\bar{z})]}{4(\bar{a}_{\text{des}}^2 - \bar{b}_{\text{des}}^2)} \left(\frac{\alpha_\lambda \bar{B}_0}{\bar{k}\gamma\beta} \right)^2 \left(\frac{\bar{b}_{\text{des}}^2}{\bar{a}_{\text{des}}^2} + r_m^2 \right) \\ & \left. + \frac{\bar{a}_{\text{des}} - \bar{b}_{\text{des}}}{\bar{b}_{\text{des}}} \frac{\bar{a}_{\text{des}}^4 [1 + \cos(2\bar{k}\bar{z})]}{2(\bar{a}_{\text{des}}^2 - \bar{b}_{\text{des}}^2)^2} \left(\frac{\alpha_\lambda \bar{B}_0}{\bar{k}\gamma\beta} \right)^2 \left(r_m - \frac{\bar{b}_{\text{des}}^2}{\bar{a}_{\text{des}}^2} \right)^2 \right\} \\ & + \left(\bar{B}_Q + \frac{2}{\beta} \bar{\Phi}_Q \right). \end{aligned} \quad (5.61)$$

After some simplification where we retain only the lowest order terms in the small quantities r_m and $\bar{b}_{\text{des}}^2/\bar{a}_{\text{des}}^2$, we separate out the constant and oscillatory terms in Eq. (5.61), i.e.,

$$\begin{aligned} \delta\bar{B}_Q \equiv & \left(\bar{B}_Q + \frac{2}{\beta} \bar{\Phi}_Q \right) - \frac{4\bar{I}}{\bar{a}_{\text{des}}(\bar{a}_{\text{des}} + \bar{b}_{\text{des}})\beta^2\gamma^2} \left[1 - \left(\frac{\alpha_\lambda \bar{B}_0}{\bar{k}\gamma\beta} \right)^2 \frac{\bar{a}_{\text{des}}^3 \sigma}{(\bar{a}_{\text{des}} + \bar{b}_{\text{des}})(\bar{a}_{\text{des}}^2 - \bar{b}_{\text{des}}^2)} \right] \\ & + \frac{4\bar{I}}{\bar{a}_{\text{des}}(\bar{a}_{\text{des}} + \bar{b}_{\text{des}})\beta^2\gamma^2} \left[\left(\frac{\alpha_\lambda \bar{B}_0}{\bar{k}\gamma\beta} \right)^2 \frac{\bar{a}_{\text{des}}^3 \sigma}{(\bar{a}_{\text{des}} + \bar{b}_{\text{des}})(\bar{a}_{\text{des}}^2 - \bar{b}_{\text{des}}^2)} \cos(2\bar{k}\bar{z}) \right. \\ & \left. + \frac{2\bar{a}_{\text{des}} + \bar{b}_{\text{des}}}{\bar{a}_{\text{des}} + \bar{b}_{\text{des}}} \delta\bar{x}_x + \frac{\bar{b}_{\text{des}}}{\bar{a}_{\text{des}} + \bar{b}_{\text{des}}} \delta\bar{y}_y \right], \end{aligned} \quad (5.62)$$

where we have defined the shorthand

$$\sigma \equiv \frac{\bar{b}_{\text{des}}^2}{2\bar{a}_{\text{des}}^2} - r_m - \frac{\bar{a}_{\text{des}} r_m^2}{2\bar{b}_{\text{des}}}. \quad (5.63)$$

We can use Eq. (5.62) to determine the applied quadrupole fields, $(\bar{B}_Q + 2\bar{\Phi}_Q/\beta)$. The simplest solution (corresponding to a single, uniform physical magnet and/or electrodes) is obtained when the applied quadrupole fields are constant. One may also make use of a plurality of similarly-aligned magnets, in which case \bar{B}_Q will be largely constant with some slight longitudinal variation, or a beam tunnel with some axial variation, e.g., a rippled waveguide, in which $\bar{\Phi}_Q$ will also be largely constant with some slight longitudinal variation. For calculation purposes here, we shall assume the quadrupole fields are constant, but the slightly-varying case can also be treated without significant added complexity. If the applied quadrupole fields are constant, all the terms appearing on the first line of the right-hand side of Eq. (5.62) are constant in \bar{z} , and we can minimize the residual quadrupole field (i.e., the perturbation) $\delta\bar{B}_Q$ by choosing the applied fields to satisfy

$$\bar{B}_Q + \frac{2}{\beta}\bar{\Phi}_Q = \frac{4\bar{I}}{\bar{a}_{\text{des}}(\bar{a}_{\text{des}} + \bar{b}_{\text{des}})\beta^2\gamma^2} \left[1 - \left(\frac{\alpha_\lambda \bar{B}_0}{k\gamma\beta} \right)^2 \frac{\bar{a}_{\text{des}}^3 \sigma}{(\bar{a}_{\text{des}} + \bar{b}_{\text{des}})(\bar{a}_{\text{des}}^2 - \bar{b}_{\text{des}}^2)} \right], \quad (5.64)$$

which leaves

$$\begin{aligned} \delta\bar{B}_Q \cong & \frac{4\bar{I}}{\bar{a}_{\text{des}}(\bar{a}_{\text{des}} + \bar{b}_{\text{des}})\beta^2\gamma^2} \left[\left(\frac{\alpha_\lambda \bar{B}_0}{k\gamma\beta} \right)^2 \frac{\bar{a}_{\text{des}}^3 \sigma}{(\bar{a}_{\text{des}} + \bar{b}_{\text{des}})(\bar{a}_{\text{des}}^2 - \bar{b}_{\text{des}}^2)} \cos(2k\bar{z}) \right. \\ & \left. + \frac{2\bar{a}_{\text{des}} + \bar{b}_{\text{des}}}{\bar{a}_{\text{des}} + \bar{b}_{\text{des}}} \delta\bar{x}_x + \frac{\bar{b}_{\text{des}}}{\bar{a}_{\text{des}} + \bar{b}_{\text{des}}} \delta\bar{y}_y \right]. \end{aligned} \quad (5.65)$$

We have now determined the magnitude of the applied quadrupole fields (including lowest-order corrections) in Eq. (5.64) which supports our desired elliptic beam. By minimizing the residual quadrupole field $\delta\bar{B}_Q$, we have minimized the magnitudes of the trajectory perturbations $\delta\bar{x}_x$ and $\delta\bar{y}_y$ which appear in Eq. (5.65). Moreover, we have obtained an expression for the residual quadrupole field $\delta\bar{B}_Q$ in terms of the trajectory perturbations $\delta\bar{x}_x$ and $\delta\bar{y}_y$ which couples Eqs. (5.29) and (5.41).

For a focusing channel with only an applied quadrupole magnetic field (i.e., without an applied quadrupole electrostatic field), Eq. (5.64) yields

$$\bar{B}_Q = \frac{4\bar{I}}{\bar{a}_{\text{des}}(\bar{a}_{\text{des}} + \bar{b}_{\text{des}})\beta^2\gamma^2} \left[1 - \left(\frac{\alpha_\lambda \bar{B}_0}{k\gamma\beta} \right)^2 \frac{\bar{a}_{\text{des}}^3 \sigma}{(\bar{a}_{\text{des}} + \bar{b}_{\text{des}})(\bar{a}_{\text{des}}^2 - \bar{b}_{\text{des}}^2)} \right], \quad (5.66)$$

which will be utilized in the numerical examples presented in Section 5.7.

5.4.3 Applied Longitudinal Magnetic Field

Before we can solve Eqs. (5.29) and (5.41) for the trajectory perturbations $\delta\bar{x}_x$ and $\delta\bar{y}_y$, we must determine the amplitude of the axial magnetic field. We use a method similar to that used to obtain the quadrupole field in Section 5.4.2. Substituting Eq. (5.65) into Eq. (5.29), and Eq. (5.29) into Eq. (5.41), we arrive at

$$\begin{aligned} \frac{d^2\delta\bar{x}_x}{d\bar{z}^2} \cong & \frac{-\alpha_\lambda 4\bar{I}}{\bar{a}_{\text{des}}(\bar{a}_{\text{des}} + \bar{b}_{\text{des}})\beta^3\gamma^3} \left[\left(\frac{\alpha_\lambda \bar{B}_0}{k\gamma\beta} \right)^2 \frac{\bar{a}_{\text{des}}^3 \sigma}{(\bar{a}_{\text{des}} + \bar{b}_{\text{des}})(\bar{a}_{\text{des}}^2 - \bar{b}_{\text{des}}^2)} \cos(2\bar{k}\bar{z}) \right. \\ & \left. + \frac{2\bar{a}_{\text{des}} + \bar{b}_{\text{des}}}{\bar{a}_{\text{des}} + \bar{b}_{\text{des}}} \delta\bar{x}_x + \frac{\bar{b}_{\text{des}}}{\bar{a}_{\text{des}} + \bar{b}_{\text{des}}} \delta\bar{y}_y \right], \end{aligned} \quad (5.67)$$

and

$$\frac{d^2\delta\bar{y}_y}{d\bar{z}^2} + \frac{d^2\delta\bar{x}_x}{d\bar{z}^2} \cong \frac{4\bar{I}\alpha_\lambda}{\bar{a}_{\text{des}}\bar{b}_{\text{des}}\beta^3\gamma^3} \left(1 - \frac{\delta\bar{a}}{\bar{a}_{\text{des}}} - \frac{\delta\bar{b}}{\bar{b}_{\text{des}}} \right) - \frac{\alpha_\lambda^2 \bar{B}_0^2}{2\beta^2\gamma^2} (1 - r_m) [1 - \cos(2\bar{k}\bar{z})]. \quad (5.68)$$

We now substitute Eqs. (5.55) and (5.57) into Eq. (5.68) to obtain

$$\begin{aligned} \frac{d^2\delta\bar{y}_y}{d\bar{z}^2} + \frac{d^2\delta\bar{x}_x}{d\bar{z}^2} \cong & \frac{4\bar{I}\alpha_\lambda}{\bar{a}_{\text{des}}\bar{b}_{\text{des}}\beta^3\gamma^3} (1 - \delta\bar{x}_x - \delta\bar{y}_y) - \frac{\alpha_\lambda^2 \bar{B}_0^2}{2\beta^2\gamma^2} (1 - r_m) [1 - \cos(2\bar{k}\bar{z})] \\ & - \frac{4\bar{I}\alpha_\lambda}{\bar{a}_{\text{des}}\bar{b}_{\text{des}}\beta^3\gamma^3} \frac{\bar{a}_{\text{des}}^2 [1 + \cos(2\bar{k}\bar{z})]}{4(\bar{a}_{\text{des}}^2 - \bar{b}_{\text{des}}^2)} \left(\frac{\alpha_\lambda \bar{B}_0}{k\gamma\beta} \right)^2 \left(\frac{\bar{b}_{\text{des}}^2}{\bar{a}_{\text{des}}^2} - 2r_m \right) \\ & + \frac{4\bar{I}\alpha_\lambda}{\bar{a}_{\text{des}}\bar{b}_{\text{des}}\beta^3\gamma^3} \frac{\bar{a}_{\text{des}}^2 [1 + \cos(2\bar{k}\bar{z})]}{4(\bar{a}_{\text{des}}^2 - \bar{b}_{\text{des}}^2)} \left(\frac{\alpha_\lambda \bar{B}_0}{k\gamma\beta} \right)^2 \left(\frac{\bar{b}_{\text{des}}^2}{\bar{a}_{\text{des}}^2} + r_m^2 \right), \end{aligned} \quad (5.69)$$

which, retaining the lowest order terms in the small quantities r_m and $\bar{b}_{\text{des}}^2/\bar{a}_{\text{des}}^2$, simplifies to

$$\begin{aligned}
\frac{d^2\delta\bar{y}_y}{d\bar{z}^2} + \frac{d^2\delta\bar{x}_x}{d\bar{z}^2} \cong & \frac{4\bar{I}\alpha_\lambda}{\bar{a}_{\text{des}}\bar{b}_{\text{des}}\beta^3\gamma^3} \left[1 + \frac{r_m}{2} \left(\frac{\alpha_\lambda\bar{B}_0}{\bar{k}\beta\gamma} \right)^2 \right] - \frac{\alpha_\lambda^2\bar{B}_0^2}{2\beta^2\gamma^2} (1 - r_m) \\
& + \left[\frac{\alpha_\lambda^2\bar{B}_0^2}{2\beta^2\gamma^2} (1 - r_m) + \frac{4\bar{I}\alpha_\lambda}{\bar{a}_{\text{des}}\bar{b}_{\text{des}}\beta^3\gamma^3} \frac{r_m}{2} \left(\frac{\alpha_\lambda\bar{B}_0}{\bar{k}\beta\gamma} \right)^2 \right] \cos(2\bar{k}\bar{z}) \\
& - \frac{4\bar{I}\alpha_\lambda}{\bar{a}_{\text{des}}\bar{b}_{\text{des}}\beta^3\gamma^3} (\delta\bar{x}_x + \delta\bar{y}_y).
\end{aligned} \tag{5.70}$$

The first line of the right-hand side of Eq. (5.70) is constant, and by requiring it to vanish, i.e.,

$$0 = \frac{4\bar{I}\alpha_\lambda}{\bar{a}_{\text{des}}\bar{b}_{\text{des}}\beta^3\gamma^3} \left[1 + \frac{r_m}{2} \left(\frac{\alpha_\lambda\bar{B}_0}{\bar{k}\beta\gamma} \right)^2 \right] - \frac{\alpha_\lambda^2\bar{B}_0^2}{2\beta^2\gamma^2} (1 - r_m), \tag{5.71}$$

we can minimize the trajectory perturbations. This gives the optimal amplitude of the axial magnetic field,

$$\bar{B}_0^2 = \frac{8\bar{I}}{\bar{a}_{\text{des}}\bar{b}_{\text{des}}\beta\gamma\alpha_\lambda} \left[1 - r_m - \frac{8\bar{I}}{\bar{a}_{\text{des}}\bar{b}_{\text{des}}\beta\gamma\alpha_\lambda} \frac{r_m}{2} \left(\frac{\alpha_\lambda}{\bar{k}\beta\gamma} \right)^2 \right]^{-1}. \tag{5.72}$$

We have now determined the applied axial field magnitude (including lowest order corrections) in Eq. (5.72) required to maintain our desired elliptic beam profile.

5.5 Envelope Perturbations

5.5.1 Normal Modes

Employing Eq. (5.72) to negate the constant term, Eq. (5.70) becomes

$$\frac{d^2}{d\bar{z}^2} (\delta\bar{x}_x + \delta\bar{y}_y) \cong \frac{4\bar{I}\alpha_\lambda}{\bar{a}_{\text{des}}\bar{b}_{\text{des}}\beta^3\gamma^3} \left\{ \left[1 + r_m \left(\frac{\alpha_\lambda\bar{B}_0}{\bar{k}\beta\gamma} \right)^2 \right] \cos(2\bar{k}\bar{z}) - (\delta\bar{x}_x + \delta\bar{y}_y) \right\}. \tag{5.73}$$

Before we can determine the detailed form of the envelope perturbations, we must solve Eqs. (5.67) and (5.73) – a pair of coupled, driven, second-order equations in the trajectory perturbations $\delta\bar{x}_x$ and $\delta\bar{y}_y$.

In order to find the normal modes of oscillation, we first examine the homogeneous versions of Eqs. (5.67) and (5.73),

$$\frac{d^2 \delta \bar{x}_x}{d\bar{z}^2} \cong \frac{-\alpha_\lambda 4\bar{I}}{\bar{a}_{\text{des}}(\bar{a}_{\text{des}} + \bar{b}_{\text{des}})\beta^3 \gamma^3} \left(\frac{2\bar{a}_{\text{des}} + \bar{b}_{\text{des}}}{\bar{a}_{\text{des}} + \bar{b}_{\text{des}}} \delta \bar{x}_x + \frac{\bar{b}_{\text{des}}}{\bar{a}_{\text{des}} + \bar{b}_{\text{des}}} \delta \bar{y}_y \right), \quad (5.74)$$

$$\frac{d^2}{d\bar{z}^2} (\delta \bar{x}_x + \delta \bar{y}_y) \cong \frac{-4\bar{I}\alpha_\lambda}{\bar{a}_{\text{des}} \bar{b}_{\text{des}} \beta^3 \gamma^3} (\delta \bar{x}_x + \delta \bar{y}_y). \quad (5.75)$$

Notice that the form of Eq. (5.75) immediately provides the wavenumber of one normal mode,

$$\bar{k}_+^2 = \frac{4\bar{I}\alpha_\lambda}{\bar{a}_{\text{des}} \bar{b}_{\text{des}} \beta^3 \gamma^3} = \frac{(\bar{a}_{\text{des}} + \bar{b}_{\text{des}})^2}{\bar{a}_{\text{des}}^2} \bar{k}_0^2, \quad (5.76)$$

and the eigenvector for the other mode

$$(\delta \bar{x}_x, \delta \bar{y}_y) \propto (1, -1), \quad (5.77)$$

which has some corresponding wavenumber \bar{k}_- .

We determine the wavenumber \bar{k}_- by examining Eq. (5.74) in the eigenmode corresponding to the eigenvector $(\delta \bar{x}_x, \delta \bar{y}_y)$. In this eigenmode, we substitute $d^2 \delta \bar{x}_x / d\bar{z}^2 = -\bar{k}_-^2 \delta \bar{x}_x$ and $\delta \bar{y}_y = -\delta \bar{x}_x$ into Eq. (5.74) to find

$$-\bar{k}_-^2 \cong \frac{-\alpha_\lambda 4\bar{I}}{\bar{a}_{\text{des}}(\bar{a}_{\text{des}} + \bar{b}_{\text{des}})\beta^3 \gamma^3} \left(\frac{2\bar{a}_{\text{des}} + \bar{b}_{\text{des}}}{\bar{a}_{\text{des}} + \bar{b}_{\text{des}}} - \frac{\bar{b}_{\text{des}}}{\bar{a}_{\text{des}} + \bar{b}_{\text{des}}} \right), \quad (5.78)$$

which simplifies to

$$\bar{k}_-^2 \cong \frac{8\bar{I}\alpha_\lambda}{(\bar{a}_{\text{des}} + \bar{b}_{\text{des}})^2 \beta^3 \gamma^3} = \frac{2\bar{b}_{\text{des}}}{\bar{a}_{\text{des}}} \bar{k}_0^2. \quad (5.79)$$

Similarly, we determine the eigenvector $(\delta \bar{x}_x, \delta \bar{y}_y)^*$ corresponding to the wavenumber \bar{k}_+ by substituting $d^2 \delta \bar{x}_x / d\bar{z}^2 = -\bar{k}_+^2 \delta \bar{x}_x$ into Eq. (5.74), i.e.,

$$-\bar{k}_+^2 \delta \bar{x}_x = \frac{-4\bar{I}\alpha_\lambda}{\bar{a}_{\text{des}}(\bar{a}_{\text{des}} + \bar{b}_{\text{des}})^2 \beta^3 \gamma^3} [\delta \bar{x}_x (2\bar{a}_{\text{des}} + \bar{b}_{\text{des}}) + \delta \bar{y}_y \bar{b}_{\text{des}}], \quad (5.80)$$

which simplifies to

$$\delta \bar{x}_x \left[\bar{k}_+^2 - \bar{k}_-^2 \left(1 + \frac{\bar{b}_{\text{des}}}{2\bar{a}_{\text{des}}} \right) \right] = \delta \bar{y}_y \bar{k}_-^2 \frac{\bar{b}_{\text{des}}}{2\bar{a}_{\text{des}}}. \quad (5.81)$$

The corresponding eigenvector is

$$(\delta\bar{x}_x, \delta\bar{y}_y)^T \propto \left(\bar{k}_-^2 \frac{\bar{b}_{\text{des}}}{2\bar{a}_{\text{des}}}, \bar{k}_+^2 - \bar{k}_-^2 \left[1 + \frac{\bar{b}_{\text{des}}}{2\bar{a}_{\text{des}}} \right] \right). \quad (5.82)$$

5.5.2 Trajectory Perturbations

With the normal modes in hand, we can find the driven part of the general solutions of Eqs. (5.67) and (5.73). Because Eqs. (5.67) and (5.73) are a pair of coupled, driven harmonic oscillator equations with no damping, the trajectory perturbations $\delta\bar{x}_x$ and $\delta\bar{y}_y$ oscillate in phase with the driving term, i.e.,

$$\delta\bar{x}_x = \bar{X}_x \cos(2\bar{k}\bar{z}), \quad (5.83)$$

$$\delta\bar{y}_y = \bar{Y}_y \cos(2\bar{k}\bar{z}), \quad (5.84)$$

where we will solve for the unknown coefficients, \bar{X}_x and \bar{Y}_y .

Substituting Eqs. (5.83) and (5.84) into Eqs. (5.67) and (5.73) and making use of Eqs. (5.76) and (5.79), we find

$$-4\bar{k}^2 \bar{X}_x \cong -\bar{k}_-^2 \left[\frac{1}{2} \left(\frac{\alpha_\lambda \bar{B}_0}{\bar{k}\gamma\beta} \right)^2 \frac{\bar{a}_{\text{des}}^2 \sigma}{(\bar{a}_{\text{des}}^2 - \bar{b}_{\text{des}}^2)} + \left(1 + \frac{\bar{b}_{\text{des}}}{2\bar{a}_{\text{des}}} \right) \bar{X}_x + \frac{\bar{b}_{\text{des}}}{2\bar{a}_{\text{des}}} \bar{Y}_y \right], \quad (5.85)$$

$$-4\bar{k}^2 (\bar{X}_x + \bar{Y}_y) \cong -\bar{k}_+^2 \left\{ (\bar{X}_x + \bar{Y}_y) - \left[1 + r_m \left(\frac{\alpha_\lambda \bar{B}_0}{\bar{k}\beta\gamma} \right)^2 \right] \right\}. \quad (5.86)$$

After some algebra, Eqs. (5.85) and (5.86) imply

$$\bar{X}_x \cong \frac{1}{2} \frac{\bar{k}_-^2}{4\bar{k}^2 - \bar{k}_-^2} \left\{ \left(\frac{\alpha_\lambda \bar{B}_0}{\bar{k}\gamma\beta} \right)^2 \frac{\bar{a}_{\text{des}}^2 \sigma}{(\bar{a}_{\text{des}}^2 - \bar{b}_{\text{des}}^2)} - \frac{\bar{b}_{\text{des}}}{\bar{a}_{\text{des}}} \left[1 + r_m \left(\frac{\alpha_\lambda \bar{B}_0}{\bar{k}\beta\gamma} \right)^2 \right] \frac{\bar{k}_+^2}{4\bar{k}^2 - \bar{k}_+^2} \right\}, \quad (5.87)$$

$$\bar{Y}_y \cong -\bar{X}_x - \frac{\bar{k}_+^2}{4\bar{k}^2 - \bar{k}_+^2} \left[1 + r_m \left(\frac{\alpha_\lambda \bar{B}_0}{\bar{k}\beta\gamma} \right)^2 \right]. \quad (5.88)$$

The general solutions of Eqs. (5.67) and (5.73) can now be written concisely as

$$\delta\bar{x}_x \cong \bar{A}_+ \bar{k}_-^2 \frac{\bar{b}_{\text{des}}}{2\bar{a}_{\text{des}}} \cos(\bar{k}_+ \bar{z} + \varphi_+) + \bar{A}_- \cos(\bar{k}_- \bar{z} + \varphi_-) + \bar{X}_x \cos(2\bar{k}\bar{z}), \quad (5.89)$$

$$\delta\bar{y}_y \cong \bar{A}_+ \left[\bar{k}_+^2 - \bar{k}_-^2 \left(1 + \frac{\bar{b}_{\text{des}}}{2\bar{a}_{\text{des}}} \right) \right] \cos(\bar{k}_+ \bar{z} + \varphi_+) - \bar{A}_- \cos(\bar{k}_- \bar{z} + \varphi_-) + \bar{Y}_y \cos(2\bar{k}\bar{z}), \quad (5.90)$$

where the constants \bar{A}_+ , \bar{A}_- , φ_+ , and φ_- are determined by initial conditions. As expected, destabilizing resonances are implied by Eqs. (5.87) and (5.88) near $4\bar{k}^2 \cong \bar{k}_+^2$ and $4\bar{k}^2 \cong \bar{k}_-^2$. These can be avoided, because Eqs. (5.5), (5.46), (5.76), and (5.79) together imply the ordering

$$\bar{k}_-^2 \ll \bar{k}_0^2 \lesssim \bar{k}_+^2 \ll \bar{k}^2. \quad (5.91)$$

With an appropriate choice of initial conditions, $\bar{A}_+ = \bar{A}_- = 0$, we minimize the long-wavelength oscillations and simplify the trajectory perturbations to the form

$$\delta\bar{x}_x \cong \frac{1}{8} \frac{\bar{k}_-^2}{\bar{k}^2} \left\{ \left(\frac{\alpha_\lambda \bar{B}_0}{\bar{k}\gamma\beta} \right)^2 \frac{\bar{a}_{\text{des}}^2 \sigma}{(\bar{a}_{\text{des}}^2 - \bar{b}_{\text{des}}^2)} - \frac{\bar{b}_{\text{des}}}{\bar{a}_{\text{des}}} \left[1 + r_m \left(\frac{\alpha_\lambda \bar{B}_0}{\bar{k}\beta\gamma} \right)^2 \right] \frac{\bar{k}_+^2}{4\bar{k}^2} \right\} \cos(2\bar{k}\bar{z}), \quad (5.92)$$

$$\delta\bar{y}_y \cong -\frac{1}{8} \left\{ \frac{\bar{k}_-^2}{\bar{k}^2} \left(\frac{\alpha_\lambda \bar{B}_0}{\bar{k}\gamma\beta} \right)^2 \frac{\bar{a}_{\text{des}}^2 \sigma}{(\bar{a}_{\text{des}}^2 - \bar{b}_{\text{des}}^2)} + 2 \frac{\bar{k}_+^2}{\bar{k}^2} \left[1 + r_m \left(\frac{\alpha_\lambda \bar{B}_0}{\bar{k}\beta\gamma} \right)^2 \right] \right\} \cos(2\bar{k}\bar{z}), \quad (5.93)$$

where we have made use of Eq. (5.91) and retained the largest terms.

A further simplification is possible if we note that, to zeroth order, the axial magnetic field is given by Eq. (5.72) as

$$\bar{B}_0^2 \cong \frac{8\bar{I}}{\bar{a}_{\text{des}} \bar{b}_{\text{des}} \beta \gamma \alpha_\lambda}. \quad (5.94)$$

Combining this with Eq. (5.76), we have approximately

$$\left(\frac{\alpha_\lambda \bar{B}_0}{\bar{k}\gamma\beta} \right)^2 \cong 2 \frac{\bar{k}_+^2}{\bar{k}^2}, \quad (5.95)$$

which allows us to express the trajectory perturbations,

$$\delta\bar{x}_x \cong \frac{1}{4} \frac{\bar{k}_-^2}{\bar{k}^2} \frac{\bar{k}_+^2}{\bar{k}^2} \left(\sigma - \frac{1}{8} \frac{\bar{b}_{\text{des}}}{\bar{a}_{\text{des}}} \right) \cos(2\bar{k}\bar{z}), \quad (5.96)$$

$$\delta \bar{y}_y \cong -\frac{1}{4} \frac{\bar{k}_+^2}{\bar{k}^2} \cos(2\bar{k}\bar{z}), \quad (5.97)$$

while keeping the lowest-order terms.

5.5.3 Envelope Perturbations

Finally, we have all the ingredients to express the envelope perturbations by substituting Eqs. (5.96) and (5.97) into Eqs. (5.55) and (5.57), yielding, to lowest order

$$\frac{\delta \bar{a}}{\bar{a}_{\text{des}}} \cong \frac{1}{2} \frac{\bar{k}_+^2}{\bar{k}^2} \left(\frac{\bar{b}_{\text{des}}^2}{\bar{a}_{\text{des}}^2} - 2r_m \right) [1 + \cos(2\bar{k}\bar{z})], \quad (5.98)$$

$$\frac{\delta \bar{b}}{\bar{b}_{\text{des}}} \cong -\frac{1}{2} \frac{\bar{k}_+^2}{\bar{k}^2} \left(\frac{\bar{b}_{\text{des}}^2}{\bar{a}_{\text{des}}^2} + r_m^2 + \frac{1}{2} \cos(2\bar{k}\bar{z}) \right), \quad (5.99)$$

where the wavenumbers are defined in Eqs. (5.44), (5.76), and (5.79) as

$$\bar{k}_0^2 = \frac{4\bar{I}\alpha_\lambda \bar{a}_{\text{des}}}{\gamma^3 \beta^3 \bar{b}_{\text{des}} (\bar{a}_{\text{des}} + \bar{b}_{\text{des}})^2}, \quad (5.100)$$

$$\bar{k}_+^2 = \frac{(\bar{a}_{\text{des}} + \bar{b}_{\text{des}})^2}{\bar{a}_{\text{des}}} \bar{k}_0^2, \quad (5.101)$$

$$\bar{k}_-^2 = \frac{2\bar{b}_{\text{des}}}{\bar{a}_{\text{des}}} \bar{k}_0^2. \quad (5.102)$$

Recall from Eq. (5.52) that the twist angle θ is given, to lowest order, by

$$\theta \cong -\sqrt{2} \frac{\bar{k}_+}{\bar{k}} \left(\frac{\bar{b}_{\text{des}}^2}{\bar{a}_{\text{des}}^2} - r_m \right) \cos(\bar{k}\bar{z}), \quad (5.103)$$

where we have used Eq. (5.95). Because $\bar{k}_+^2/\bar{k}^2 \ll 1$, the amplitudes of these envelope and twist angle perturbations are small.

We can also simplify the applied fields from Eqs. (5.64) and (5.72) using Eqs. (5.44), (5.79), (5.95), and (5.91) to obtain

$$\bar{B}_Q + \frac{2}{\beta} \bar{\Phi}_Q \cong \frac{\bar{k}_0^2 \bar{b}_{\text{des}} (\bar{a}_{\text{des}} + \bar{b}_{\text{des}}) \gamma \beta}{\alpha_\lambda \bar{a}_{\text{des}}^2} \left(1 - 2\sigma \frac{\bar{k}_+^2}{\bar{k}^2} \right), \quad (5.104)$$

$$\bar{B}_0^2 \cong \frac{2\beta^2 \gamma^2 \bar{k}_+^2}{\alpha_\lambda^2 (1 - r_m)}. \quad (5.105)$$

5.5.4 Summary

Knowing now the envelope and particle trajectory perturbations, it is straightforward to determine the distribution matrix elements using the results of Section 2.6.4. Moreover, since the applied fields are known, the equation of motion for the distribution matrix (2.104) can now be integrated and compared with the analytic results (see Section 5.7). This comparison is simplified by noting that, because the envelope perturbations are linear combinations of a constant, $\cos(2\pi\bar{z}/\bar{S})$, or $\cos(4\pi\bar{z}/\bar{S})$ to lowest order, all transverse velocities vanish at the points $\bar{z} = \frac{1}{2}n\bar{S}$, where n is an integer. In any of these planes at $\bar{z} = \frac{1}{2}n\bar{S}$ all of the distribution matrix elements vanish, except M_{xx} , M_{yy} , and $M_{xy} = M_{yx}$.

5.6 Ordering Constraints

5.6.1 Overview

Our analysis has assumed that the applied magnetic fields are well-represented by the paraxial approximation. Using the results of Section 2.3.4, we will estimate the magnitude of the non-paraxial terms and derive conditions that must be satisfied in order to ensure that these non-paraxial terms are negligible. In Section 5.6.2, we will derive a condition for the negligibility of non-paraxial terms in the applied quadrupole magnetic field. We will apply a similar procedure in Section 5.6.3 to obtain a condition on the axial field wavenumber \bar{k} for the negligibility of non-paraxial terms in the applied axial magnetic field. In Section 5.6.4, we will enforce the requirement that the envelope oscillations be small in order to obtain another constraint on the wavenumber \bar{k} . Together, these constraints define an allowed range of axial field wavenumbers for the validity of the paraxial approximations and perturbation expansions used throughout this chapter.

5.6.2 Applied Quadrupole Magnetic Field

The applied quadrupole magnetic field B_Q is generated by the Ψ_{11} term of the magnetic potential [see Eqs. (2.51) and (2.52)]. If this term is axially-varying, it can generate the

non-paraxial terms Ψ_{13} and Ψ_{31} through Eq. (2.48). Without loss of generality, we are free to define

$$g(z) \equiv \frac{\Psi_{13}}{\Psi_{31}}, \quad (5.106)$$

and substitute it into Eq. (2.48) to obtain

$$0 = \Psi_{11}'' + 6(1 + g)\Psi_{31}. \quad (5.107)$$

If we require the higher-order terms to have a negligible contribution to the applied magnetic field compared to the paraxial term (recall $\mathbf{B}_{\text{app}} = -\nabla\Psi$), this implies

$$|3x^2y\Psi_{31}| \ll |y\Psi_{11}|, \quad (5.108)$$

$$|3xy^2\Psi_{13}| \ll |x\Psi_{11}|, \quad (5.109)$$

which simplify using Eqs. (5.106) and (5.107) to

$$|x^2\Psi_{11}''| \ll |2(1 + g)\Psi_{11}|, \quad (5.110)$$

$$|gy^2\Psi_{11}''| \ll |2(1 + g)\Psi_{11}|. \quad (5.111)$$

These conditions must hold for all particles in the beam, but are strictest at the beam edge, i.e.,

$$|a^2\Psi_{11}''| \ll |2(1 + g)\Psi_{11}|, \quad (5.112)$$

$$|gb^2\Psi_{11}''| \ll |2(1 + g)\Psi_{11}|. \quad (5.113)$$

For the beam solution derived in this chapter, the magnetic quadrupole field magnitude can be made axially invariant if the electric quadrupole is, as well [see Eq. (5.64)]. In this case, conditions (5.112) and (5.113) are trivially satisfied, since $\Psi_{11}'' = 0$.

More generally, for beam-matching solutions, the quadrupole field will not be constant, in which case Eqs. (5.112) and (5.113) must be verified. Notice that the largest value of Ψ_{11}''/Ψ_{11} is given by

$$\frac{\Psi''_{11}}{\Psi_{11}} \ll \max_g \left[\min \left(\frac{2(1+g)}{a^2}, \frac{2(1+g)}{gb^2} \right) \right], \quad (5.114)$$

which implies

$$\frac{\Psi''_{11}}{\Psi_{11}} \ll \frac{2}{a^2} + \frac{2}{b^2}, \quad (5.115)$$

when

$$g \rightarrow g_{\text{crit}} \equiv \left(\frac{\Psi_{13}}{\Psi_{31}} \right)_{\text{crit}} = \frac{a^2}{b^2}. \quad (5.116)$$

This suggests that, while non-paraxial magnetic fields cannot be eliminated, their effect can be minimized by a proper choice of aspect ratio. When designing physical magnets to generate a magnetic field for a beam system, it is important to remember that they must be shaped not only to obtain an optimal paraxial field, but also to minimize non-paraxial field errors in the beam envelope. By requiring the aspect ratio of the higher-order magnetic quadrupole field components to take the critical value g_{crit} , we minimize these non-paraxial magnetic field errors.

5.6.3 Axial Magnetic Field

The axial field B_z is generated by Ψ_{00} through the equation $B_z = -d\Psi_{00}/dz$. An oscillatory B_z , such as that in Eq. (5.9), implies an oscillatory Ψ_{00} , which, through Eq. (2.47), implies oscillatory Ψ_{20} and Ψ_{02} . These can contribute, through Eqs. (2.49) and (2.50), to the non-paraxial terms Ψ_{22} , Ψ_{40} , and Ψ_{04} . Without loss of generality, we are free to define

$$f(z) \equiv \frac{\Psi_{22}}{\Psi_{40}}, \quad (5.117)$$

and substitute into Eqs. (2.49) and (2.50) to find

$$0 = \Psi''_{20} + (2f + 12)\Psi_{40}, \quad (5.118)$$

and

$$0 = \Psi''_{20} - \Psi''_{02} + 12(\Psi_{40} - \Psi_{04}), \quad (5.119)$$

where the primes denote differentiation with respect to z . Combining Eqs. (5.118) and (5.119), we find

$$\Psi_{40} = -\frac{\Psi_{20}''}{2(6+f)}, \quad (5.120)$$

$$\Psi_{04} = \frac{\Psi_{20}''f - \Psi_{02}''(6+f)}{12(6+f)}. \quad (5.121)$$

If we require the higher-order terms to have a negligible contribution to the magnetic field, this implies

$$|2xy^2\Psi_{22} + 4x^3\Psi_{40}| \ll |2x\Psi_{20}|, \quad (5.122)$$

$$|2x^2y\Psi_{22} + 4y^3\Psi_{04}| \ll |2y\Psi_{02}|, \quad (5.123)$$

or, making use of Eqs. (5.117), (5.120), and (5.121) to simplify, we find

$$\left| \frac{2y^2f + 4x^2}{2(6+f)} \Psi_{20}'' \right| \ll |2\Psi_{20}|, \quad (5.124)$$

and

$$\left| -x^2 \frac{\Psi_{20}''f}{6+f} + y^2 \frac{\Psi_{20}''f - (6+f)\Psi_{02}''}{3(6+f)} \right| \ll |2\Psi_{02}|. \quad (5.125)$$

Equations (5.124) and (5.125) provide the conditions that must be satisfied if the non-paraxial magnetic field is to be negligible in the x -direction and y -direction, respectively.

When the axial magnetic field varies sinusoidally with a dimensionless wavenumber \bar{k} , Eq. (5.124) can be expressed as

$$\left| \frac{\bar{k}^2}{2(6+f)} \left| \bar{y}^2f + 2\bar{x}^2 \right| \right| \ll 1. \quad (5.126)$$

This condition holds for all particles in the beam, but the particular coordinate position where it is strictest depends critically on the value of f . In fact, if we maximize the absolute value appearing in Eq. (5.126) for all values of f , we find

$$\frac{\bar{k}^2}{2|6+f|} \left\{ \begin{array}{ll} \bar{b}^2 f + 2\bar{a}^2 & , 0 \leq f \\ 2\bar{a}^2 & , -2\bar{a}^2/\bar{b}^2 < f < 0 \\ |f|\bar{b}^2 & , f \leq -2\bar{a}^2/\bar{b}^2 \end{array} \right\} \ll 1, \quad (5.127)$$

which gives us an overall condition the beam must satisfy if the non-paraxial magnetic field is to be negligible in the x -direction.

Similarly, for the y -direction, when the axial field varies with a dimensionless wavenumber \bar{k} , Eq. (5.125) can be expressed as

$$\frac{\bar{k}^2}{2|6+f|} \left| -\bar{x}^2 f \frac{r_m}{1-r_m} + \frac{\bar{y}^2}{3} \left[f \frac{r_m}{1-r_m} - (6+f) \right] \right| \ll 1, \quad (5.128)$$

which simplifies, for $|r_m| \ll 1$, to

$$\frac{\bar{k}^2}{2|6+f|} \left| \bar{x}^2 f r_m + \frac{\bar{y}^2}{3} (6+f) \right| \ll 1. \quad (5.129)$$

Maximizing the absolute value that appears in Eq. (5.129) for all values of f and r_m , we find

$$\frac{\bar{k}^2}{2|6+f|} \left\{ \begin{array}{l} \left\{ \begin{array}{l} |fr_m|\bar{a}^2 + \frac{\bar{b}^2}{3}(6+|f|) \quad , 0 \leq f \\ \frac{\bar{b}^2}{3}(6-|f|) \quad , \frac{-6\bar{b}^2}{3r_m\bar{a}^2 + \bar{b}^2} < f < 0 \\ |fr_m|\bar{a}^2 \quad , -6 < f \leq \frac{-6\bar{b}^2}{3|r_m|\bar{a}^2 + \bar{b}^2} \\ |fr_m|\bar{a}^2 + \frac{\bar{b}^2}{3}(|f|-6) \quad , f \leq -6 \end{array} \right\} \quad , 0 \leq r_m \\ \left\{ \begin{array}{l} \frac{\bar{b}^2}{3}(6+|f|) \quad , 0 \leq f \\ |fr_m|\bar{a}^2 + \frac{\bar{b}^2}{3}(6-|f|) \quad , -6 < f < 0 \\ |fr_m|\bar{a}^2 \quad , \frac{-6\bar{b}^2}{\bar{b}^2 - 3|r_m|\bar{a}^2} < f \leq 6 \\ \frac{\bar{b}^2}{3}(|f|-6) \quad , f < \frac{-6\bar{b}^2}{\bar{b}^2 - 3|r_m|\bar{a}^2} \end{array} \right\} \quad , \frac{-\bar{b}^2}{3\bar{a}^2} < r_m < 0 \\ \left\{ \begin{array}{l} |fr_m|\bar{a}^2 \quad , \frac{6\bar{b}^2}{3|r_m|\bar{a}^2 - \bar{b}^2} \leq f \\ \frac{\bar{b}^2}{3}(6+|f|) \quad , 0 < f \leq \frac{6\bar{b}^2}{3|r_m|\bar{a}^2 - \bar{b}^2} \\ |fr_m|\bar{a}^2 + \frac{\bar{b}^2}{3}(6-|f|) \quad , -6 < f \leq 0 \\ |fr_m|\bar{a}^2 \quad , f \leq -6 \end{array} \right\} \quad , r_m \leq \frac{-\bar{b}^2}{3\bar{a}^2} \end{array} \right\} \ll 1, \quad (5.130)$$

which gives us an overall condition which must be satisfied if the non-paraxial magnetic field is to be negligible in the y -direction.

We need only to show Eqs. (5.127) and (5.130) can be satisfied for some chosen f and $|r_m| \ll 1$, but a naïve choice can be overly restrictive. For example, if we consider $f = 0$, then Eq. (5.127) implies

$$\frac{\bar{k}^2\bar{a}^2}{6} \ll 1. \quad (5.131)$$

On the other hand, if we consider the case where $r_m > 0$ and $f \gg 6$, Eqs. (5.127) and (5.130) imply

$$\bar{k}^2 \left(\frac{\bar{a}^2}{f} + \frac{\bar{b}^2}{2} \right) \ll 1, \quad (5.132)$$

$$\bar{k}^2 \left(\frac{r_m \bar{a}^2}{2} + \frac{\bar{b}^2}{6} \right) \ll 1. \quad (5.133)$$

If we now specify a sufficiently large f satisfying

$$6 \frac{\bar{a}^2}{\bar{b}^2} \leq f, \quad (5.134)$$

and sufficiently small r_m such that

$$r_m \leq r_{\text{crit}} \equiv \frac{\bar{b}^2}{\bar{a}^2}, \quad (5.135)$$

then Eqs. (5.132) and (5.133) reduce to

$$\frac{2}{3} \bar{k}^2 \bar{b}^2 \ll 1, \quad (5.136)$$

or, equivalently,

$$\frac{2}{3} (2\pi \bar{b})^2 \ll \bar{S}^2. \quad (5.137)$$

Equation (5.137) provides a constraint on the minimum allowed wavelength of the axial magnetic field that is consistent with the paraxial approximation. As we saw in Section 5.6.2, the non-paraxial magnetic field geometry is critical in maintaining the validity of the paraxial approximation across the beam envelope. In this case, for the axial magnetic field, we see that the parameter $f \equiv \Psi_{22}/\Psi_{40}$ will generally need to be rather large (of the order of \bar{a}^2/\bar{b}^2) if we wish to work with axial magnetic field wavelengths which approach the order of the narrow beam dimension.

5.6.4 Small Envelope Oscillation Constraint and Summary of Ordering

An additional constraint on the wavenumber \bar{k} is obtained by applying Eq. (5.5) (small envelope oscillations in the short dimension) to Eq. (5.99), which yields

$$\frac{1}{4} \frac{\bar{k}_+^2}{\bar{k}^2} \ll 1, \quad (5.138)$$

or

$$\frac{1}{4} \frac{\bar{k}_0^2}{\bar{k}^2} \ll 1, \quad (5.139)$$

which proves Eq. (5.46).

We can now summarize the ordering constraints on the wavenumber \bar{k} using Eqs. (5.91), (5.136), and (5.139) as

$$\frac{1}{4} \bar{k}_-^2 \ll \frac{1}{8} \frac{\bar{a}_{des}}{\bar{b}_{des}} \bar{k}_-^2 \cong \frac{1}{4} \bar{k}_0^2 \approx \frac{1}{4} \bar{k}_+^2 \ll \bar{k}^2 \ll \frac{3}{2 \bar{b}_{des}^2}. \quad (5.140)$$

In terms of the corresponding wavelengths, the ordering relation is

$$\frac{8\pi^2 \bar{b}_{des}^2}{3} \ll \bar{S}^2 \ll 4\bar{S}_+^2 \approx 4\bar{S}_0^2 \cong 8 \frac{\bar{b}_{des}}{\bar{a}_{des}} \bar{S}_-^2 \ll 4\bar{S}_-^2. \quad (5.141)$$

5.7 Numerical Results

5.7.1 6:1 Nonrelativistic Beam

Let us consider a 6:1 elliptic electron beam with desired envelopes semi-axes $a_{des} = 0.373$ cm and $b_{des} = 0.062$ cm propagating with current $I = 0.11$ A along a beam tunnel with a constant axial potential of $\Phi_{00} = 2290$ V. For this beam, then, we have $\beta = 0.094$ and $\gamma = 1.0045$. Let us choose a reference length of $\lambda = b_{des}$, which sets the dimensionless parameters

$$\alpha_\lambda \equiv \frac{q^2}{\lambda m c^2} = 4.53 \times 10^{-12}, \quad (5.142)$$

$$\bar{k}_0^2 = \frac{4\bar{I}\alpha_\lambda \bar{a}_{des}}{\gamma^3 \beta^3 \bar{b}_{des} (\bar{a}_{des} + \bar{b}_{des})^2} = 0.00372, \quad (5.143)$$

$$\bar{k}_+^2 = \frac{(\bar{a}_{des} + \bar{b}_{des})^2}{\bar{a}_{des}^2} \bar{k}_0^2 = 0.00506, \quad (5.144)$$

and

$$\bar{k}_-^2 = \frac{2\bar{b}_{\text{des}}}{\bar{a}_{\text{des}}} \bar{k}_0^2 = 0.00124. \quad (5.145)$$

First, let us determine which values of the dimensionless longitudinal magnetic period \bar{S} are allowed by the constraints of Eq. (5.137). We find

$$\frac{8\pi^2}{3} \bar{b}^2 \ll \bar{S}^2 \ll 4\bar{S}_+^2, \quad (5.146)$$

or

$$(5.13)^2 \ll \bar{S}^2 \ll (177)^2, \quad (5.147)$$

which leaves a reasonable range within which \bar{S} can be chosen to satisfy both constraints. For illustrative purposes, we choose $\bar{S} = 30.84$, i.e., $S = \lambda\bar{S} = 1.912$ cm.

Let us find a solution with the magnetic field aspect ratio $r_m = 0$. The applied quadrupole field is determined by Eq. (5.104),

$$\left(B_Q + \frac{\Phi_Q}{\beta} \right) = \frac{q}{\lambda^2} \left(\bar{B}_Q + \frac{\bar{\Phi}_Q}{\beta} \right) = -1.873 \text{ G}, \quad (5.148)$$

which corresponds to an on-axis transverse field gradient of

$$\left(\frac{\partial B_y}{\partial x} \right)_{00} = \frac{B_Q}{\lambda} = 30.21 \text{ G/cm}, \quad (5.149)$$

when $\Phi_Q = 0$. The longitudinal field can be obtained from Eq. (5.105), yielding

$$B_0 = \frac{q}{\lambda^2} \bar{B}_0 = -261.32 \text{ G}. \quad (5.150)$$

The envelope values are computed from Eqs. (5.98), (5.99), and (5.103) to yield

$$a = \lambda \bar{a} = [0.37363 + 0.00063 \cos(2kz)] \text{ cm}, \quad (5.151)$$

$$b = \lambda \bar{b} = [0.0621 - 0.0019 \cos(2kz)] \text{ cm}, \quad (5.152)$$

$$\theta = -0.014 \cos(kz) \text{ rad}. \quad (5.153)$$

With these analytic forms for the envelope quantities and the zero emittance assumption, we can specify initial conditions for the distribution matrix $\underline{\underline{\mathbf{M}}}$ using the results of Section 2.6.4, while the values for the applied magnetic fields determine the force matrix $\underline{\underline{\mathbf{F}}}$ through Eq. (2.71). We can now utilize standard numeric techniques to integrate Eq. (2.104) in order to evolve the distribution matrix forward in the axial coordinate z . With knowledge of $\underline{\underline{\mathbf{M}}}(z)$, we can again use the results of Section 2.6.4 to determine the envelope quantities. The envelope semi-axes $a(z)$ and $b(z)$ are shown in Figure 5.1, and the twist angle $\theta(z)$ is shown in Figure 5.2. Clearly, the beam envelope is well-confined and follows the desired trajectory to a good approximation.

As a separate verification of the theory and envelope code, a 3D OMNITRAK [38] simulation is performed for the 6:1 elliptic beam. Since 3D trajectory simulations are time-intensive, only a 2-period interval is used for this test, as shown in Figure 5.3. The beam is sent through a conducting rectangular beam tunnel (not shown) of width 10.74 mm and height 7.0 mm. The beam's entrance conditions are specified by Eqs. (5.151), (5.152), and (5.153), while the confining fields are given by Eqs. (5.148) and (5.150). Substantially parallel, non-twisting transport is achieved.

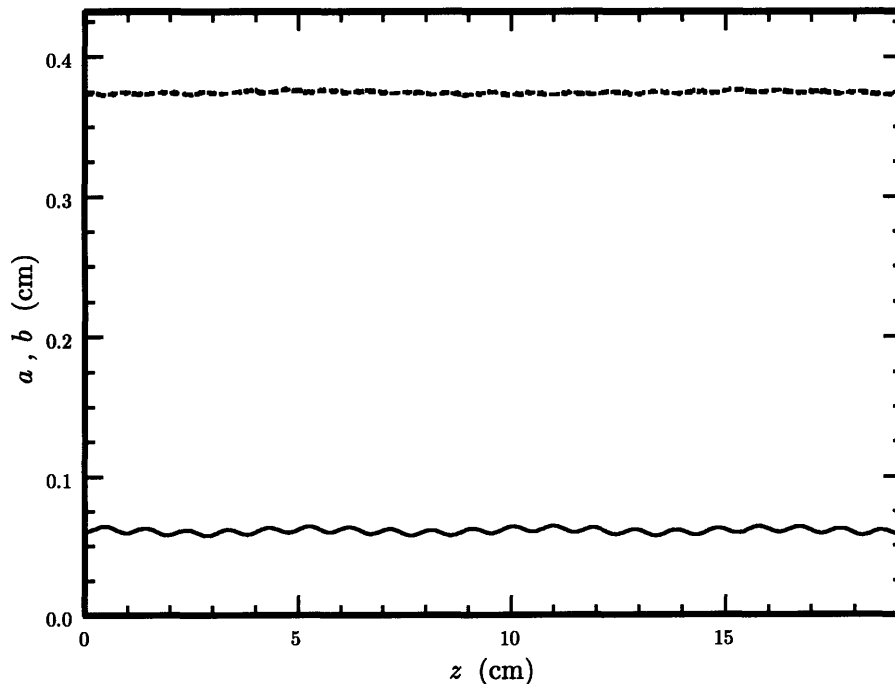


Figure 5.1: Beam envelope semi-major axis $a(z) \cong 0.373$ cm (dotted line) and semi-minor axis $b(z) \cong 0.062$ cm (solid line) of the 6:1 elliptic beam over 10 longitudinal magnetic periods, $10S = 19.12$ cm.

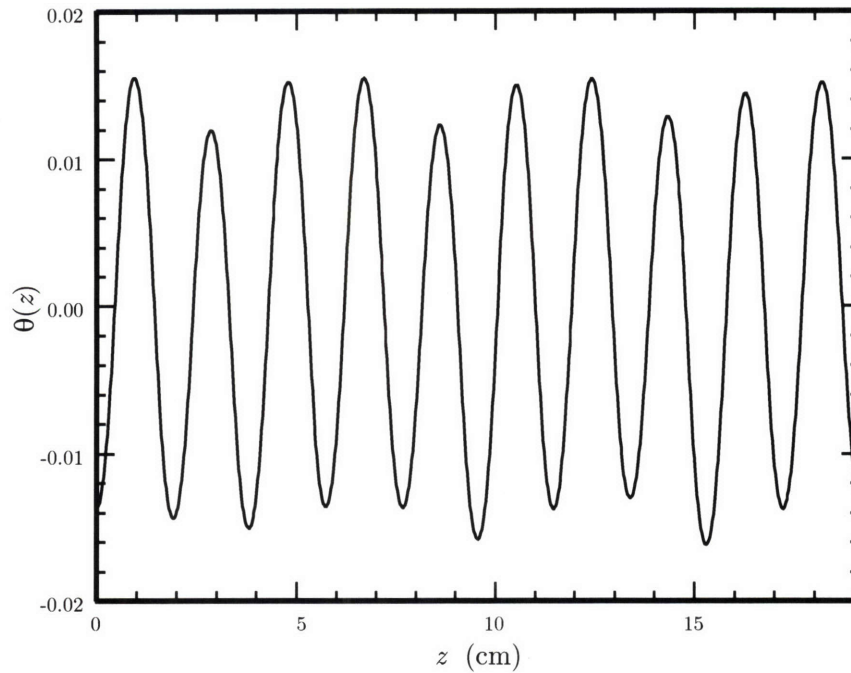


Figure 5.2: Beam envelope twist angle $\theta(z)$ of the 6:1 elliptic beam over 10 longitudinal magnetic periods, $10S = 19.12$ cm.

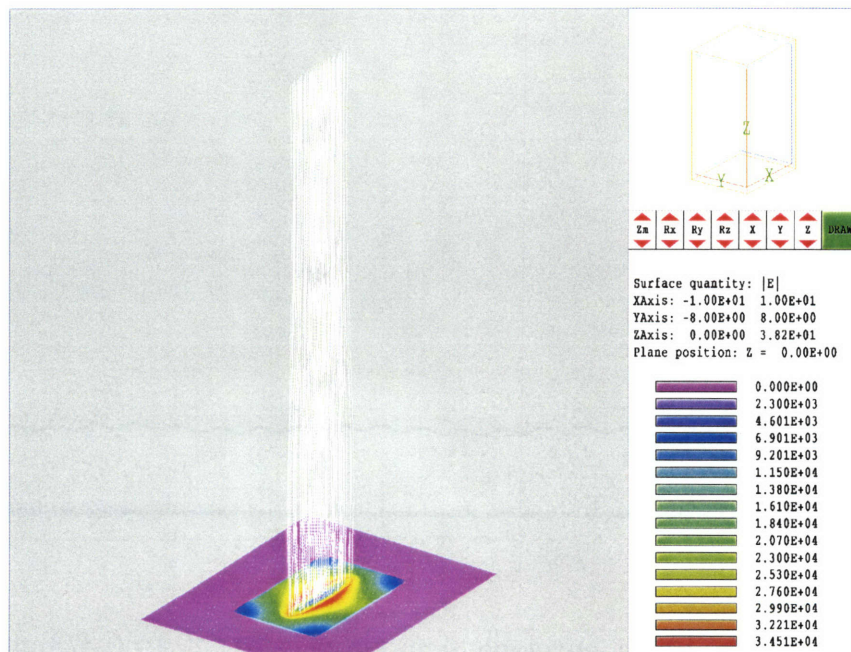


Figure 5.3: Particle trajectories for a 3D Omnitrak simulation of the 6:1 elliptic beam over 2 longitudinal magnetic periods, $2S = 3.824$ cm.

5.7.2 10:1 Relativistic Beam

Let us consider a 10:1 relativistic elliptic electron beam with desired envelope semi-axes $a_{\text{des}} = 0.4 \text{ cm}$ and $b_{\text{des}} = 0.04 \text{ cm}$ and axial kinetic energy of 500 kV (i.e., $\Phi_{00} = 500 \text{ kV}$) propagating with current $I = 150 \text{ A}$ along a beam tunnel. For this elliptic beam, we have $\beta = 0.863$ and $\gamma = 1.978$. Let us choose a reference length of $\lambda = b_{\text{des}}$, which sets the dimensionless parameters

$$\alpha_i \equiv \frac{q^2}{\lambda m c^2} = 7.04 \times 10^{-12}, \quad (5.154)$$

$$\bar{k}_0^2 = \frac{4I\alpha_i \bar{a}_{\text{des}}}{\gamma^3 \beta^3 \bar{b}_{\text{des}} (\bar{a}_{\text{des}} + \bar{b}_{\text{des}})^2} = 0.000586, \quad (5.155)$$

$$\bar{k}_+^2 = \frac{(\bar{a}_{\text{des}} + \bar{b}_{\text{des}})^2}{\bar{a}_{\text{des}}^2} \bar{k}_0^2 = 0.000709, \quad (5.156)$$

and

$$\bar{k}_-^2 = \frac{2\bar{b}_{\text{des}}}{\bar{a}_{\text{des}}} \bar{k}_0^2 = 0.000117. \quad (5.157)$$

First, let us determine which values of the longitudinal magnetic period $S = \lambda \bar{S}$ are allowed by the constraints of Eq. (5.137). We find

$$\frac{8\pi^2}{3} \bar{b}^2 \ll \bar{S}^2 \ll 4\bar{S}_+^2, \quad (5.158)$$

or

$$(5.13)^2 \ll \bar{S}^2 \ll (519)^2, \quad (5.159)$$

which leaves a reasonable range within which \bar{S} can be chosen to satisfy both constraints. For illustrative purposes, we choose $\bar{S} = 50$, i.e., $S = \lambda \bar{S} = 2 \text{ cm}$.

Let us find a solution with the magnetic field aspect ratio $r_m = 0$. The applied quadrupole field is determined by Eq. (5.104),

$$\left(B_q + \frac{\Phi_q}{\beta} \right) = \frac{q}{\lambda^2} \left(\bar{B}_q + \frac{\bar{\Phi}_q}{\beta} \right) = -4.685 \text{ G}, \quad (5.160)$$

which corresponds to an on-axis transverse field gradient of

$$\left(\frac{\partial B_y}{\partial x} \right)_{00} = \frac{B_Q}{\lambda} = 117.13 \text{ G/cm} , \quad (5.161)$$

when $\Phi_Q = 0$. The longitudinal field can be obtained from Eq. (5.105), yielding

$$B_0 = \frac{q}{\lambda^2} \bar{B}_0 = -2738.14 \text{ G} . \quad (5.162)$$

The envelope values are computed from Eqs. (5.98), (5.99), and (5.103) to yield

$$a = \lambda \bar{a} = [0.40009 + 0.00009 \cos(2kz)] \text{ cm} , \quad (5.163)$$

$$b = \lambda \bar{b} = [0.039991 - 0.00045 \cos(2kz)] \text{ cm} , \quad (5.164)$$

$$\theta = -0.0030 \cos(kz) \text{ rad} . \quad (5.165)$$

Integrating Eq. (2.104) to determine the beam evolution, we plot the beam envelope semi-axes $a(z)$ and $b(z)$ in Figure 5.3, and the twist angle $\theta(z)$ in Figure 5.4. Once again, we find that the beam is well-confined and follows the desired trajectory to a good approximation.

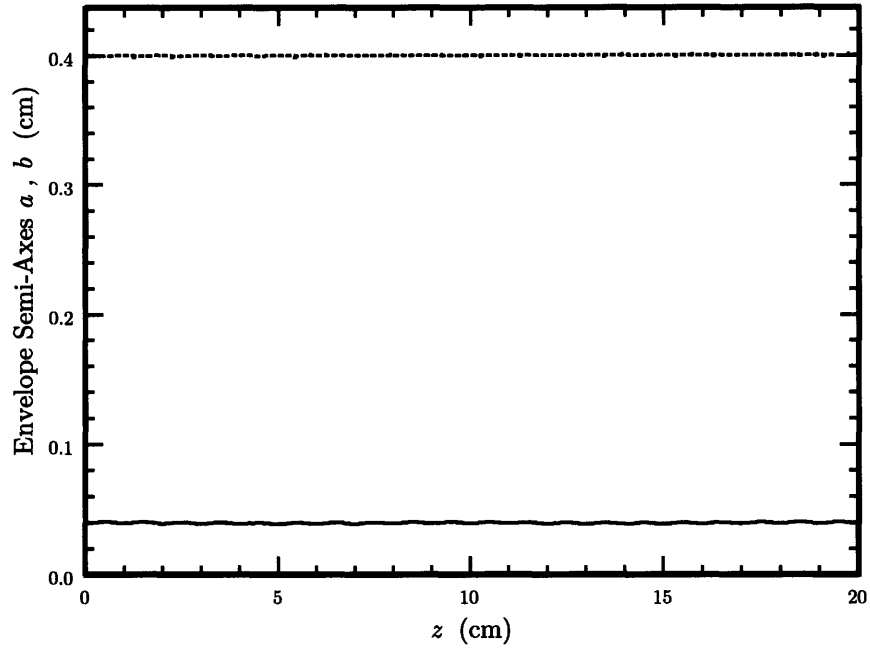


Figure 5.4: Beam envelope semi-major axis $a(z) \cong 0.4$ cm (dotted line) and semi-minor axis $b(z) \cong 0.04$ cm (solid line) of the 10:1 relativistic elliptic beam over 10 longitudinal magnetic periods, $10S = 20$ cm.

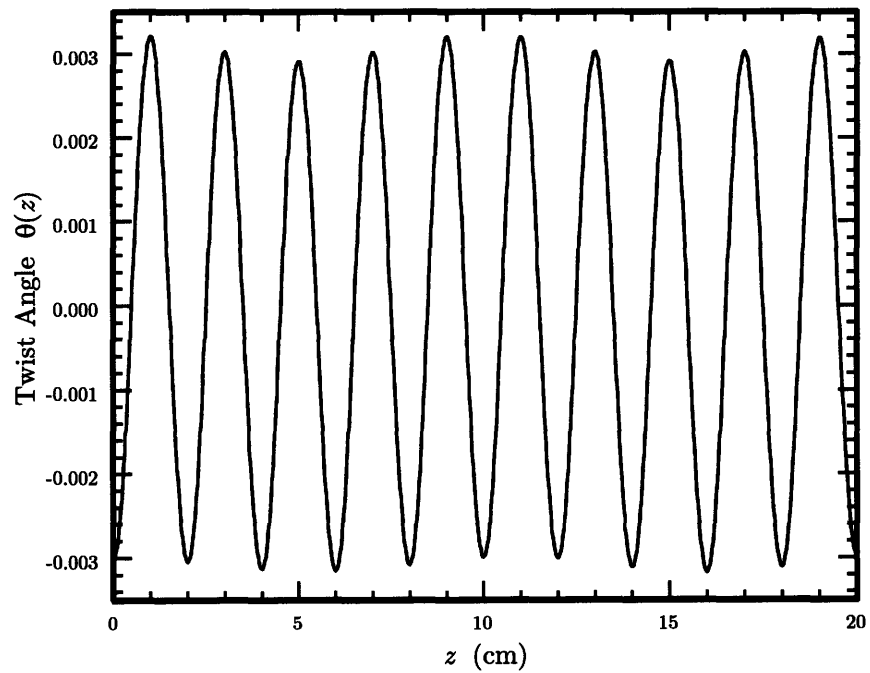


Figure 5.5: Beam envelope twist angle $\theta(z)$ of the 10:1 relativistic elliptic beam over 10 longitudinal magnetic periods, $10S = 20$ cm.

6 Elliptic Beams in Transition

6.1 Overview

In Chapter 4, we solved the inverse problem of obtaining the external electrode structure required to accelerate an elliptic beam of a constant cross-section, and in Chapter 5, we solved the inverse problem of confining a coasting elliptic beam of a nearly constant cross-section. More complex situations involve transitions; for example, an elliptic beam may flow between an accelerating region and a coasting region or the cross-section of the elliptic beam may vary. For these cases, the results of Chapter 4 or Chapter 5 can be applied to obtain solutions before or after the transition, but we must use the approximate techniques of Chapter 3 (particularly, the *small residual quadrupole* regime in Section 3.4.7) in order to match the beam solutions through the transition region. Because of the approximations used, the matched solutions presented in this chapter will generally be less accurate than those derived in Chapter 4 and Chapter 5, however, they still provide a very good first-pass matched-beam solution which can be refined through numerical optimization, as will be demonstrated in numerical examples.

We will present two examples of the application of techniques of Chapter 3 to transitional problems. In Section 6.2, we consider a constant-envelope beam transitioning from an accelerating region to a coasting region, i.e., the beam injection matching problem. We prescribe a semi-analytic technique which can be used to design the electrode geometry and applied fields that will produce a high-quality, laminar elliptic beam. We extract it from a diode and propagate it through a beam tunnel while maintaining a constant beam cross-section. In Section 6.3, we consider a parallel-flow, coasting beam whose cross-section undergoes compression before resuming parallel flow, i.e., the beam compression problem. We analytically prescribe a set of applied fields that achieves this flow profile.

6.2 Beam Injection Matching

6.2.1 Overview

In Chapter 4 and Chapter 5, we considered the problems of beam formation and beam transport in isolation, but any practical device must solve both these problems. A beam cannot be transported unless it is first formed, and a beam which is formed is useless if

not transported. Modeling the dynamics of a charged-particle beam that is injected from a diode into a transport tube is one of the more challenging problems in beam physics. Conventional approaches rely on extensive simulation, multi-parameter, multi-dimensional optimization, and a great deal of trial and error. For 3D elliptic beams, in particular, these approaches can be prohibitively time-consuming, if they produce a reasonable solution at all. We present, in this section, an alternative approach. In Section 6.2.2, we use the methods of Chapter 3 to relate the electrostatic potential of the beam system to the required confining magnetic fields. In Section 6.2.3, we outline a semi-analytic solution technique that quickly converges to an acceptable solution of the beam injection matching problem. In Section 6.2.4, we present an example calculation of beam injection matching for a 6:1 nonrelativistic elliptic electron beam.

6.2.2 Applied Magnetic Fields in the Transition Region

We consider a space-charge-dominated, large-aspect-ratio elliptic beam which is created and accelerated in a space-charge-limited diode (see Chapter 4), passes through a transitional region near the anode hole, and then enters a drift tube through which it coasts with constant velocity (see Chapter 5), all the while with a constant beam cross-section. The dimensionless axial electrostatic potential $\bar{\Phi}_{00}$ for such a beam will follow the Child-Langmuir [29] form in the diode region and smoothly transition to a constant in the coasting beam region. Outside the transition region, we have already inverted the problem to determine the appropriate applied fields and electrode geometries (see Chapter 4 and Chapter 5), therefore we know both the form of the axial potential and the form of the applied fields and electrode geometry outside the transition region. Because we assume a space-charge-dominated beam, emittance effects are negligible [16] [27] [28] and the beam takes a cold-fluid form in which fluid elements follow single particle trajectories in the transition region. If the transition occurs over a characteristic scale length \bar{S}_{des} (see Section 3.1), we can use the methods in Chapter 3 to model the beam behavior in the transition region.

The Child-Langmuir solution, which derives from the *small fields, no-oscillation* regime in Section 3.4.2, and the coasting beam solution, which derives from the *small residual quadrupole field* regime in Section 3.4.7, both require the condition in Eq. (3.43), i.e.,

$$|\delta \bar{B}_q| \ll \frac{\gamma \beta}{\alpha_x \bar{S}_{\text{des}}^2}. \quad (6.1)$$

Assuming a smooth transition, we require that the condition in Eq. (6.1) also holds in the transition region. Under such circumstances, using Eq. (3.17) and taking the limit $\theta \rightarrow 0$, we find that in the transition region we have

$$\left| \bar{B}_Q + \frac{2}{\beta} \bar{\Phi}_Q - \left(\frac{4\bar{I}}{\bar{a}\bar{b}\beta^2\gamma^2} + \frac{1}{\beta} \bar{\Phi}_{00}'' \right) \frac{\bar{b}}{\bar{a} + \bar{b}} \right| \ll \frac{\gamma\beta}{\alpha_\lambda \bar{S}_{\text{des}}^2}, \quad (6.2)$$

which is satisfied by choosing

$$\bar{B}_Q = \left(\frac{4\bar{I}}{\bar{a}\bar{b}\beta^2\gamma^2} + \frac{1}{\beta} \bar{\Phi}_{00}'' \right) \frac{\bar{b}}{\bar{a} + \bar{b}} - \frac{2}{\beta} \bar{\Phi}_Q. \quad (6.3)$$

Equation (6.3) specifies the form of the matched applied quadrupole magnetic field in the transition region in terms of the unknown axial electrostatic potential $\bar{\Phi}_{00}(\bar{z})$ and the unknown electrostatic quadrupole potential $\bar{\Phi}_Q(\bar{z})$. Note that γ and β are related to $\bar{\Phi}_{00}$ by $\gamma = 1 + \alpha_\lambda \bar{\Phi}_{00}$ and $\beta^2 = 1 - \gamma^{-2}$ [see Eqs. (2.19) and (2.20)].

Similarly, we obtain a matched axial field \bar{B}_z by assuming the desired solution exists in the *small residual quadrupole field* regime in the transition region. Therefore, Eq. (3.66) holds, i.e.,

$$\frac{d\bar{p}_y}{d\bar{z}} - \frac{\alpha_\lambda \bar{y}}{\beta} \left(\frac{4\bar{I}}{\bar{a}\bar{b}\beta\gamma^2} + \bar{\Phi}_{00}'' - \frac{\alpha_\lambda}{\gamma} \bar{B}_z^2 \right) \sim \mathcal{O} \left(\frac{1}{\bar{S}_{\text{des}}^2} \left[\bar{b}\gamma\beta + \frac{\bar{a}^2}{\bar{b}} \beta\gamma \right] \right). \quad (6.4)$$

We take an axial magnetic field of the form

$$\bar{B}_z(\bar{z}) = \bar{B}_0(\bar{z}) \sin \left(\frac{2\pi\bar{z}}{\bar{S}} + \varphi(\bar{z}) \right), \quad (6.5)$$

where φ is a parameter that represents a slowly-varying phase shift of the axial magnetic field, and the amplitude \bar{B}_0 varies slowly on the length scale \bar{S}_{des} with $\bar{S} \ll \bar{S}_{\text{des}}$. If we now perform a *local average* of Eq. (6.4) over the magnetic oscillation wavelength \bar{S} , the momentum term vanishes by the assumption of a constant beam envelope, and we find

$$\frac{\alpha_\lambda \bar{y}}{\beta} \left(\frac{4\bar{I}}{\bar{a}\bar{b}\beta\gamma^2} + \bar{\Phi}_{00}'' - \frac{\alpha_\lambda}{\gamma} \frac{\bar{B}_0^2}{2} \right) \sim \mathcal{O} \left(\frac{1}{\bar{S}_{\text{des}}^2} \left\langle \bar{b}\gamma\beta + \frac{\bar{a}^2}{\bar{b}} \beta\gamma \right\rangle \right), \quad (6.6)$$

where the angle brackets denote the *local average*. Equation (6.6) is satisfied by choosing

$$\bar{B}_0^2 = \frac{2\gamma\beta}{\alpha_\chi} \left(\frac{4\bar{I}}{\bar{a}\bar{b}\beta^2\gamma^2} + \frac{1}{\beta} \bar{\Phi}_{00}' \right), \quad (6.7)$$

which specifies the form of the matched axial magnetic field in the transition region in terms of the unknown axial electrostatic potential $\bar{\Phi}_{00}(\bar{z})$. Again, note that γ and β are related to $\bar{\Phi}_{00}$ by $\gamma = 1 + \alpha_\chi \bar{\Phi}_{00}$ and $\beta^2 = 1 - \gamma^{-2}$ [see Eqs. (2.19) and (2.20)].

6.2.3 Semi-Analytic Solution Technique

Equations (6.3) and (6.7) specify the applied fields in the transition region in terms of the unknown axial electrostatic potential $\bar{\Phi}_{00}(\bar{z})$ and the unknown quadrupole potential $\bar{\Phi}_Q(\bar{z})$. In principle, we have the freedom to choose arbitrary functional forms for these potentials. Once the potentials $\bar{\Phi}_{00}(\bar{z})$ and $\bar{\Phi}_Q(\bar{z})$ are given (and the desired beam envelope semi-axes \bar{a} and \bar{b} are chosen), the beam velocity profile is determined through Eq. (2.18), and the transverse electrostatic potentials in the beam interior are determined through Eqs. (2.38), (2.39), and (2.40) with $\theta = 0$. Laplace's equation $\nabla^2 \bar{\Phi} = 0$, together with the electrostatic potential and its derivatives on the beam boundary, fully defines an inverse problem for determining the potential outside the beam similar to the Pierce diode problem discussed in Section 4.2.3.

Unfortunately, this inverse problem has not been solved for arbitrary forms of the axial potential and remains as a challenge for future work. The precise electrode structure in the transition region is therefore unknown. Nevertheless, we will make use of a semi-analytic technique to obtain approximate beam injection matching solutions. We outline it as follows:

1. Construct a trial electrode geometry G^{t1} that joins an accelerating-beam Child-Langmuir region (as in Chapter 4) to a coasting beam region (Chapter 5). Construct the associated trial functions for the electrostatic potentials $\bar{\Phi}_{00}^{t1}(\bar{z})$ and $\bar{\Phi}_Q^{t1}(\bar{z})$ that adhere to the limiting forms [i.e., the Child-Langmuir form on one side of the transition region and a constant on the other for $\bar{\Phi}_{00}^{t1}(\bar{z})$, and zero on one side of the transition region and a constant on the other for $\bar{\Phi}_Q^{t1}(\bar{z})$] and transition between them smoothly. The superscript “t1” indicates that these are “first-guess” trial functions.
2. Using the trial functions $\bar{\Phi}_{00}^{t1}(\bar{z})$ and $\bar{\Phi}_Q^{t1}(\bar{z})$ in Eqs. (6.3) and (6.7), compute the applied quadrupole and non-axisymmetric PPM magnetic fields $\bar{B}_Q^{t1}(\bar{z})$ and $\bar{B}_0^{t1}(\bar{z})$ required for beam matching.

3. (Optional) Given the electrostatic potentials $\overline{\Phi}_{00}^{t1}(\bar{z})$ and $\overline{\Phi}_Q^{t1}(\bar{z})$, the magnetic fields $\overline{B}_Q^{t1}(\bar{z})$ and $\overline{B}_0^{t1}(\bar{z})$, and the initial conditions for the beam at the emitter (parallel flow, negligible emittance, zero twist angle, beam semi-axes given by the elliptic cathode size), we integrate the envelope quantities forward through the diode and beam tunnel using Eq. (2.104) to verify that they adhere to the desired beam behavior. Numerical optimization may be performed at this stage through the introduction of additional parameters in the representation of the applied magnetic fields. For simplicity in the present discussion, we have introduced only a single parameter; namely, the axial magnetic field phase shift $\varphi(z) = \varphi_0 = \text{const}$.
4. The applied magnetic fields $\overline{B}_Q^{t1}(\bar{z})$ and $\overline{B}_0^{t1}(\bar{z})$ (or their optimized versions from Step 3) are applied to the trial electrode geometry G^{t1} in a numerical simulation routine such as the 3D OMNITRAK code. Both the particle trajectories and the electrostatic potentials are computed self-consistently with the specified electrode geometry G^{t1} , including the effects of the anode hole and the applied magnetic fields $\overline{B}_Q^{t1}(\bar{z})$ and $\overline{B}_0^{t1}(\bar{z})$. We use the results of the simulation to obtain an improved estimate of the electrostatic potentials on the beam axis and denote them as $\overline{\Phi}_{00}^{t2}(\bar{z})$ and $\overline{\Phi}_Q^{t2}(\bar{z})$.
5. If the “t2” potentials $\overline{\Phi}_{00}^{t2}(\bar{z})$ and $\overline{\Phi}_Q^{t2}(\bar{z})$ are sufficiently similar to the “t1” potentials $\overline{\Phi}_{00}^{t1}(\bar{z})$ and $\overline{\Phi}_Q^{t1}(\bar{z})$, we conclude that we have obtained a self-consistent solution to the matched beam through the transition region. If the potentials are significantly different (the specific criterion depends on the application at hand and the beam quality desired), we may proceed iteratively in order to approach a solution by returning to Step 2 and using $\overline{\Phi}_{00}^{t2}(\bar{z})$ and $\overline{\Phi}_Q^{t2}(\bar{z})$ to computed an improved version of the applied magnetic fields $\overline{B}_Q^{t2}(\bar{z})$ and $\overline{B}_0^{t2}(\bar{z})$.

The semi-analytic technique outlined above should be contrasted with the conventional approach to the beam matching problem which requires iterative modifications and optimizations of a 3D electrode geometry, i.e., ($G^{t1} \rightarrow G^{t2} \rightarrow G^{t3} \rightarrow \dots G^{tn}$). The conventional approach amounts to a high-dimensional optimization process which relies on a computationally-intensive simulation routine to evaluate the merit of each modification. Such a process quickly approaches the limits of what can be achieved in a reasonable computation time.

The conventional approach does have occasional utility, since it is the only way a particularly desired electrostatic potential can be achieved. Moreover, if large nonparaxial effects are observed in a simulation, electrode geometry modifications may

be necessary in order to eliminate them, which may require one or two simulation runs. However, once it has been established that a particular electrode geometry supports a paraxial field distribution, no geometry modifications are necessary in the semi-analytic solution method outlined above. Because the geometry is held fixed in the iterative scheme, and because the numerical optimization occurs over a directly integrable equation (not a computationally intensive 3D simulation), the semi-analytic process converges extremely quickly. Indeed, in the next section, we apply this technique to obtain a satisfactory solution after only two iterations.

6.2.4 6:1 Elliptic Beam Matching Example

Let us consider the matching of a 6:1 elliptic electron beam of constant envelope semi-axes $a_{\text{des}} = 0.373$ cm and $b_{\text{des}} = 0.062$ cm propagating with current $I = 0.11$ A. The beam is emitted from a space-charge-limited, parallel-flow, elliptic electron diode with diode length $d = 0.411$ cm and cathode potential $\Phi_{00}(0) = -2290$ V (see discussions in Section 4.4.4). It is injected into a grounded, rectangular beam tunnel of width 10.74 mm and height 7.0 mm. We choose a longitudinal magnetic period of length $S = 1.0$ cm and a reference length of $\lambda = b_{\text{des}}$. In the following, we apply the semi-analytic beam matching technique discussed in Section 6.2.3.

The diode electrode geometry is that discussed in Section 4.4.4.1 while the beam tunnel geometry is that discussed in Section 5.7.1. The two regions are connected by adding a quasi-elliptical aperture to the anode in order to extract the beam (see later in Figure 6.5). The axial electrostatic potential $\Phi_{00}(z)$ then smoothly varies from the Child-Langmuir form near the cathode to a constant value of $\Phi_{00} \cong -70$ V in the beam tunnel, which is obtained from the OMNITRAK simulation results presented in Section 5.7.1. Here, $\Phi_{00} \cong -70$ is the voltage depression at the beam axis due to space charge.

We construct a trial function Φ_{00}^{t1} for the axial potential which varies smoothly between the Child-Langmuir and constant behavior. Because this process converges so rapidly, the results which follow are largely independent of the trial function chosen. In fact, one simple way of obtaining a trial function is simply to perform an OMNITRAK simulation without any applied magnetic fields in the transition region. The beam will likely lose confinement or undergo large envelope oscillations, but we can extract the axial potential information from the OMNITRAK simulation, regardless.

The electrostatic quadrupole potential $\Phi_Q(z)$ is zero in both the Child-Langmuir limit of Section 4.4.4.1 and the coasting beam limit of Section 5.7.1, therefore we choose a vanishing trial function $\Phi_Q^{\text{t1}} = 0$.

Adopting the trial functions Φ_{00}^{t1} and Φ_Q^{t1} and making use of Eqs. (6.3) and (6.7), we obtain the applied magnetic fields B_0^{t1} and B_Q^{t1} .

Employing the applied magnetic fields B_0^{t1} and B_Q^{t1} [with $\phi(z) = 0$, by default] in an OMNITRAK simulation of the beam system, we obtain a refined measurement of the on-axis electrostatic potential $\Phi_{00}^{t2}(z)$, as shown in Figure 6.1. The refined measurement of the quadrupole electrostatic potential $\Phi_Q^{t2}(z)$ is zero, to within the numerical error of the simulation.

Adopting the trial functions Φ_{00}^{t2} and Φ_Q^{t2} and making use of Eqs. (6.3) and (6.7), we obtain the updated applied magnetic fields B_0^{t2} and B_Q^{t2} .

Given the electrostatic potentials Φ_{00}^{t2} and Φ_Q^{t2} , the magnetic fields B_0^{t2} and B_Q^{t2} , and the initial conditions for the beam at the emitter (parallel flow, negligible emittance, zero twist angle, beam envelope semi-axes given by the elliptic cathode size), we integrate the envelope quantities forward through the diode and beam tunnel using Eq. (2.104). Performing a simple 1D optimization, we choose a value for the phase shift of $\phi(z) = \phi_0 = -0.16$ rad in order to minimize envelope oscillations.

In Figure 6.2, we show a plot of the beam envelope semi-axes a and b of the 6:1 elliptic beam over four longitudinal magnetic periods ($4S = 4.0$ cm), though the diode and beam tunnel. Note that the envelopes are not exactly constant, which is largely attributable to the fact that the condition $S \ll S_{des}$ is not strictly satisfied, as both lengths are of the same order (1 cm). This limitation can be overcome by the inclusion of additional parameters in the applied field description. Naturally, this complicates the optimization process, but is still vastly simpler (and more computationally tractable) than optimizing a 3D geometry. For the present didactic purposes, we utilize only the single parameter optimization over the phase shift $\phi(z) = \phi_0$ of the axial magnetic field.

The optimized applied magnetic fields B_0^{t2} and B_Q^{t2} [with $\phi(z) = \phi_0 = -0.16$ rad], are plotted in Figure 6.3 and Figure 6.4, respectively. Note that the magnetic fields achieve their largest values in the vicinity of the anode hole at $z = 0.411$ cm, where they must counteract the defocusing electrostatic forces near the anode hole.

We employ the applied magnetic fields B_0^{t2} and B_Q^{t2} [with $\phi(z) = \phi_0 = -0.16$ rad] in the second-iteration OMNITRAK simulation of the beam system. Particles are emitted from a space-charge-limited diode and tracked over four axial magnetic periods ($4S = 4.0$ cm). The resulting particle trajectories and electrostatic equipotentials are shown in the plane $(y - z)$ in Figure 6.5 and in the plane $(x - z)$ in Figure 6.6. A 3D perspective view of the simulation region and trajectories (with the anode and beam tunnel not shown, for illustrative purposes) is shown in Figure 6.7. It is apparent from

the simulation results that the beam is well confined and the beam envelope semi-axes are nearly constant.

The beam behavior shown in Figure 6.7 is quite remarkable considering that extensive 3D optimization has not been performed. Only two iterations and a simple one-parameter optimization of a directly integrable equation are necessary in order to produce this result.

We also note that this beam injection matching technique may be used with the positions of the coasting region and accelerating regions reversed in order to design a high-efficiency, single-stage depressed collector. The collector electrode (essentially, a mirror image diode) is held at a potential negative with respect to the beam tunnel (for electrons), thereby a high-quality, laminar charged-particle beam is focused while it is decelerated such that it impinges on the collection electrode with nearly zero velocity. Much of the beam kinetic energy can thereby be recovered in the form of a current that can be used to drive a load, including, perhaps the current used to drive the beam formation diode, itself. Such a depressed collector reduces the input energy required to operate a beam device, increasing its efficiency.

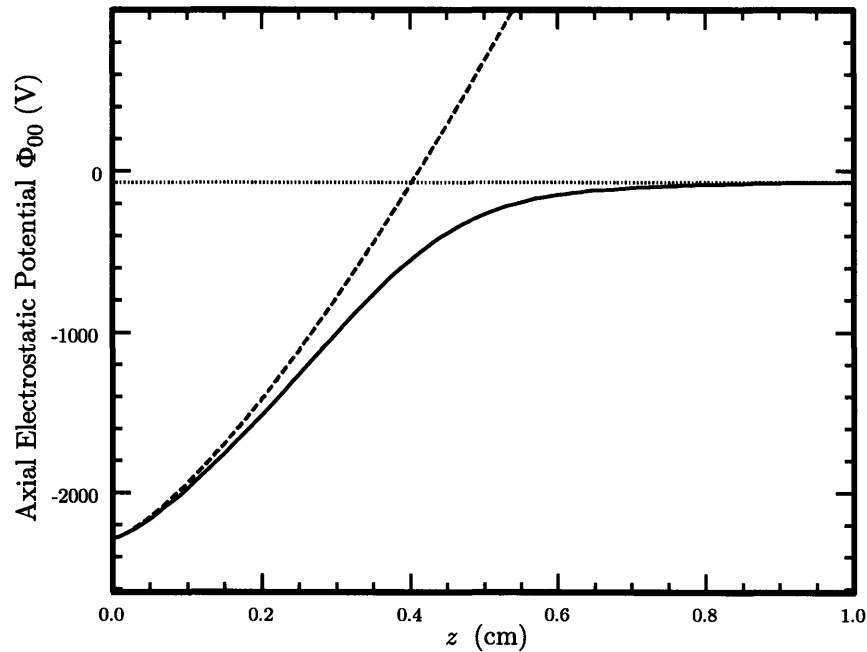


Figure 6.1: Plots of the on-axis electrostatic potential $\Phi_{00}^{t2}(z)$ (solid curve), the Child-Langmuir potential $\Phi \propto z^{4/3}$ (dashed curve), and the depressed potential limit $\Phi_{00}^{t2} \cong -70$ V (dotted line) versus the axial coordinate z in the second iteration of the 6:1 elliptic beam matching calculations.

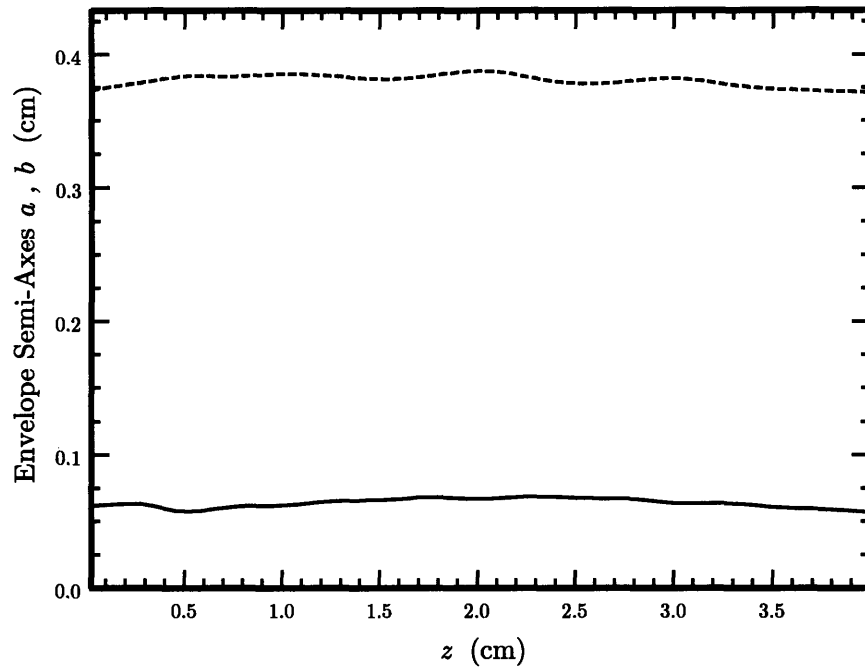


Figure 6.2: Beam envelope semi-major axis a and semi-minor axis b of the 6:1 elliptic beam over four longitudinal magnetic periods, $4S = 4.0$ cm.

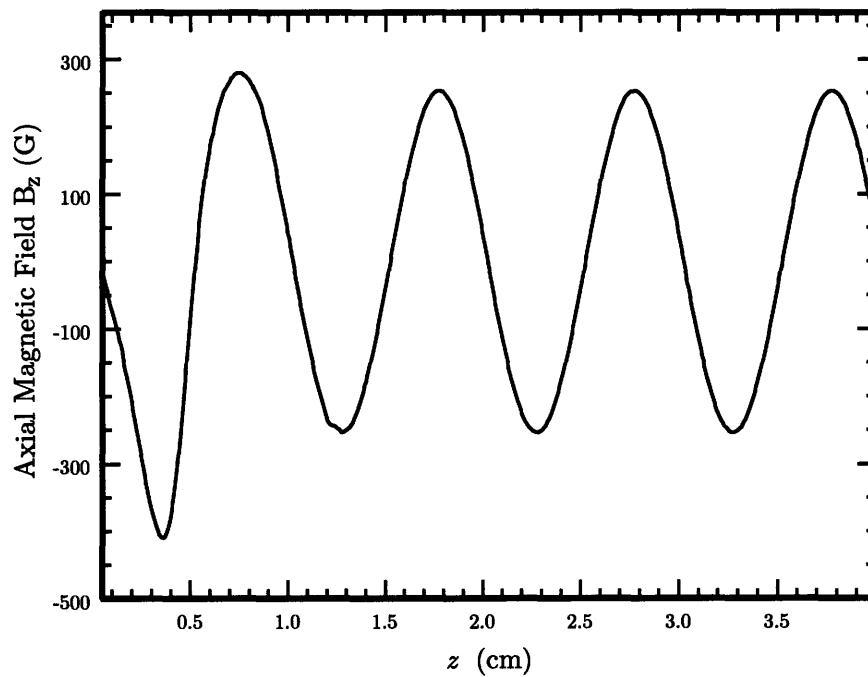


Figure 6.3: Plot of the axial magnetic field $B_z(z) = B_0^{t^2}(z)\sin(-0.16 + 2\pi z/S)$ versus the axial coordinate z over four periods, $4S = 4.0$ cm.

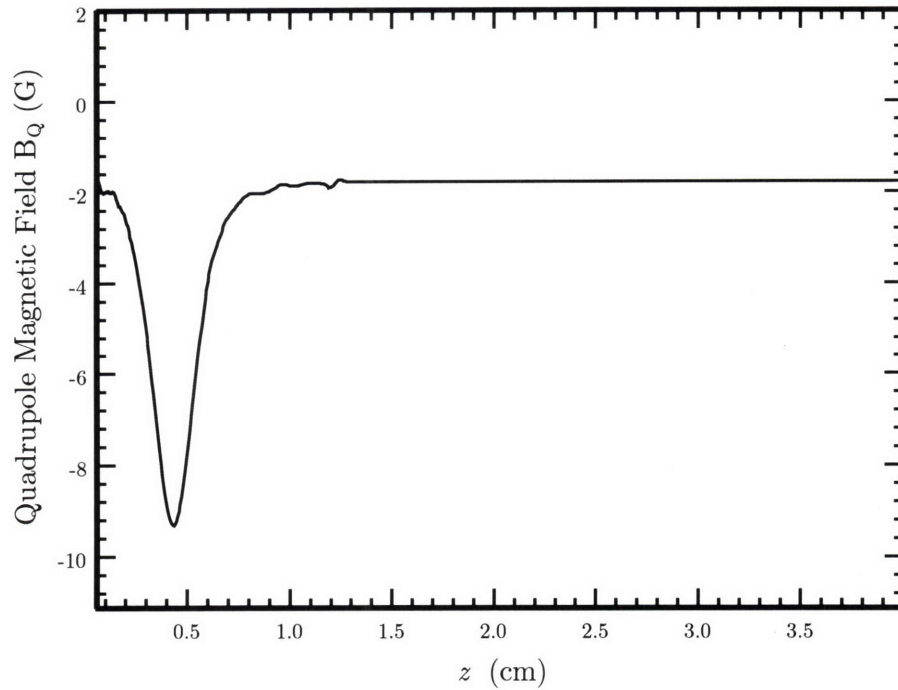


Figure 6.4: Plot of the quadrupole magnetic field $B_Q(z) = B_Q^{12}(z)$ versus the axial coordinate z over four axial magnetic periods, $4S = 4.0$ cm.

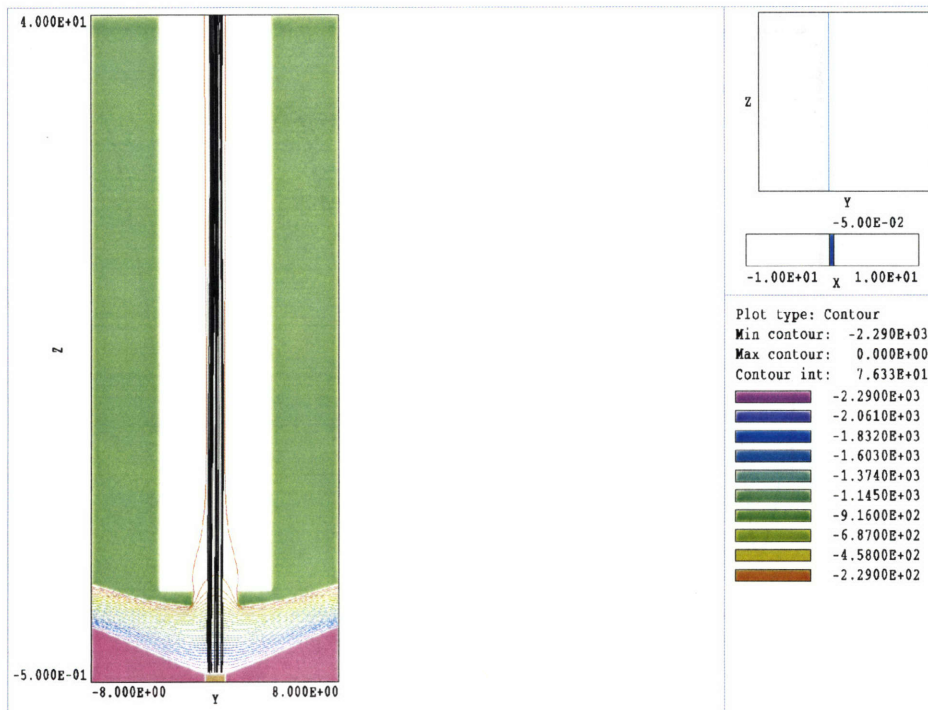


Figure 6.5: Projection onto the plane $(y-z)$ of particle trajectories over four axial magnetic periods ($4S = 4.0$ cm) in the 3D OMNITRAK simulation.

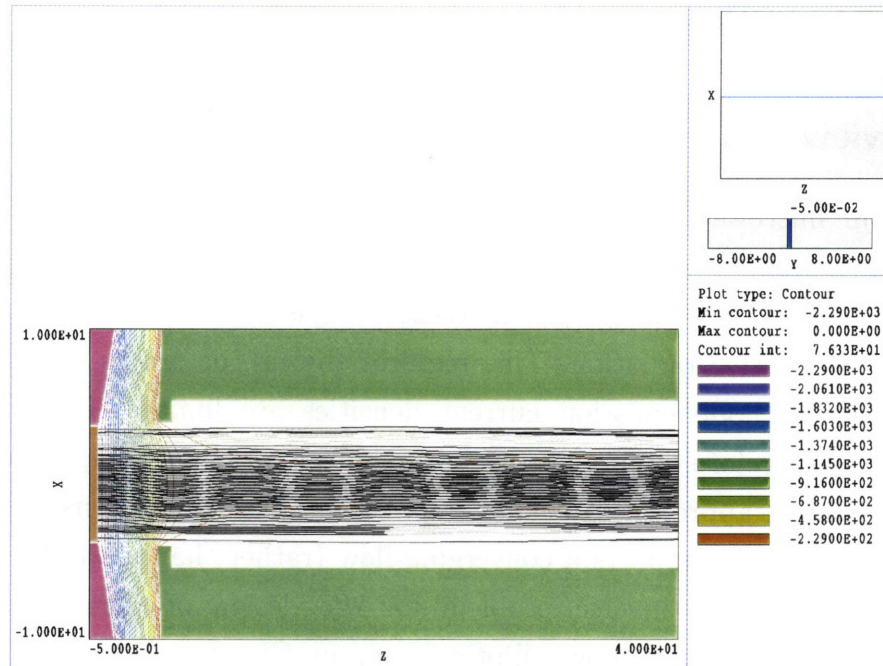


Figure 6.6: Projection onto the plane $(x - z)$ of particle trajectories over four axial magnetic periods ($4S = 4.0$ cm) in the 3D OMNITRAK simulation.

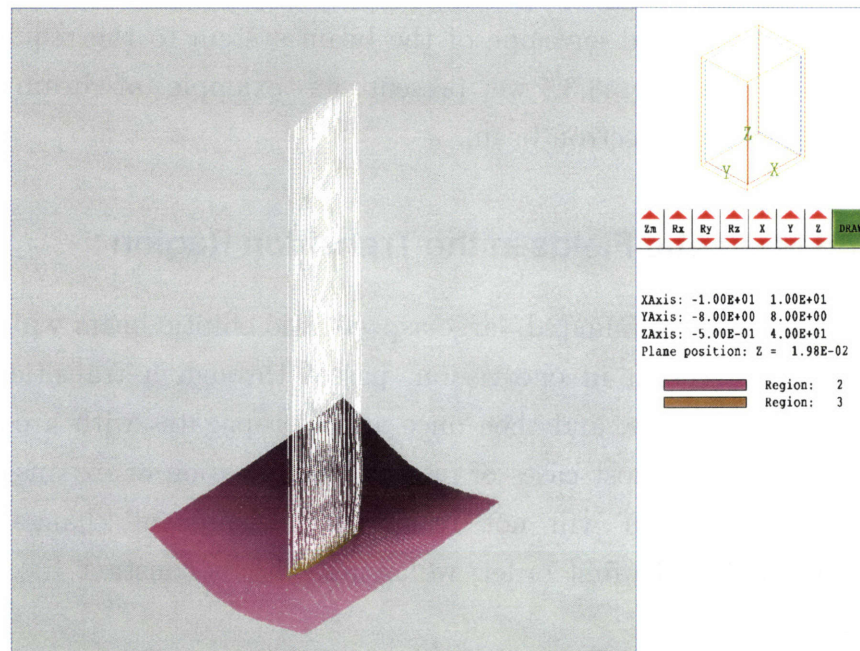


Figure 6.7: Perspective view of particle trajectories over four axial magnetic periods ($4S = 4.0$ cm) in the 3D OMNITRAK simulation. Note that the anode and beam tunnel, though present in the simulation, are not shown so that the beam can be viewed clearly.

6.3 Beam Compression

6.3.1 Overview

Beam tunnels in microwave devices are often limited in size in order to prevent the propagation of undesired electromagnetic modes. At the same time, high current charged-particle beams must propagate in these tunnels in order to produce significant power levels of microwave radiation. This requires the use of beams with high current densities, however cathode emission current densities are limited. Beam systems for microwave devices therefore often make use of some form of beam compression.

The conventional approach to beam compression relies on the construction of a set of diode electrodes which supports a converging-flow (rather than a parallel-flow) beam. While we have solved the inverse problem for the design of electrodes which self-consistently support a parallel-flow elliptic beam in Chapter 4, no such solution is known for a converging-flow elliptic beam. This remains a topic for future work in this area.

An alternative to electrostatic compression in the diode is magnetic compression of a coasting beam, which we present here. In Section 6.3.2, we use the methods of Chapter 3 to relate the desired envelope of the beam system to the required confining magnetic fields. In Section 6.3.3, we present an example of beam compression calculations for a 6:1 elliptic electron beam.

6.3.2 Applied Magnetic Fields in the Transition Region

We consider a space-charge-dominated, large-aspect-ratio elliptic beam which propagates with a constant cross-section in one region, passes through a transitional region in which its cross-section changes, and then once again propagates with a constant cross-section in a third region. In most cases of interest, compression or expansion of a beam through the transition region will not result in a significant change in its axial electrostatic potential $\bar{\Phi}_{00}$. To first order, we assume $\bar{\Phi}_{00}$ is constant (i.e., the coasting beam approximation).

Outside the transition region, we have already inverted the problem to determine the appropriate applied fields and electrode geometries (see Chapter 5). Because we assume a space-charge-dominated beam, emittance effects are negligible [16] [27] [28] and the beam takes a cold-fluid form in which fluid elements follow single particle trajectories in the transition region. If the transition occurs over a characteristic scale

length \bar{S}_{des} (see Section 3.1), we can use the methods in Chapter 3 to model the beam behavior in the transition region. Moreover, if we assume the beam is non-twisting with $|\theta| \ll 1$ and specify the desired beam envelope semi-axes $\bar{a}_{\text{des}}(\bar{z})$ and $\bar{b}_{\text{des}}(\bar{z})$, the fluid element trajectories will be self-similar, i.e.,

$$\frac{\bar{x}(\bar{z})}{\bar{x}(\bar{z}_0)} = \frac{\bar{a}_{\text{des}}(\bar{z})}{\bar{a}_{\text{des}}(\bar{z}_0)}, \quad (6.8)$$

$$\frac{\bar{y}(\bar{z})}{\bar{y}(\bar{z}_0)} = \frac{\bar{b}_{\text{des}}(\bar{z})}{\bar{b}_{\text{des}}(\bar{z}_0)}. \quad (6.9)$$

Since the beam propagation solutions obtained on either side of the transition region are obtained in the *small residual quadrupole field* regime in Section 3.4.7, we search for a solution in the transition region which is also in this regime. Under such circumstances, Eq. (3.66) implies

$$\frac{d\bar{p}_y}{d\bar{z}} - \frac{\alpha_\lambda \bar{y}}{\beta} \left(\frac{4\bar{I}}{\bar{a}\bar{b}\beta\gamma^2} - \frac{\alpha_\lambda}{\gamma} \bar{B}_z^2 \right) \sim \mathcal{O} \left(\frac{1}{\bar{S}_{\text{des}}^2} \left[\bar{b}\gamma\beta + \frac{\bar{a}^2}{\bar{b}}\beta\gamma \right] \right). \quad (6.10)$$

We take an axial magnetic field of the form

$$\bar{B}_z(\bar{z}) = \bar{B}_0(\bar{z}) \sin \left(\frac{2\pi\bar{z}}{\bar{S}} + \phi(\bar{z}) \right), \quad (6.11)$$

where $\phi(\bar{z})$ is a parameter that represents a slowly-varying phase shift of the axial magnetic field, and the amplitude \bar{B}_0 varies slowly on the length scale \bar{S}_{des} with $\bar{S} \ll \bar{S}_{\text{des}}$. If we now perform a *local average* of Eq. (6.10) over the magnetic oscillation wavelength \bar{S} , we find

$$\left\langle \frac{d\bar{p}_y}{d\bar{z}} \right\rangle - \frac{\alpha_\lambda \bar{y}}{\beta} \left(\frac{4\bar{I}}{\bar{a}\bar{b}\beta\gamma^2} - \frac{\alpha_\lambda}{\gamma} \frac{\bar{B}_0^2}{2} \right) \sim \mathcal{O} \left(\frac{1}{\bar{S}_{\text{des}}^2} \left\langle \bar{b}\gamma\beta + \frac{\bar{a}^2}{\bar{b}}\beta\gamma \right\rangle \right). \quad (6.12)$$

where the angle brackets denote the *local average*. Equation (6.12) is satisfied by choosing

$$\bar{B}_0^2 \cong \frac{8\bar{I}}{\bar{a}\bar{b}\alpha_\lambda\beta\gamma} - \frac{2\gamma\beta}{\alpha_\lambda^2 \bar{y}} \left\langle \frac{d\bar{p}_y}{d\bar{z}} \right\rangle, \quad (6.13)$$

which can be expressed using Eqs. (3.39) and (6.9) as

$$\bar{B}_0^2 \cong \frac{8\bar{I}}{\bar{a}\bar{b}\alpha_\lambda\beta\gamma} - \frac{2\gamma^2\beta^2}{\alpha_\lambda^2\bar{b}_{des}} \frac{d^2\bar{b}_{des}}{d\bar{z}^2}. \quad (6.14)$$

Equation (6.14) specifies the form of the matched axial magnetic field \bar{B}_z in the transition region in terms of the desired beam envelope semi-minor axis $\bar{b}_{des}(\bar{z})$.

Similarly, we obtain the quadrupole magnetic field \bar{B}_Q using Eqs. (3.17) and (3.18) in the limit $\theta \rightarrow 0$, which yields

$$\frac{d\bar{p}_x^Q}{d\bar{z}} \cong -\alpha_\lambda\bar{x} \left(\bar{B}_Q + \frac{2}{\beta}\bar{\Phi}_Q - \frac{4\bar{I}}{\bar{a}(\bar{a} + \bar{b})\beta^2\gamma^2} \right). \quad (6.15)$$

Performing a *local average* of Eq. (6.15) over the magnetic oscillation wavelength \bar{S} , we find

$$\gamma\beta \frac{d^2\bar{x}_{des}}{d\bar{z}^2} \cong -\alpha_\lambda\bar{x} \left(\bar{B}_Q + \frac{2}{\beta}\bar{\Phi}_Q - \frac{4\bar{I}}{\bar{a}(\bar{a} + \bar{b})\beta^2\gamma^2} \right), \quad (6.16)$$

which implies, through Eq. (6.8),

$$\bar{B}_Q \cong \frac{4\bar{I}}{\bar{a}(\bar{a} + \bar{b})\beta^2\gamma^2} - \frac{2}{\beta}\bar{\Phi}_Q - \frac{\gamma\beta}{\alpha_\lambda\bar{a}} \frac{d^2\bar{a}_{des}}{d\bar{z}^2}. \quad (6.17)$$

Equation (6.17) specifies the form of the matched quadrupole magnetic field \bar{B}_Q in the transition region in terms of the desired beam envelope semi-major axis $\bar{a}_{des}(\bar{z})$ and the electrostatic quadrupole potential $\bar{\Phi}_Q$.

6.3.3 6:1 Elliptic Beam Compression Example

Let us consider an elliptic electron beam with current $I = 0.11\text{A}$ and axial velocity $v_z = 0.094c$ propagating through a grounded, rectangular beam tunnel of width 10.74 mm and height 7.0 mm. In this example, the external quadrupole electrostatic potential vanishes, i.e., $\bar{\Phi}_Q = 0$. Choosing a reference length $\lambda = 0.062\text{cm}$, we ask the beam envelope semi-axes to take the forms

$$\bar{a}_{des}(\bar{z}) = \bar{a}_f \left[\frac{3}{2} - \frac{1}{2} \tanh\left(\frac{\bar{z}}{v\bar{S}} - 3\right) \right], \quad (6.18)$$

$$\bar{b}_{des}(\bar{z}) = \bar{b}_f \left[\frac{3}{2} - \frac{1}{2} \tanh\left(\frac{\bar{z}}{v\bar{S}} - 3\right) \right], \quad (6.19)$$

where the final beam envelope semi-axes are $a_f = \lambda \bar{a}_f = 0.187$ cm and $b_f = \lambda \bar{b}_f = 0.031$ cm, and we choose a longitudinal magnetic period of length $S = \lambda \bar{S} = 1$ cm and a steepness parameter $\nu = 1.5$.

Making use of Eqs. (6.18) and (6.19), the desired beam envelope semi-axes $a_{\text{des}}(z)$ and $b_{\text{des}}(z)$ are plotted in Figure 6.8 as solid curves and correspond to beam compression by a factor of two in each transverse dimension through the transition region, i.e., an area compression ratio of 4:1. Note that we could equally well choose different compression factors in each dimension simply by choosing different parameters in Eqs. (6.18) and (6.19).

We can obtain expressions for the applied magnetic fields in the transition region by using Eqs. (6.18) and (6.19) in Eqs. (6.14) and (6.17), yielding

$$\bar{B}_0^2(\bar{z}) \cong \frac{8\bar{I}}{\bar{a}\bar{b}\alpha_s\beta\gamma} - \frac{2\beta^2\gamma^2}{\alpha_s^2\nu^2\bar{S}^2} \frac{\tanh\left(\frac{\bar{z}}{\nu\bar{S}} - 3\right) \text{sech}^2\left(\frac{\bar{z}}{\nu\bar{S}} - 3\right)}{\frac{3}{2} - \frac{1}{2} \tanh\left(\frac{\bar{z}}{\nu\bar{S}} - 3\right)}, \quad (6.20)$$

$$\bar{B}_Q \cong \frac{4\bar{I}}{\bar{a}(\bar{a} + \bar{b})\beta^2\gamma^2} - \frac{\gamma\beta}{\alpha_s\nu^2\bar{S}^2} \frac{\tanh\left(\frac{\bar{z}}{\nu\bar{S}} - 3\right) \text{sech}^2\left(\frac{\bar{z}}{\nu\bar{S}} - 3\right)}{\frac{3}{2} - \frac{1}{2} \tanh\left(\frac{\bar{z}}{\nu\bar{S}} - 3\right)}. \quad (6.21)$$

We make use of Eqs. (6.20) and (6.21) to plot the applied magnetic fields B_z and B_Q over 10 axial magnetic periods (10 cm) in Figure 6.9 and Figure 6.10, respectively. Note that in determining the axial magnetic field in Figure 6.9, we have not performed any optimization over the phase shift parameter φ ; we have simply used its default value of $\varphi = 0$.

Given the applied magnetic fields of Figure 6.9 and Figure 6.10 and the entrance conditions for the beam [parallel flow, negligible emittance, zero twist angle, semi-axes given by Eqs. (6.18) and (6.19)], we can integrate the envelope trajectories forward through the beam tunnel using Eq. (2.104). In Figure 6.8, overlaid with the desired semi-axes $a_{\text{des}}(z)$ and $b_{\text{des}}(z)$ (solid curves), we have plotted the integrated semi-axes $a(z)$ and $b(z)$ (dashed curves) of the 6:1 electron beam over ten longitudinal magnetic periods (10 cm). Note that while we see some mismatch oscillation, the overall behavior

is as expected. Further numerical optimization can certainly be performed to decrease the oscillation amplitude.

We employ the applied magnetic fields Figure 6.9 and Figure 6.10 in an OMNITRAK simulation of the beam system. Particles enter the simulation region with the prescribed initial conditions [parallel flow, negligible emittance, zero twist angle, semi-axes given by Eqs. (6.18) and (6.19)] and are tracked over 10 axial magnetic periods (10 cm). The resulting particle trajectories and electrostatic equipotentials are shown in the plane $(y-z)$ in Figure 6.11 and in the plane $(x-z)$ in Figure 6.12. A 3D perspective view of the simulation region and trajectories (with the beam tunnel suppressed, for illustrative purposes) is shown in Figure 6.13. It is apparent from the simulation results that the beam behavior is consistent with the envelope code results, showing beam compression in both transverse dimensions and the residual mismatch oscillations.

We note that this beam compression technique can also be reversed to accomplish beam expansion, such as may be needed in a collector in order to reduce the beam power density deposited on a collection surface.

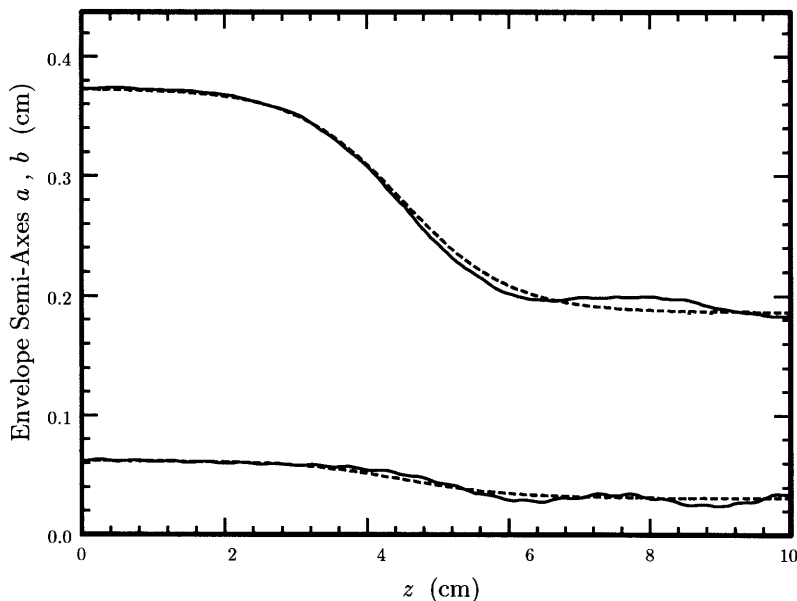


Figure 6.8: Shown in solid curves are the desired beam envelope semi-major and semi-minor axes $a_{\text{des}}(z)$ and $b_{\text{des}}(z)$ of the 6:1 electron beam plotted as the beam undergoes compression by a factor of two in each dimension over 10 longitudinal magnetic periods. The dashed curves correspond to the beam envelope semi-major and semi-minor axes $a(z)$ and $b(z)$ computed using the applied magnetic fields in Figure 6.9 and Figure 6.10.

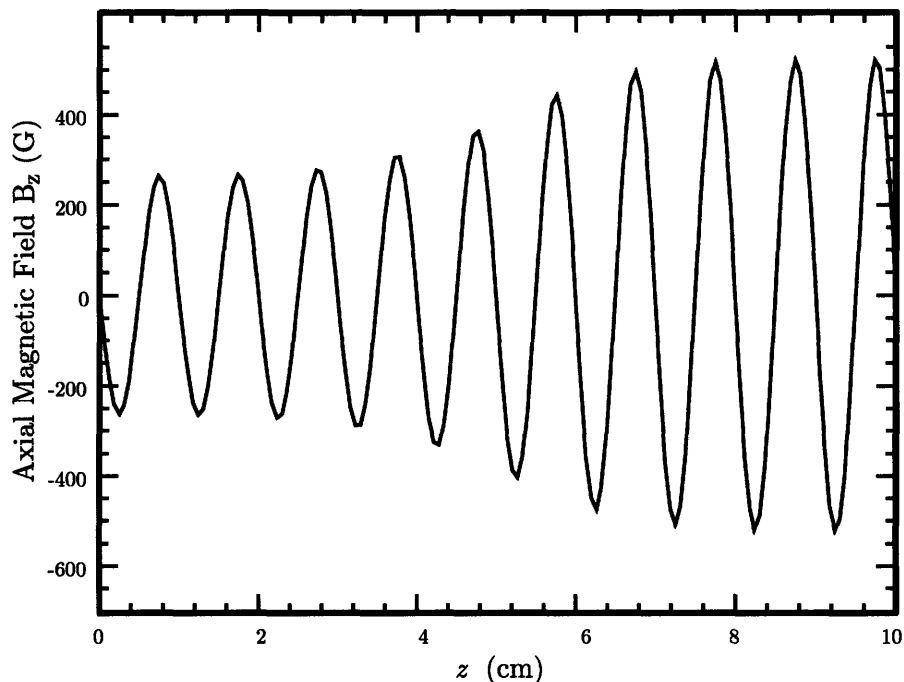


Figure 6.9: Plot of the axial magnetic field $B_z(z) = B_0(z)\sin(2\pi z/S)$ versus the axial coordinate z over ten periods (10 cm). The magnetic envelope function $B_0(z)$ is obtained from Eq. (6.20).

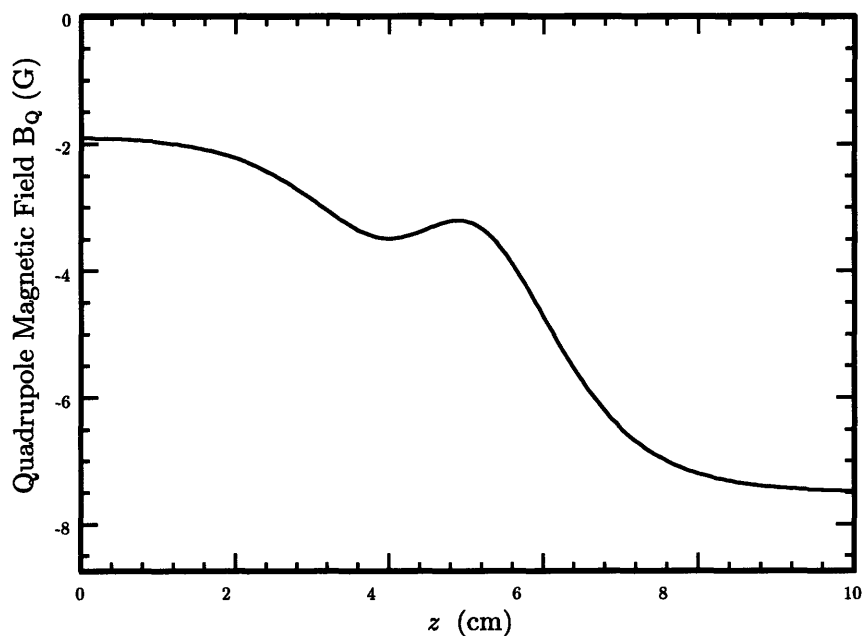


Figure 6.10: Plot of the quadrupole magnetic field $B_Q(z)$ versus the axial coordinate z over ten axial magnetic periods (10 cm). The quadrupole magnetic field $B_Q(z)$ is obtained from Eq. (6.21).

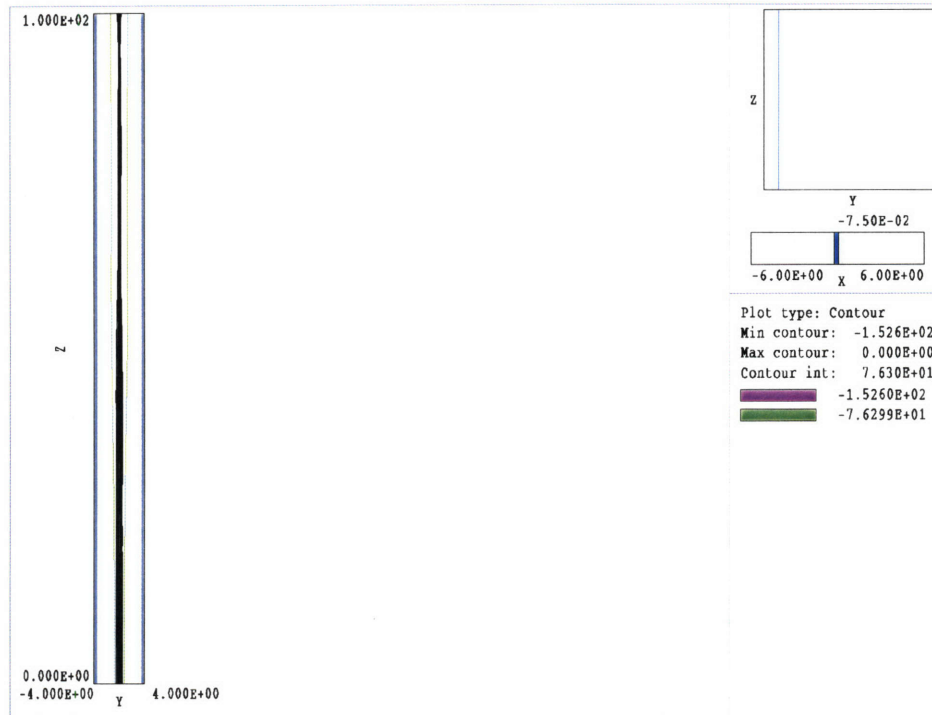


Figure 6.11: Particle trajectories are tracked over 10 axial magnetic periods (10 cm) using the 3D trajectory code OMNITRAK and projected onto the plane ($y - z$).

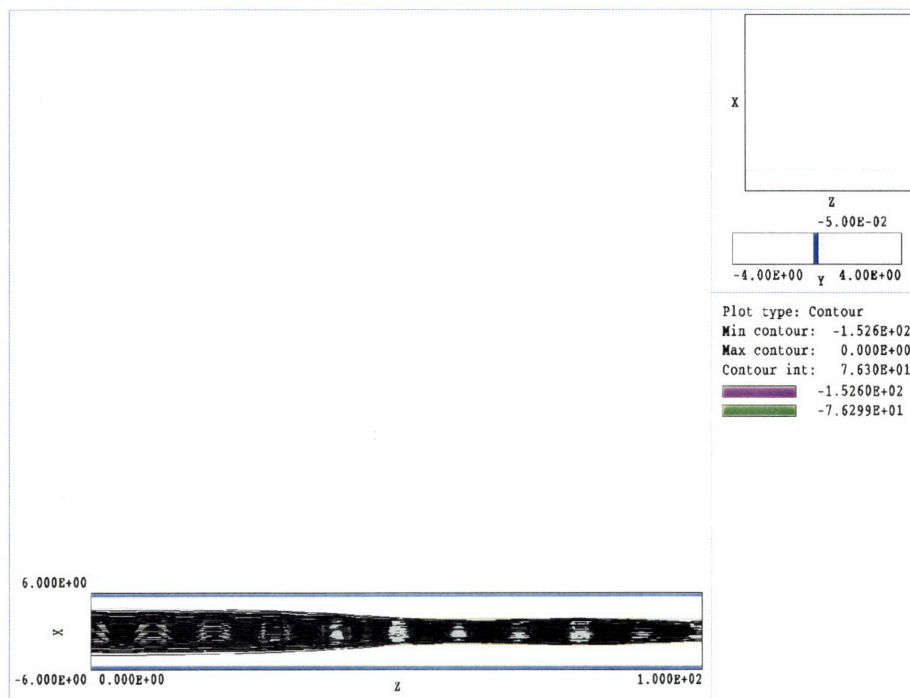


Figure 6.12: Particle trajectories are tracked over 10 axial magnetic periods (10 cm) using the 3D trajectory code OMNITRAK and projected onto the plane ($x - z$).

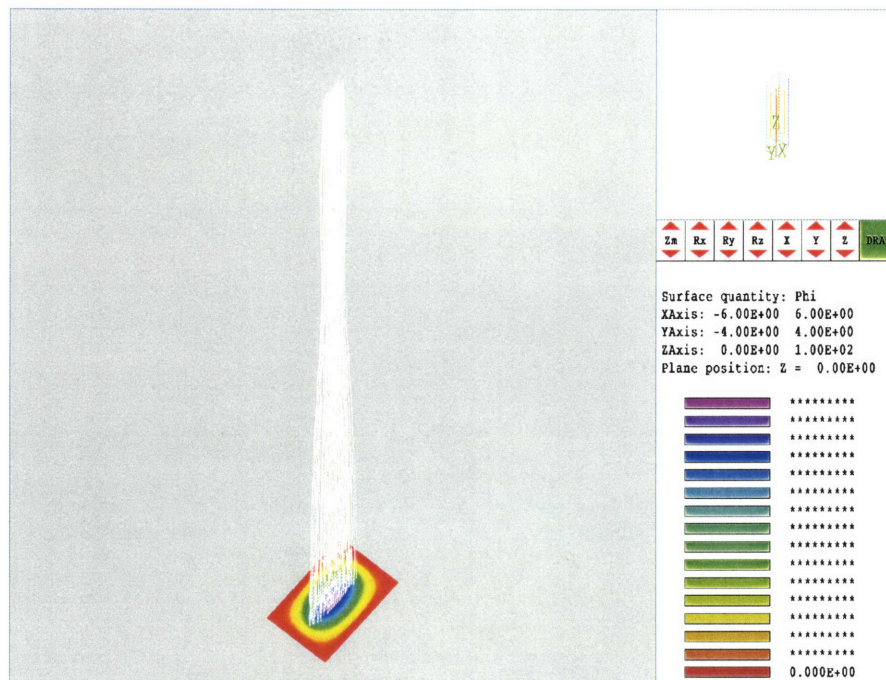


Figure 6.13: Perspective view of particle trajectories tracked over 10 axial magnetic periods (10 cm) using the 3D trajectory code OMNITRAK. The beam tunnel, though present in the simulation, is suppressed so that the beam can be viewed clearly.

7 Conclusion

In this thesis, we have attempted to provide a new perspective on elliptic charged-particle beam problems. We presented, in Chapter 2, a unified paraxial model of steady-state elliptic charged-particle beams, bridging the existing gap between the accelerating-beam Child-Langmuir [29] theory and numerous models of coasting beam dynamics. We describe the evolution of the elliptic beam particle distribution function through the matrix differential equation (2.104). In later chapters, as we integrate Eq. (2.104) to determine the evolution of the elliptic beam for several examples, we find results consistent with those produced by the much more numerically intensive 3D simulation code OMNITRAK [38].

We have also emphasized the analytic inverse approach to charged-particle beam problems in this thesis. In Chapter 3, we were able to use this approach to analyze single-particle behavior in elliptic beams, obtaining constraints on the applied fields in various regimes (as identified in Section 3.4), each corresponding to different components of a beam system: the beam-forming diode, the transitional matching section, and the coasting beam transport lattice.

Similarly, in Chapter 4, we obtained a novel relativistic generalization of paraxial, elliptic beam Child-Langmuir [29] flow in Eq. (4.3). Taking the nonrelativistic limit, we were able to solve the inverse problem analytically, obtaining Eq. (4.33) for the external equipotentials (i.e., electrode surfaces) consistent with Child-Langmuir [29] beams of elliptic cross-section. In Section 4.4, we showed that 3D OMNITRAK [38] simulations incorporating the analytically-specified electrode surfaces robustly produce near-ideal beams, providing independent confirmation of the theory.

In Chapter 5, we used a perturbative approach to solve an inverse problem determining the applied fields and entrance conditions that self-consistently support a parallel-flow, coasting, space-charge-dominated, large aspect-ratio elliptic beam. Numerical integrations of the beam distribution using Eq. (2.104) and OMNITRAK [38] simulations both confirm the analytic solution.

Finally, in Chapter 6, we presented semi-analytic inverse techniques to obtain the applied fields necessary in order to confine elliptic beams in transition regions. Examples were worked for a beam-matching situation between an elliptic beam diode and transport channel and for a compressing beam scenario. In each example, numerical integration of the beam distribution using Eq. (2.104) and OMNITRAK [38] simulations produced consistent results.

These results, taken together, suggest means of improving the quality and increasing our control of high-intensity elliptic charged-particle beams. We have discussed a few applications of these techniques for particle accelerators and microwave tubes, but there are a plethora of other potential applications, such as industrial processing and radiation therapy, which could stand to benefit from such improvements in beam systems. In general, we believe that the analytic inverse approach is a more rational approach to charged-particle beam problems than the traditional brute-force numeric techniques, particularly for 3D problems. While we harbor no pretensions that numeric techniques can be fully supplanted by analytic ones, we are confident that future work in this area will produce powerful new analytic-numeric hybrid algorithms that will enable finer control of higher-quality beams while providing new insights and opening new applications for their use.

Appendix

A Elliptic Projections

A.1 Overview

Equation (2.105) describes the 2D ellipse obtained when the 4D hyperellipsoid defined in Eq. (2.100) is projected into a 2D subspace (x_1, x_2) where $x_1, x_2 \in (x, y, p_x, p_y)$. In order to prove that Eq. (2.105) properly represents the projected ellipse, we begin with a geometric description of projection for a low-dimensional case in Appendix A.2. In Appendix A.3, we perform an analogous projection operation to obtain a 3D ellipsoid from a 4D hyperellipsoid, and in Appendix A.4, we perform another projection to reduce the 3D ellipsoid to a 2D ellipse.

A.2 1D Projection of the 2D Ellipse

We write the matrix equation for an ellipse in a 2D space (x_1, x_2) as

$$1 = \underline{\boldsymbol{\chi}}_{12}^T \cdot \underline{\mathbf{C}} \cdot \underline{\boldsymbol{\chi}}_{12}, \quad (\text{A.1})$$

where

$$\underline{\boldsymbol{\chi}}_{12} \equiv \begin{pmatrix} x_1 \\ x_2 \end{pmatrix}, \quad (\text{A.2})$$

and

$$\underline{\mathbf{C}} \equiv \begin{pmatrix} C_{11} & C_{12} \\ C_{12} & C_{22} \end{pmatrix}. \quad (\text{A.3})$$

We expand Eq. (A.1) as

$$1 = C_{11}x_1^2 + 2C_{12}x_1x_2 + C_{22}x_2^2. \quad (\text{A.4})$$

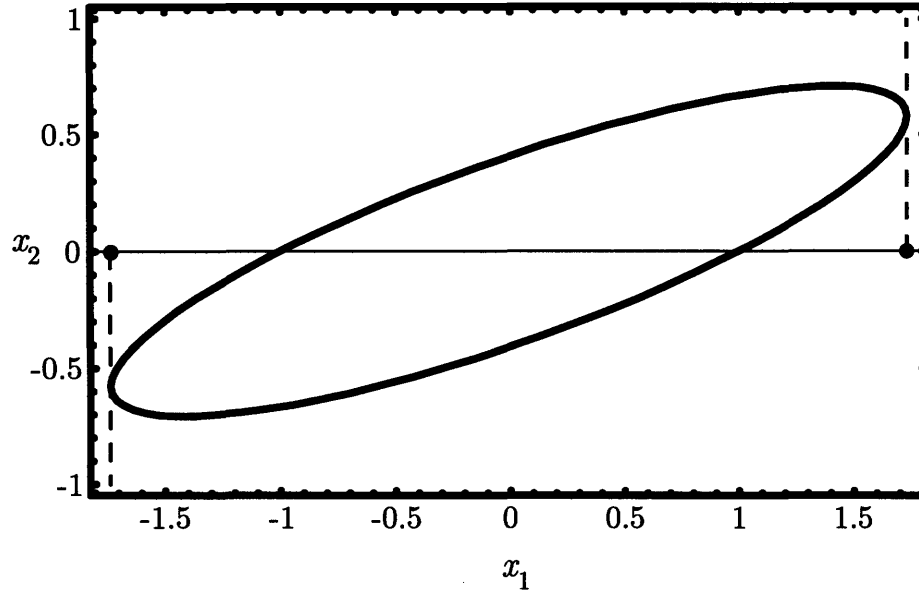


Figure A.1: The solid line corresponds to the 2D ellipse defined by Eq. (A.1) with $C_{11} = 1$, $C_{22} = 6$, and $C_{12} = -2$. The projection of this 2D ellipse onto the x_1 -axis is bounded by a 1D ellipse – the two points indicated by the filled circles at $(x_1, x_2) = (\pm\sqrt{3}, 0)$.

Let us illustrate the fact that Eq. (A.4) represents an ellipse by graphing it for the specific case of $C_{11} = 1$, $C_{22} = 6$, and $C_{12} = -2$ in Figure A.1. In Figure A.1, the solid curve describes the shape of the 2D ellipse defined by Eq. (A.4), while the dashed lines graphically project this 2D ellipse into the 1D subspace of x_1 . The 1D projection is bounded by a perpendicular projection of the extremal points of the 2D ellipse onto the x_1 -axis.

Just as a 2D ellipse is a curve which bounds a 2D area, a 1D ellipse is a pair of points which bounds a 1D line. The projection of the 2D ellipse defined by Eq. (A.4) into the subspace of x_1 is bounded by a 1D ellipse. In order to derive the equation for the 1D ellipse, we note that the extremal values of x_1 on the 2D ellipse are obtained where $dx_1/dx_2 = 0$, with the derivative being taken along the elliptic curve. Therefore, implicitly differentiating Eq. (A.4) to obtain

$$0 = 2C_{11}x_1dx_1 + 2C_{12}(x_1dx_2 + x_2dx_1) + 2C_{22}x_2dx_2, \quad (\text{A.5})$$

and setting $dx_1 = 0$ in Eq. (A.5), we obtain the equation for the extremal points on the 2D ellipse,

$$x_2 = -\frac{C_{12}}{C_{22}} x_1. \quad (\text{A.6})$$

Substituting Eq. (A.6) into Eq. (A.4), we find the equation for the 1D ellipse that bounds the projection of the 2D ellipse defined by Eq. (A.4) into in the x_1 subspace, i.e.,

$$x_1^2 = \left(C_{11} - \frac{C_{12}^2}{C_{22}} \right)^{-1}. \quad (\text{A.7})$$

With the example parameters of $C_{11} = 1$, $C_{22} = 6$, and $C_{12} = -2$, Eq. (A.7) implies that the points $x_1^2 = 3$ bound the 1D ellipse, as shown in Figure A.1.

A.3 3D Projection of the 4D Hyperellipsoid

By analogy to the 2D to 1D projection of Appendix A.1, we can make a 4D to 3D projection of a hyperellipsoid by looking for extrema in the values of three of the coordinates on the hyperellipsoidal surface. Let us first define the 4D hyperellipsoid through the equation

$$1 = \underline{\boldsymbol{\chi}}^T \cdot \underline{\mathbf{L}} \cdot \underline{\boldsymbol{\chi}}, \quad (\text{A.8})$$

where

$$\underline{\boldsymbol{\chi}} \equiv \begin{pmatrix} x_1 \\ x_2 \\ x_3 \\ x_4 \end{pmatrix}, \quad (\text{A.9})$$

$$\underline{\mathbf{L}} = \begin{pmatrix} L_{11} & L_{12} & L_{13} & L_{14} \\ L_{12} & L_{22} & L_{23} & L_{24} \\ L_{13} & L_{23} & L_{33} & L_{34} \\ L_{14} & L_{24} & L_{34} & L_{44} \end{pmatrix}. \quad (\text{A.10})$$

We expand Eq. (A.8) as

$$1 = L_{11}x_1^2 + L_{22}x_2^2 + L_{33}x_3^2 + L_{44}x_4^2 + 2L_{12}x_1x_2 + 2L_{13}x_1x_3 + 2L_{14}x_1x_4 + 2L_{23}x_2x_3 + 2L_{24}x_2x_4 + 2L_{34}x_3x_4, \quad (\text{A.11})$$

which we then implicitly differentiate to yield

$$\begin{aligned}
0 = & 2L_{11}x_1dx_1 + 2L_{22}x_2dx_2 + 2L_{33}x_3dx_3 + 2L_{44}x_4dx_4 \\
& + 2L_{12}(x_1dx_2 + x_2dx_1) + 2L_{13}(x_1dx_3 + x_3dx_1) + 2L_{14}(x_1dx_4 + x_4dx_1) \\
& + 2L_{23}(x_2dx_3 + x_3dx_2) + 2L_{24}(x_2dx_4 + x_4dx_2) + 2L_{34}(x_3dx_4 + x_4dx_3).
\end{aligned} \tag{A.12}$$

To project the 4D hyperellipsoid defined by Eq. (A.11) into the subspace (x_1, x_2, x_3) , we find the extremal points in these coordinates by setting $dx_1 = dx_2 = dx_3 = 0$ in Eq. (A.12). In this case, we find

$$x_4 = -\frac{1}{L_{44}}(L_{14}x_1 + L_{24}x_2 + L_{34}x_3), \tag{A.13}$$

which we substitute into Eq. (A.11) to obtain the equation for the 3D ellipsoid that bounds the projection of the 4D hyperellipsoid defined by Eq. (A.11) into the subspace (x_1, x_2, x_3) , i.e.,

$$\begin{aligned}
L_{44} = & (L_{11}L_{44} - L_{14}^2)x_1^2 + (L_{22}L_{44} - L_{24}^2)x_2^2 + (L_{33}L_{44} - L_{34}^2)x_3^2 \\
& + 2(L_{12}L_{44} - L_{14}L_{24})x_1x_2 + 2(L_{13}L_{44} - L_{14}L_{34})x_1x_3 + 2(L_{23}L_{44} - L_{24}L_{34})x_2x_3.
\end{aligned} \tag{A.14}$$

A.4 2D Projection of the 3D Ellipsoid

The 3D ellipsoid of Eq. (A.14) can be further projected into the 2D subspace (x_1, x_2) . We first implicitly differentiate Eq. (A.14) to obtain

$$\begin{aligned}
0 = & 2(L_{11}L_{44} - L_{14}^2)x_1dx_1 + 2(L_{22}L_{44} - L_{24}^2)x_2dx_2 + 2(L_{33}L_{44} - L_{34}^2)x_3dx_3 \\
& + 2(L_{12}L_{44} - L_{14}L_{24})(x_1dx_2 + x_2dx_1) + 2(L_{13}L_{44} - L_{14}L_{34})(x_1dx_3 + x_3dx_1) \\
& + 2(L_{23}L_{44} - L_{24}L_{34})(x_2dx_3 + x_3dx_2).
\end{aligned} \tag{A.15}$$

Setting $dx_1 = dx_2 = 0$, Eq. (A.15) implies

$$x_3 = \frac{(L_{14}L_{34} - L_{13}L_{44})x_1 + (L_{24}L_{34} - L_{23}L_{44})x_2}{L_{33}L_{44} - L_{34}^2}, \tag{A.16}$$

which we substitute into Eq. (A.14) to obtain

$$\begin{aligned}
1 = & \frac{L_{14}^2 L_{33} - 2L_{13} L_{14} L_{34} + L_{11} L_{34}^2 + L_{13}^2 L_{44} - L_{11} L_{33} L_{44}}{L_{34}^2 - L_{33} L_{44}} x_1^2 \\
& + 2 \frac{L_{14} L_{24} L_{33} - L_{14} L_{23} L_{34} - L_{13} L_{24} L_{34} + L_{12} L_{34}^2 + L_{13} L_{23} L_{44} - L_{12} L_{33} L_{44}}{L_{34}^2 - L_{33} L_{44}} x_1 x_2 \\
& + \frac{L_{24}^2 L_{33} - 2L_{23} L_{24} L_{34} + L_{22} L_{34}^2 + L_{23}^2 L_{44} - L_{22} L_{33} L_{44}}{L_{34}^2 - L_{33} L_{44}} x_2^2.
\end{aligned} \tag{A.17}$$

Equation (A.17) is the 2D ellipse boundary of the projection of the 4D hyperellipsoid defined by Eq. (A.11) into the subspace (x_1, x_2) .

Recalling Eq. (2.100) and comparing it to Eq. (A.8), we make the identification

$$\underline{\underline{\mathbf{L}}} = \underline{\underline{\mathbf{M}}}^{-1}, \tag{A.18}$$

which allows us to relate the elements L_{ij} to the elements M_{ij} . Making use of Eq. (A.18) to rewrite Eq. (A.17) in terms of the elements of $\underline{\underline{\mathbf{M}}}$, we find, after considerable simplification,

$$1 = \frac{M_{22}}{M_{11} M_{22} - M_{12}^2} x_1^2 - 2 \frac{M_{12}}{M_{11} M_{22} - M_{12}^2} x_1 x_2 + \frac{M_{11}}{M_{11} M_{22} - M_{12}^2} x_2^2, \tag{A.19}$$

which is identical to Eq. (2.108), or, equivalently, Eq. (2.105).

B Envelope Quantities

The matrix equation (A.1) describes an ellipse in the 2D space (x_1, x_2) . If this ellipse is also described by Eq. (2.111), we can equate the coefficients to obtain

$$C_{11} = \frac{\cos^2 \theta_{12}}{A^2} + \frac{\sin^2 \theta_{12}}{B^2}, \tag{B.20}$$

$$C_{12} = \frac{1}{2} \left(\frac{1}{A^2} - \frac{1}{B^2} \right) \sin(2\theta_{12}), \tag{B.21}$$

$$C_{22} = \frac{\sin^2 \theta_{12}}{A^2} + \frac{\cos^2 \theta_{12}}{B^2}. \tag{B.22}$$

If this same ellipse is also described by Eq. (2.105), then we know that

$$\underline{\underline{\mathbf{M}}}_{12} = \underline{\underline{\mathbf{C}}}^{-1}, \tag{B.23}$$

and we can relate the elements of matrix $\underline{\underline{\mathbf{M}}}_{12}$ to the elements of matrix $\underline{\underline{\mathbf{C}}}$ through

$$M_{11} = \frac{C_{22}}{C_{11}C_{22} - C_{12}^2}, \quad (\text{B.24})$$

$$M_{12} = -\frac{C_{12}}{C_{11}C_{22} - C_{12}^2}, \quad (\text{B.25})$$

$$M_{22} = \frac{C_{11}}{C_{11}C_{22} - C_{12}^2}. \quad (\text{B.26})$$

Combining Eqs. (B.20), (B.21), and (B.22) with Eqs. (B.24), (B.25), and (B.26), we obtain, after some simplification, Eqs. (2.112), (2.113), and (2.114).

The inverse relations for the envelope quantities are obtained with the quadratic form methods presented in Korn and Korn [56]. Equation (A.1) is a quadratic form representing an ellipse whose semi-axes A and B ($B < A$), and twist angle θ_{12} are given by

$$A^2 = \frac{\|\underline{\underline{\mathbf{C}}}\|}{\lambda_1 \lambda_2^2}, \quad (\text{B.27})$$

$$B^2 = \frac{\|\underline{\underline{\mathbf{C}}}\|}{\lambda_1^2 \lambda_2}, \quad (\text{B.28})$$

$$\tan 2\theta_{12} = 2 \frac{C_{12}}{C_{11} - C_{22}}, \quad (\text{B.29})$$

where λ_1 and λ_2 ($\lambda_2 < \lambda_1$) are the eigenvalues of the matrix $\underline{\underline{\mathbf{C}}}$.

From Eq. (B.23), we have

$$C_{11} = \frac{M_{22}}{M_{11}M_{22} - M_{12}^2}, \quad (\text{B.30})$$

$$C_{12} = -\frac{M_{12}}{M_{11}M_{22} - M_{12}^2}, \quad (\text{B.31})$$

$$C_{22} = \frac{M_{11}}{M_{11}M_{22} - M_{12}^2}, \quad (\text{B.32})$$

which, combined with Eqs. (B.27), (B.28), and (B.29), yield Eqs. (2.115), (2.116), and (2.117).

C Negligibility of Perturbed Trajectory Term

We neglect a term proportional to $d\delta\bar{x}_x/d\bar{z}$ in Eq. (5.43) in order to integrate the equation and solve for $\delta\bar{y}_x$, and here we demonstrate the validity of that approximation. For this term to be negligible compared to the other driving term, we require [referring to Eq. (5.43)]

$$\left| \frac{\alpha_y \bar{B}_0}{k\gamma\beta} \frac{\bar{k}}{\bar{k}_0^2} \frac{d\delta\bar{x}_x}{d\bar{z}} \right| \ll \left| (1-r_m) \frac{\alpha_y \bar{B}_0}{k\gamma\beta} \left(\frac{r_m}{1-r_m} \frac{\bar{k}^2}{\bar{k}_0^2} - \frac{\bar{b}_{\text{des}}^2}{\bar{a}_{\text{des}}^2} \right) \right|. \quad (\text{C.33})$$

Using Eq. (5.96) to specify $d\delta\bar{x}_x/d\bar{z}$, this implies

$$\left| \frac{\bar{k}^2}{\bar{k}_0^2} \frac{1}{2} \frac{\bar{k}_-^2 \bar{k}_+^2}{\bar{k}^4} \left(\sigma - \frac{1}{8} \frac{\bar{b}_{\text{des}}}{\bar{a}_{\text{des}}} \right) \right| \ll \left| (1-r_m) \left(\frac{r_m}{1-r_m} \frac{\bar{k}^2}{\bar{k}_0^2} - \frac{\bar{b}_{\text{des}}^2}{\bar{a}_{\text{des}}^2} \right) \right|, \quad (\text{C.34})$$

which simplifies, using Eqs. (5.63), (5.76), and (5.79) to

$$\left| r_m \frac{\bar{b}_{\text{des}}}{\bar{a}_{\text{des}}} \frac{\bar{k}_0^4}{\bar{k}^4} + \frac{1}{2} r_m^2 \frac{\bar{k}_0^4}{\bar{k}^4} + \frac{1}{8} \frac{\bar{b}_{\text{des}}^2}{\bar{a}_{\text{des}}^2} \frac{\bar{k}_0^4}{\bar{k}^4} \right| \ll \left| r_m - \frac{\bar{b}_{\text{des}}^2}{\bar{a}_{\text{des}}^2} \frac{\bar{k}_0^2}{\bar{k}^2} \right|, \quad (\text{C.35})$$

where we have retained the lowest-order terms.

Each term on the left-hand side of Eq. (C.35) is dominated by a term on the right-hand side if we make use of Eqs. (5.5), (5.12), and (5.46). The inequality only fails when the term on the right vanishes, i.e., conservatively, when

$$\frac{1}{2} \frac{\bar{b}_{\text{des}}^2}{\bar{a}_{\text{des}}^2} \frac{\bar{k}_0^2}{\bar{k}^2} \lesssim r_m \lesssim \frac{3}{2} \frac{\bar{b}_{\text{des}}^2}{\bar{a}_{\text{des}}^2} \frac{\bar{k}_0^2}{\bar{k}^2}. \quad (\text{C.36})$$

If the magnetic field aspect ratio r_m is outside the range given in Eq. (C.36), the term proportional to $d\delta\bar{x}_x/d\bar{z}$ in Eq. (5.43) is negligible.

References

- [1] J. Plücker, *Annalen der Physik und Chemie*, vol. 13, p.88, 1858.
- [2] P.A. Sturrock, "Magnetic deflection focusing," *J. Electron. Control*, vol. 7, pp. 162-168, August 1959.
- [3] T.P. Wangler, *et al.*, "Beam-halo in mismatched proton beams," *Nucl. Inst. & Methods A*, vol. 519, pp. 425-431, February 2004.
- [4] S. Bernal, *et al.*, "Beam experiments in the extreme space-charge limit on the University of Maryland Electron Ring," *Phys. Plasmas*, vol. 11, pp. 2907-2915, May 2004.
- [5] C. Chen, R. Pakter, and R.C. Davidson, "Ideal matching of heavy ion beams," *Nucl. Inst. And Methods A*, vol. 464, pp. 518-523, May 2001.
- [6] S. J. Russell, *et al.*, "First observation of elliptical sheet beam formation with an asymmetric solenoid lens," *Phys. Rev. ST Accel. Beams*, vol. 8, 080401, August 2005.
- [7] S. Humphries, *et al.*, "Circular-to-planar transformations of high-perveance electron beams by asymmetric solenoid lenses," *Phys. Rev. ST Accel. Beams*, vol. 7, 060401, June 2004.
- [8] A. Burke, R. Phillips, and G. Scheitrum, "W-band sheet beam klystron gun design using MICHELLE," International Vacuum Electronics Conference Proceedings, p. 43, Monterey, California, April 25-27, 2006.
- [9] M. Read, *et al.*, "Beam generation and transport for a THz twt," International Vacuum Electronics Conference Proceedings, p. 49, Monterey, California, April 25-27, 2006.
- [10] B. Danly, *et al.*, "Sheet-beam electron gun design for millimeter and sub-millimeter wave vacuum electronic sources," International Vacuum Electronics Conference Proceedings, p. 115, Monterey, California, April 25-27, 2006.
- [11] S.J. Russell, *et al.*, "Sheet beam development for mm-wave microwave tubes at Los Alamos National Laboratory," International Vacuum Electronics Conference Proceedings, p. 143, Monterey, California, April 25-27, 2006.
- [12] G. Scheitrum, *et al.*, "W-band sheet beam klystron research at SLAC," International Vacuum Electronics Conference Proceedings, p. 481, Monterey, California, April 25-27, 2006.
- [13] G. Caryotakis, *et al.*, "Design of an 11.4 GHz, 150-MW, Sheet Beam, PPM-Focused Klystron," *AIP Conference Proceedings*, vol. 691, pp. 22-33, December 2003.
- [14] B.E. Carlsten, *et al.*, "Stable two-plane focusing for emittance-dominated sheet-beam transport," *Phys. Rev. ST Accel. Beams*, vol. 8, 062002, June 2005.
- [15] M.A. Basten and J.H. Booske, "Two-plane focusing of high-space-charge sheet electron beams using periodically cusped magnetic fields," *J. Appl. Phys.* vol. 85, pp. 6313-6322, May 1999.

- [16] R. Pakter and C. Chen, "Cold-fluid equilibrium for a corkscrewing elliptic beam in a variable focusing channel," *Phys. Rev. E*, vol. 62, pp. 2789-2796, August 2000.
- [17] C. Adolphsen, "ILC R&D & Opportunities for Industry", Fermilab Meeting of the Linear Collider Forum of America, September 2005.
- [18] B. Carlsten, *et al.*, "Technology Development for a mm-Wave Sheet-Beam Traveling-Wave Tube", *IEEE Trans. Plasma Sci.*, vol. 33, pp. 85-93, February 2005.
- [19] J. Zhou, R. Bhatt, and C. Chen, "Cold-fluid theory of equilibrium and stability of a high-intensity periodically twisted ellipse-shaped charged-particle beam," *Phys. Rev. ST Accel. Beams*, vol. 9, 034401, March 2006.
- [20] B.L. Qian, J. Zhou, and C. Chen, private communication.
- [21] Z. Zhang, *et al.*, "Experimental and numerical studies of sheet electron beam propagation through a planar wiggler magnet," *IEEE Trans. Plasma Sci.*, vol. 21, pp. 760-767, December 1993.
- [22] W.W. Destler, *et al.*, "First operation of a wiggler-focused, sheet beam free electron laser amplifier," *Phys. Plasmas*, vol. 1, pp. 1708-1713, May 1994.
- [23] J.H. Booske, B.D. McVey, and T.M. Antonsen, "Stability and confinement of nonrelativistic sheet electron beams with periodic cusped magnetic focusing," *J. Appl. Phys.*, vol. 73, pp. 4140-4155, May 1993.
- [24] J. Zhou, private communication.
- [25] C. Chen, R. Bhatt, A. Radovinsky, and J. Zhou, "Three-Dimensional Design of a Non-Axisymmetric Periodic Permanent Magnet Focusing Ssystem," *Proceedings of the Particle Accelerator Conference, Knoxville, Tennessee*, p. 1964, May 2005.
- [26] F. Sacherer, "Transverse Space Charge Effects in Circular Accelerators," Ph.D. Thesis, U.C. Berkeley, 1968.
- [27] C. Chen and R. Pakter, "Mechanisms and control of beam halo formation in intense microwave sources and accelerators," *Phys. Plasmas*, vol. 7, pp. 2203-2214, May 2000.
- [28] R.C. Davidson, P. Stoltz, and C. Chen, *Phys. Plasmas*, vol. 4, pp. 3710-3717, October 1997.
- [29] C.D. Child, "Discharge from Hot Cao," *Phys. Rev.*, vol. 32, pp. 492-511, May 1911; I. Langmuir, "Effect of space charge and initial velocities on the potential distribution and thermionic current between parallel plane electrodes," *Phys. Rev.*, vol. 21, pp. 419-435, April 1923.
- [30] P. Kirstein, G. Kino, and W. Waters, *Space Charge Flow* (McGraw-Hill, New York, 1967), p. 331.
- [31] J.W. Luginsland, Y.Y. Lau, R.J. Umstadtd, J.J. Watrous, "Beyond the Child-Langmuir law: A review of recent results on multidimensional space-charge-limited flow," *Phys. Plasmas*, vol. 9, pp. 2371-2376, May 2002.

- [32] J.J. Watrous, J.W. Luginsland, and M. Frese, "Current and current density of a finite-width, space-charge-limited electron beam in two-dimensional, parallel-plate geometry," *Phys. Plasmas*, vol. 8, pp. 4202-4210, September 2001.
- [33] J.W. Luginsland, Y.Y. Lau, and R.M. Gilgenbach, "Two-dimensional Child-Langmuir law," *Phys. Rev. Lett.*, vol. 77, pp. 4668-4670, November 1996.
- [34] R.J. Umstadtd and J.W. Luginsland, "Two-dimensional space-charge-limited emission: beam-edge characteristics and applications," *Phys. Rev. Lett.*, vol. 87, 145002, October 2001.
- [35] Y.Y. Lau, Phys. "Simple theory for the two-dimensional Child-Langmuir law," *Phys. Rev. Lett.*, vol. 87, 278301, December 2001.
- [36] J.R. Pierce, *Theory and Design of Electron Beams*, (D. Van Nostrand Company, Inc., New York, 1954)
- [37] W.B. Hermannsfeldt, "Electron Trajectory Program," SLAC Reports, vol. 226, 1979.
- [38] OMNITRAK software, copyright Field Precision, Albuquerque, NM. Available: <http://www.fieldp.com>
- [39] J. Petillo et al., IEEE Trans. Plasma Science, vol. 30, issue 3, p. 1238, 2002.
- [40] D. P. Grote, A. Friedman, I. Haber, W. Fawley, J.L. Vay, *Nucl. Inst. & Methods A*, vol. 415, p. 428, 1998.
- [41] H.R. Jory and A.W. Trivelpiece, "Exact Relativistic Solution for the One-Dimensional Diode," *J. Appl. Phys.*, vol. 40, p. 3924, 1969.
- [42] P. Morse and H. Feshbach, *Methods of Theoretical Physics* (McGraw-Hill, New York, 1953), vol. 1, Ch. 6, p. 702.
- [43] D.E. Radley, "Theory of the Pierce Type Electron Gun", *J. Elect. Contr.*, vol. 4, p. 125, 1957.
- [44] A. Nakai, *Nucl. Inst. & Methods*, vol. 54, p. 57, 1967.
- [45] R. Bhatt and C. Chen, "Theory and simulation of nonrelativistic elliptic-beam formation with one-dimensional Child-Langmuir flow characteristics," *Phys. Rev. ST Accel. Beams* 8, 014201, January 2005.
- [46] P. Morse and H. Feshbach, *Methods of Theoretical Physics* (McGraw-Hill, New York, 1953), vol. 2, Ch. 11, p. 1568.
- [47] P. Morse and H. Feshbach, *Methods of Theoretical Physics* (McGraw-Hill, New York, 1953), vol. 1, Ch. 4, p.421.
- [48] J. C. Gutierrez-Vega et al., "Theory and Numerical Analysis of the Mathieu Functions," research notes, 2003. Available: <http://homepages.mty.itesm.mx/jgutierrez/mathieu.htm>
- [49] S. Humphries, *Charged Particle Beams*, <http://www.fieldp.com>, Ch. 3, pp. 90-101.
- [50] J.D. Lawson, *Physics of Charged Particle Beams* (Clarendon, Oxford, UK, 1988), p. 210.
- [51] M. Conte and W. MacKay, *An Introduction to the Physics of Particle Accelerators* (World Scientific, Singapore, 1991).

- [52] R. Davidson, *Physics of Nonneutral Plasmas* (Addison-Wesley, Redwood City, 1990).
- [53] J.H. Booske, M.A. Basten, and A.H. Kumbasar, "Periodic magnetic focusing of sheet electron beams," *Phys. Plasmas*, vol. 1, pp. 1714-1720, May 1994.
- [54] J.H. Booske and M.A. Basten, "Demonstration via simulation of stable confinement of sheet electron beams using periodic magnetic focusing," *IEEE Trans. Plasma Sci.*, vol. 27, pp. 134-135, February 1999.
- [55] B.E. Carlsten, *et al.*, "Stability of an emittance-dominated sheet-electron beam in planar wiggler and periodic permanent magnet structures with natural focusing," *Phys. Rev. ST Accel. Beams*, vol 8, 062001, June 2005.
- [56] G. Korn and T. Korn, *Mathematical Handbook for Scientists and Engineers*, (McGraw-Hill, New York, 1968), ch. 2, pp. 42-44.
- [57] R. Bhatt, T. Bemis, C. Chen, "Three-dimensional theory and simulation of nonrelativistic elliptic electron and ion beam generation," (invited paper) *IEEE Trans. Plasma Sci.*, vol. 34, pp. 187-193, April 2006.
- [58] M. Hess and C. Chen, "Confinement Criterion for a Highly Bunched Beam", *Phys. Plasmas*, v. 7, p. 5206 (2000).
- [59] I.S. Gradshteyn, and I.M. Ryzhik, *Table of Integrals, Series, and Products*, 5th Edition (Academic Press, San Diego, 1994)
- [60] J. Jackson, *Classical Electrodynamics* (Wiley, New York, 1962).
- [61] L. Schächter, *Beam-Wave Interaction in Periodic and Quasi Periodic Structures* (Springer-Verlag, Berlin, 1997).
- [62] A.I. Borisenko, and I.E. Tarapov, *Vector and Tensor Analysis with Applications* (Dover, New York, 1968)
- [63] T. Apostol, *Calculus Vol II* (Wiley, New York, 1967).
- [64] Joe Thompson, S. Bharat, and N. Weatherill, eds., *Handbook of Grid Generation* (CRC Press, Boca Raton, 1999)
- [65] Sasamoto, H. Imai, and H. Kawarada, "A Practical Method for an Ill-Conditioned Optimal Shape Design of a Vessel in which Plasma is Confined", in *Inverse Problems in Engineering Sciences - ICM-90 Satellite Conference Proceedings Osaka 1990* (Springer-Verlag, Tokyo 1991)
- [66] H. Imai, A. Sasamoto, H. Kawarada, M. Natori, "An Application of the Fuzzy Theory for an Ill-Posed Problem", in *Inverse Problems in Engineering Mechanics - IUTAM Symposium Tokyo 1992* (Springer-Verlag, Berlin 1992)
- [67] F. Berntsson and L. Elden, "Numerical Solution of an Inverse Steady State Heat Conduction Problem", in *Inverse Problems in Engineering Mechanics II - International Symposium on Inverse Problems in Engineering Mechanics Nagano 2000* (Elsevier, Oxford 2000).
- [68] Samuel Liao, *Microwave Electron-Tube Devices* (Prentice-Hall, Englewood Cliffs, 1988).
- [69] John Smedly, *et al.*, "Design and Performance of a High Brightness Pulsed Power Electron Source", BNL Instrumentation seminar, Feb. 6, 2002.

- [70] George Caryotakis, SLAC Klystron Lecture Series, *Lecture 2 - Velocity Modulation*, Jan. 21, 2004, http://www-group.slac.stanford.edu/kly/Old_web_site/slac_klystron_lecture_series.htm
- [71] J.C. Gutierrez Vega, "Theory and Numerical Analysis of the Mathieu Functions", Thesis, Instituto Tecnológico y de Estudios Superiores de Monterrey, 2003.
- [72] J. R. Pierce, "My work with vacuum tubes at Bell Laboratories," *SMEEC Vintage Electrics*, vol. 3, 1991. Available: http://www.smecc.org/john_r_pierce_electron_tubes.htm
- [73] F. Zhou, et al., "Experimental characterization of emittance growth induced by the nonuniform transverse laser distribution in a photoinjector," *Phys. Rev. ST Accel Beams*, vol. 5, 094203, September 2002.